이학박사학위논문

Topological edge state lasers based on photonic Su-Schrieffer-Heeger lattices

Su−Schrieffer−Heeger 광자 구조를 활용한 위상적 가장자리 상태 레이저

2020년 8월

서울대학교 대학원

물리천문학부

한 창 현

Abstract

Topological edge state lasers based on photonic Su-Schrieffer-Heeger lattices

Changhyun Han
Department of Physics and Astronomy
The Graduate School
Seoul National University

Topological phases of matter opened the era of quantum materials by suggesting new states of matter. In particular, topological insulators are insulating in the bulk, but simultaneously the surface is conducting and the flow of surface electrons is topologically protected, so that scattering due to imperfections can be suppressed. These characteristics are expected to be useful for the development of spintronic devices or for stable information storage in quantum computers. On the other hand, the discovery in the fields of condensed matter has become another cornerstone for studying topological properties in other wave-particle systems such as light. In the case of the topological edge state of light, since it can be protected from backscattering due to imperfections as in the case of the electrons in the topological insulators, it is expected to be utilized in high-efficiency optical waveguides, couplers, and so on.

Many studies on topological photonics have been conducted to observe the propagation characteristics of light, such as time-reversal symmetry broken edge states using a magnetic field, and spin-protected edge states using dedicatedly

designed pseudospin of light. Lasing action from topological edge states has not been studied as much as passive (transport) properties. In the case of previous studies on the topological lasers mainly utilizing the microring resonator, the sizes of the device and the mode are dozens of micrometers. However, by using a photonic crystal resonator, the mode can be reduced to a wavelength scale, and a single mode oscillation is feasible due to the small mode size. Therefore, if an edge state laser using a photonic crystal resonator is developed, it is expected to be a new turning point in the study of the topological edge state lasers. In addition, the photonic crystal resonators usually suffer from process imperfections due to its small feature size. The topological edge state is relatively less sensitive to the disorder caused by such process variations, and thus the yield improvement of the optical device can be expected.

In this thesis, for the first research topic, a robust topological edge state which is formed in a finite chain of photonic crystal (PhC) nanocavities combined with the Su-Schrieffer-Heeger (SSH) model is theoretically and experimentally demonstrated. We implement the model by arranging the same PhC nanocavities in an SSH dimer chain configuration composed of InAsP / InP multiple quantum well (MQW) epilayers, and demonstrate lasing behavior in relevant topological edge state and bulk state. In addition, the presence and robustness of TES is demonstrated by spectral analysis as well as direct visualization of the corresponding modal pattern using near-field optical microscopy techniques.

For the second research topic, inspired by novel higher-order topological insulator concept, we fabricate a 2D SSH-like topological photonic crystal structure using a InGaAsP MQW semiconductor optical gain material and confirm laser oscillations in multiple dimensional topological states existing in the structure. It is proved

through spectral analysis and emission imaging that various lasers are selectively excited by varying the position of the pump light in a single photonic crystal device. Finally, brief results of a valley edge mode laser are introduced. Valley edge modes which exist at the interface of two inversion symmetry-broken valley photonic crystals are utilized to form a ring cavity, which is enabled by topological protection of edge modes from sharp bends along the interface waveguide. Lasing action from the ring cavity is demonstrated and the fact that the formation of the ring cavity is truly a fruit of topological protection of the edge modes is confirmed by comparing with a trivial cavity laser.

Keyword : Photonic crystals, Topological photonics, Su-Schrieffer-Heeger model, Edge mode lasers, Valley edge modes

Student Number : 2014-21364

Table of Contents

List of Figures

Chapter 1. Introduction

1.1. Photonic crystals and photonic crystal lasers

1.1.1. Introduction to the photonic crystal

Controlling the flow of light at will is a long-standing goal for many scientists and engineers. It is much harder to handle light (photons) than electrons since photons are not interacting particles and not directly affected by external environments such as electric and magnetic fields. In this context, a photonic crystal is a useful tool for overcoming such a particularity of the photon. The photonic crystal, which seems unfamiliar and rather fancy, is actually found in our life and nature. For example, an optical mouse which we are using every day and even now is equipped with a VCSEL (Vertical-Cavity Surface Emitting Laser), which is utilizing a principle of the photonic crystal [1]. A distributed feedback laser (DFB) that is used in optical communications also utilizes the photonic crystals which function similar to those of the VCSELs [2]. More striking examples can be found in nature. Several organisms exhibit extraordinary coloration without any color-producing component, such as pigments. If we take a close look at these organisms, one can find that such coloration is originated from elaborately designed nanostructures, which can be referred to the photonic crystals [3].

The photonic crystal is an optical structure where optical materials with different refractive indices are periodically arranged. It affects the flow of light in a similar way as an electronic crystal does to the electrons. To see how it relates to the electronic crystals, we should start from the Maxwell equations which govern the macroscopic behaviors of the electromagnetic field in dielectric media [4],

$$\nabla \cdot \mathbf{H}(\mathbf{r},t) = 0$$
$$\nabla \cdot [\epsilon(\mathbf{r})\mathbf{E}(\mathbf{r},t)] = 0$$
$$\nabla \times \mathbf{E}(\mathbf{r},t) + \frac{\mu_0 \partial \mathbf{H}(\mathbf{r},t)}{\partial t} = 0 \qquad (1)$$
$$\nabla \times \mathbf{H}(\mathbf{r},t) - \frac{\epsilon_0 \epsilon(\mathbf{r}) \partial \mathbf{E}(\mathbf{r},t)}{\partial t} = 0.$$

Here, we have displacement fields, $\mathbf{D}(\mathbf{r}) = \epsilon_0 \epsilon(\mathbf{r})\mathbf{E}(\mathbf{r})$, and magnetic fields, $\mathbf{B}(\mathbf{r}) = \mu_0 \mathbf{H}(\mathbf{r})$, where ϵ_0 and μ_0 are the vacuum dielectric constant and the vacuum permeability. The photonic crystal features are dissolved in the relative dielectric constant, $\epsilon(\mathbf{r})$. Then we write the electric and magnetic field as complex-valued forms,

$$\mathbf{H}(\mathbf{r},t) = \mathbf{H}(\mathbf{r})e^{i\omega t}$$
$$\mathbf{E}(\mathbf{r},t) = \mathbf{E}(\mathbf{r})e^{i\omega t}. \qquad (2)$$

Then, inserting (2) to (1), the two curl equations in (1) become,

$$\nabla \times \mathbf{E}(\mathbf{r}) - i\omega\mu_0 \mathbf{H}(\mathbf{r}) = 0$$
$$\nabla \times \mathbf{H}(\mathbf{r}) + i\omega\epsilon_0 \epsilon(\mathbf{r})\mathbf{E}(\mathbf{r}) = 0 \qquad (3)$$

These coupled equations can be combined to a single equation that needs to be solved preferentially, by using the fact that the speed of light follows the relation, $c = \sqrt{\epsilon_0 \mu_0}$.

$$\nabla \times \left(\frac{1}{\epsilon(\mathbf{r})} \nabla \times \mathbf{H}(\mathbf{r}) \right) = \left(\frac{\omega}{c} \right)^2 \mathbf{H}(\mathbf{r}) \qquad (4)$$

For a given $\epsilon(\mathbf{r})$, we can find the spatial distribution of the field, $\mathbf{H}(\mathbf{r})$, and the corresponding frequency, ω, by solving (4). It can be easily noticed that the above equation is in fact an eigenvalue equation whose eigenvalues and eigenvectors are $\left(\frac{\omega}{c}\right)^2$ and $\mathbf{H}(\mathbf{r})$, respectively. The

similarity between (4) and the well-known Schrödinger equation arises here. The Schrödinger equation is also an eigenvalue equation which have a frequency and a wavefunction as an eigenvalue and an eigenvector respectively. Therefore, we can imagine that photons in the periodic optical media will experience similar phenomena to those experienced by electrons in the periodic atomic potential. The comparison of electrodynamics and quantum mechanics is summarized in Table 1.

Table 1. Analogy between quantum mechanics and electrodynamics [4].

	Quantum Mechanics	*Electrodynamics*
Field	$\Psi(\mathbf{r},t)=\Psi(\mathbf{r})e^{-iEt/\hbar}$	$\mathbf{H}(\mathbf{r},t)=\mathbf{H}(\mathbf{r})e^{-i\omega t}$
Eigenvalue problem	$\hat{H}\Psi=E\Psi$	$\hat{\Theta}\mathbf{H}=\left(\frac{\omega}{c}\right)^2\mathbf{H}$
Hermitian operator	$\hat{H}=-\frac{\hbar^2}{2m}\nabla^2+V(\mathbf{r})$	$\hat{\Theta}=\nabla\times\frac{1}{\varepsilon(\mathbf{r})}\nabla\times$

1.1.2. Scaling property of electrodynamics

Despite the relationship between the two fundamental equations, there are several differences that make the electrodynamic equation (4) distinct from its electronic counterpart. One of the important and useful differences is a scaling property of the Maxwell equation. Unlike the Schrödinger equation, the Maxwell equation can be scaled in physical dimensions without changing any physical property of it. We can apply this to the equation (4) by considering the scaled dielectric constant $\epsilon'(\mathbf{r}) = \epsilon(\mathbf{r}/\mathrm{s})$ for the scale parameter s. Then the equation becomes,

$$\mathrm{s}\nabla' \times \left(\frac{1}{\epsilon(\mathbf{r}'/\mathrm{s})} \mathrm{s}\nabla' \times \mathbf{H}(\mathbf{r}'/\mathrm{s}) \right) = \left(\frac{\omega}{c}\right)^2 \mathbf{H}(\mathbf{r}'/\mathrm{s}) \qquad (5)$$

Dividing out the s's shows that the equations is the same as before, which means that the new mode profile and the mode frequency are simply scaled. The scaling property makes the photonic crystal structure applicable to entire frequency ranges, from microwave to optical frequency and further.

1.1.3. Photonic band structure

Depending on the dimensions of periodicity, photonic crystals can be classified by 1D, 2D and 3D photonic crystals, as shown Figure 1-1. A simple 1D photonic crystal is a multilayer stack or grating, which was studied by Lord Rayleigh [5] even before the term 'photonic crystal' was introduced by Eli Yablonovitch and Sajeev John in 1987 [6].

Just as the motion of electrons in the electronic crystal is defined by the electronic band structure, the behavior of photons in the photonic crystal is defined by the photonic band structure. The photonic band structure is usually composed of the continuum band allowing the existence of photons in the certain frequency ranges and the photonic band gap prohibiting the existence of photon in the other certain frequency ranges. The photonic band gap is useful since it can act as a mirror operating in the certain frequency ranges, since photons with those frequencies cannot propagate into the structure. It is also demonstrated that the spontaneous emission from the atomic transition is prohibited at the photonic band gap because there is no available photonic state.

Figure 1-2 shows examples of the photonic band structure. Such a simple band structure can be obtained from 1D photonic crystals (multilayer stack). The x-axis is a wave vector, which in the photonic crystal structure, is a crystal momentum. Unlike the wave vector in non-periodic structures, the crystal momentum is only meaningful in the range of the first Brillouin zone [7]. Outside the value of the zone boundary is a mere repetition of the first Brillouin zone. We can also see that the size of the photonic band gap is proportional to the difference of the dielectric constants of the constituent materials. This fact is useful for applications that require a large band gap.

The photonic band gap is interesting and of importance, but much attention is drawn into the band itself, as well. The photonic band is basically classified to the two polarizations, transvers-electric (TE) and transverse-magnetic (TM). The photonic bands of these two polarizations are different, which even affects the existence of the photonic band gap. Also, the photonic bands generally have flatten-slopes of their dispersion curves at certain wave vector points. These wave vector points are called high symmetry points since the mode profiles at those points are spatially highly symmetric. It should be noted that the slope of the dispersion curve has a special

meaning of the group velocity ($v = \frac{d\omega}{dk}$). The edges of the continuum bands are usually formed at such high symmetry points, and therefore the photons there should have very slow group velocities. Researchers have found that such a property is also valuable in making practical devices.

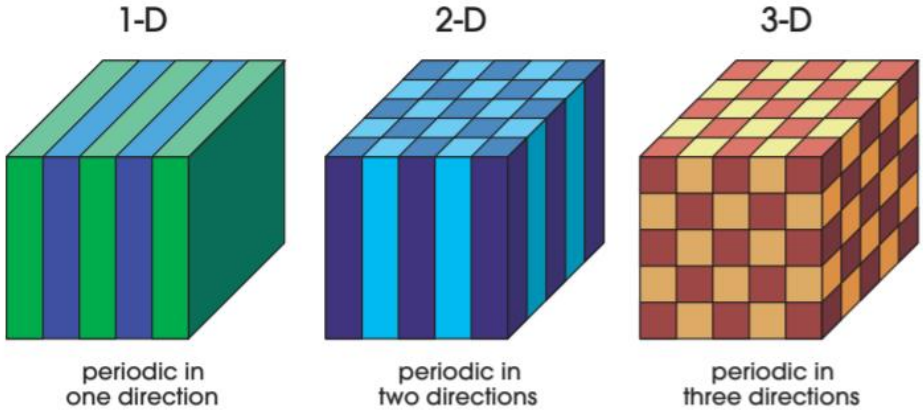

Figure 1- 1. Examples of 1D, 2D and 3D photonic crystals [4].

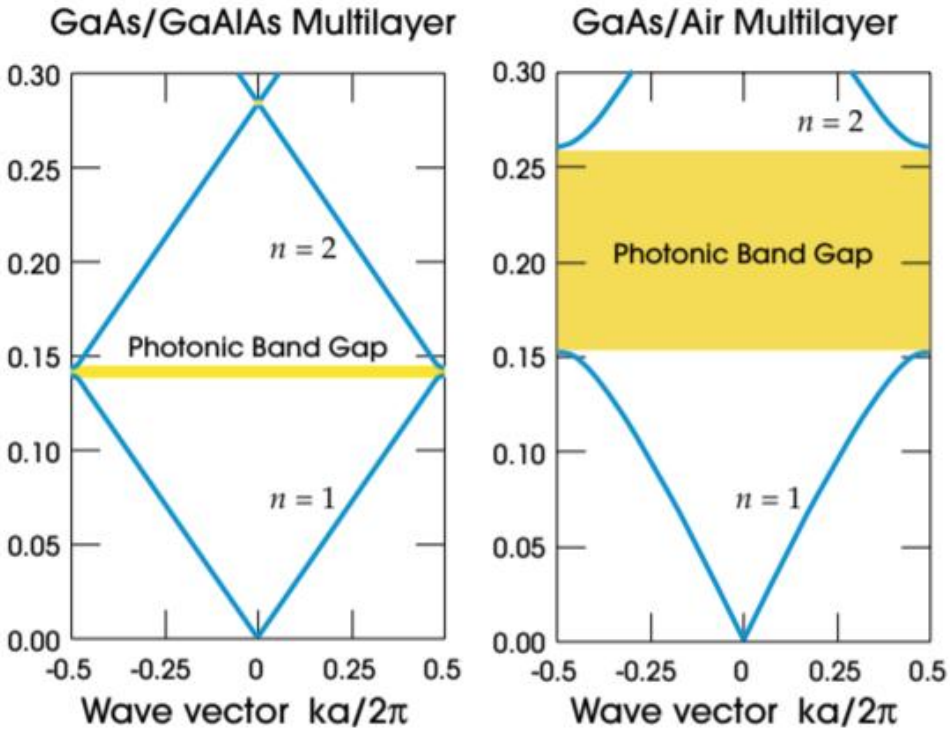

Figure 1- 2. Examples of the photonic band structure [4].

1.1.4. Photonic crystal band edge lasers

The properties of the photonic crystal can be utilized for various photonic devices. Among them, of great importance are lasers, which find their usages in various fields ranging from medical, military, imaging, communication and so on. For lasing action to occur, several requirements must be fulfilled, such as resonators and optical gains [8]. Traditionally, the optical cavity is formed by two mirrors which reflect light traveling opposite directions. One of the counterintuitive forms of the cavities is a DFB cavity, which can be considered as a 1D photonic crystal band edge laser. As introduced above, at the band edges, the dispersion curve becomes flatten and the group velocity becomes slower. This means that the effective path length of the photons becomes longer and as a result, the photons experience more optical gain than ordinary cases, provided that suitable optical gain material and pumping is introduced [9].

The mode size is an another characteristic of the band edge lasers. Unlike conventional cavity modes, the band edge modes are formed by multiple reflections by periodically arranged features. Therefore, the mode is in principle, extended over many periods, resulting in large mode volumes. Generally, the band edge modes are extended to the edges of the entire periodic structure. This large mode volume enables the band edge lasers operating at high power. It also should be considered that the band edge modes are located at one of the high symmetry points of wave vectors. This means that the modes have a specific momentum, deciding the direction of propagation [10]. Despite the group velocity of the band edge mode is close to zero as mentioned before, the band structure should be discretized because of the boundary condition of the finite structures, which prevents the modes from having exactly zero group velocity. Figure 1-3 shows the photonic band structure of the hexagonal lattice photonic crystal. Several band edge points are indicated by circles. The band edges near the wave vector Γ have negligible in plane momentum, therefore band edge lasers operating near the Γ points are surface emitting lasers [11]. On the other hand, the band edges that are not near the Γ points emit laser beam with the direction determined by the specific momenta, such as M or K points.

Since long ago, many kinds of the photonic band edge lasers incorporating various materials and structures have been demonstrated. Figure 1-4 shows an example of the photonic band edge lasers using InGaAsP multiple quantum wells as a gain medium. The holes arranged in the

hexagonal lattice are drilled into the semiconductor slab and vertical confinement was achieved by wet etching of the layer underneath of the slab. This kind of 2D photonic crystal slab is a widely used scheme to realize 2D photonic crystals in 3D space. The periodicity exists only in 2D plane, and a finite slab can act as vertical confinement without need of infinitely extended structures. This vertical confinement can be realized by the total internal reflection, requiring low index layers above and below the slab. This laser utilizes in-plane band edge modes. Optically excited, a single mode lasing action was demonstrated, which is presented from spectral and light-in light-out measurements.

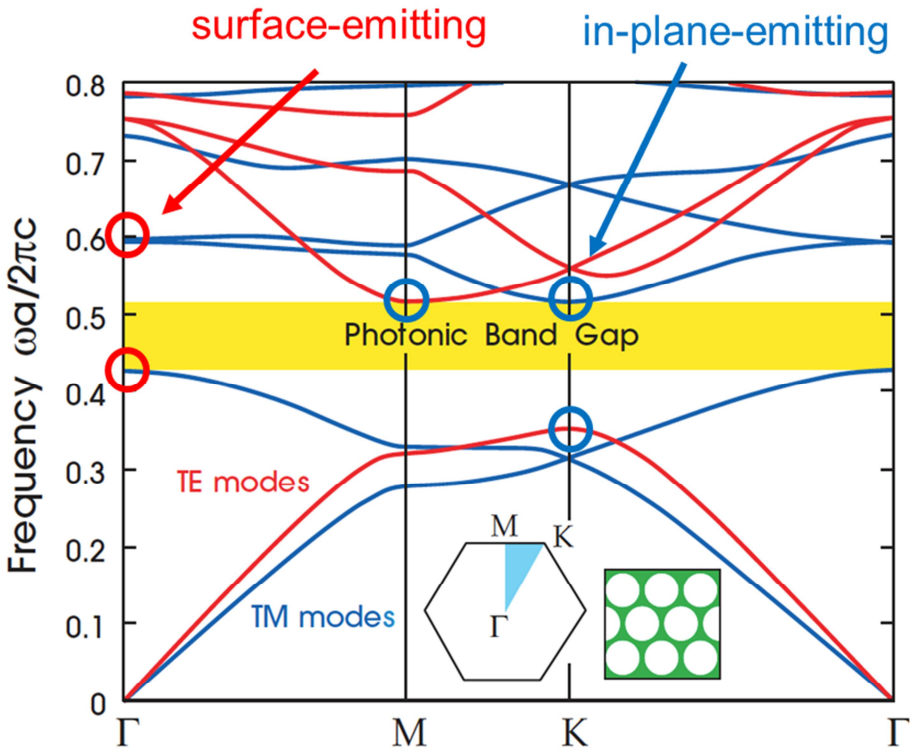

Figure 1- 3. Band structures of the hexagonal photonic crystal.

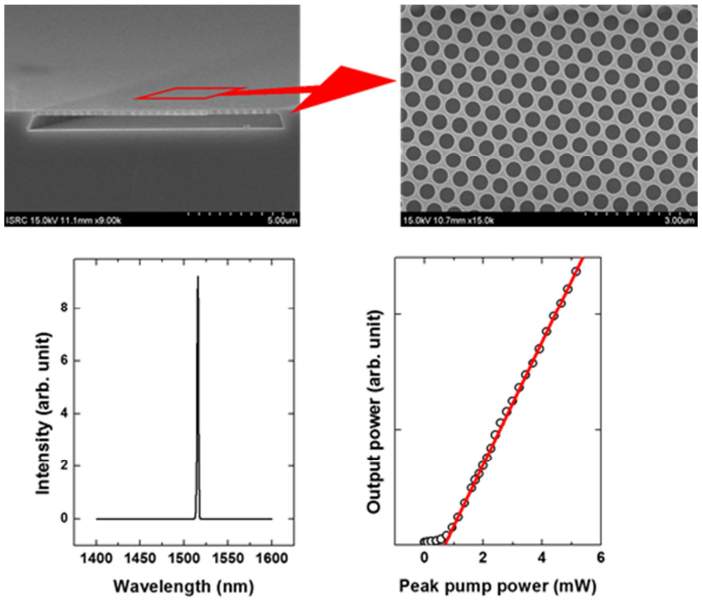

Figure 1- 4 A photonic band edge laser fabricated using InGaAsP multiple quantum wells [12].

1.1.5. Photonic crystal cavity lasers

As discussed at the earlier chapter, the photonic band gaps where no photonic state can exist is of great importance in the photonic band structure. As stated, the structure with the photonic band gap can be used as a mirror that can reflect specific wavelengths of light, which makes itself useful for various applications. Suppose that in the photonic crystal structure, there is a broken periodicity in the middle of the crystal structure. Then the optical states with the frequency in the photonic band gap of otherwise a perfect crystal can be located in the area called a defect, experiencing reflections from any direction surrounding there due to the photonic band gap. The result is a localized state at the defect of the photonic crystal structure. This defect state has a frequency inside the photonic band gap. The most striking example of usage of the defect state is a photonic crystal defect laser [13, 14]. Contrary to the photonic band edge laser, the lasing mode is only localized at the defect, not extending to the periodic region. A widely investigated platform for the photonic crystal defect laser is a 2D photonic crystal slab laser, which is shown in Figure 1-5. This kind of lasers obtain in-plane confinements by photonic band gap reflections and simultaneously, vertical confinement by the total internal reflection, same as the example stated at the previous chapter. Figure 1-6 shows an example of the photonic crystal defect laser. The missing hole is clearly seen in the middle of the array. Two cavity modes with different polarizations are contributing to the lasing action, as shown in the measured spectrum. The characteristics of the photonic crystal cavity laser is that the mode volume is much smaller than that of the photonic crystal band edge laser. Also, if elaborately designed, the quality factor of the mode can be high. A high quality factor is beneficial for low threshold lasing, which is crucial for energy-efficient devices. Furthermore, small mode volume allows itself to strongly interact with materials. This strong light-matter interaction is another highly pursued research topic, including Purcell effect [15], exciton-polariton quasi particle accompanying vacuum Rabi-splitting [16] and also sensing with very small targets. Lasers with very small mode volume will be, in the future, utilized as light sources for photonic integrated circuits that is expected to partially replace integrated circuits [17].

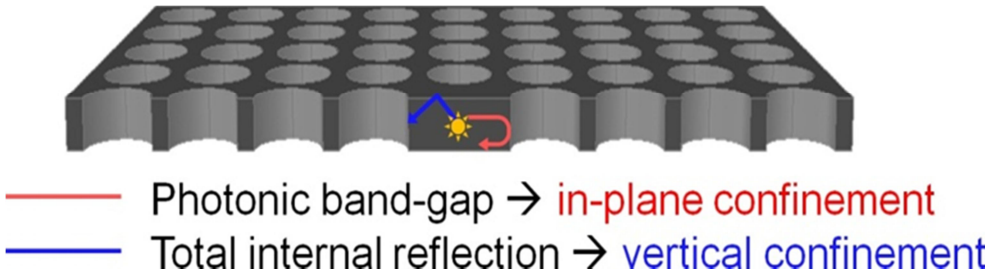

Figure 1- 5. Confinement mechanisms of the 2D photonic crystal slab cavity.

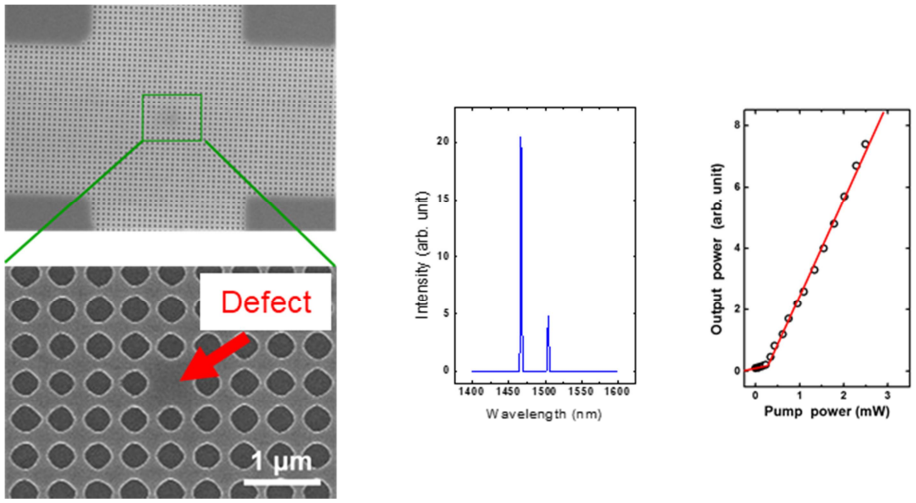

Figure 1- 6. Photonic crystal defect cavity laser [18].

1.2. Topological photonics

1.2.1. Topological Insulator and topological band theory

Topology is a subject concerning the properties of the object that are preserved under continuous deformations, such as stretching, twisting, bending, not tearing or gluing. Topology and condensed matter physics, which are seemingly unrelated subjects are now becoming the unseparated and, the resulting field of topological insulator is now the most attractive research area in the condensed matter physics [19]. The importance and the impact of topological insulators to academic is evidenced by the astronomical number of research papers subject to topological insulators. To explain topological insulators, we again should start with the band structure of electronic crystals. In addition to the well-known band dispersion, there is an another character of the band that can affect the property of the material. This character is in fact topology of the band, which can be manifested itself as an integer number that cannot be varied until phase transitions. To explain, let's take an example of well-known a cup-donut explanation of topology. A cup and donut are topologically the same because they can be transformed to each other without producing additional holes to the surface, as shown in Figure 1-7. Then the thing that the cup and donut share in common is the number of holes in the surface. Mathematically, this conservation of the hole number can be stated by Gauss-Bonnet theorem [19],

$$\frac{1}{2\pi}\int_{surface} KdA = 2(1-g) \qquad (6)$$

Here, g is a genus representing the number of holes on the surface and K is Gaussian curvature of the surface. The statement means that total Gaussian curvature of the close surface is an invariant number, genus. Taking this to topological band theory, the closed surface that served by the cup or donut is now presented by the energy band of electron in the momentum space. Then the role of genus in the topological band is now Chern number, which is formulated as follows,

$$\frac{1}{2\pi}\oiint F(\boldsymbol{k}) \cdot ds = C \qquad (7)$$

Similarly, *F* here is Berry curvature which is integrated over the entire first Brillouin zone. At this point, Integral becomes a closed surface integral because the brillouin zone is periodic so that both boundaries can be connected. Figure 1-8 describes the torus result from the rectangular Brillouin zone. With the established analogy between geometrical topological and topological band structure, we now can decide whether the band gaps are topologically different or the same. Generally, topology of the band gap is determined by the sum of Chern numbers of the bands below the band gap of interest.

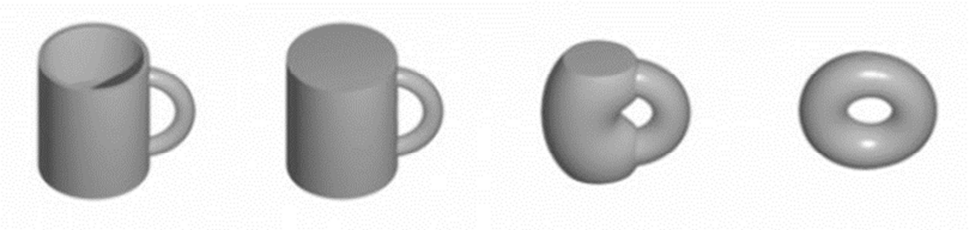

Figure 1- 7. Topological equivalence of a cup and a donut.

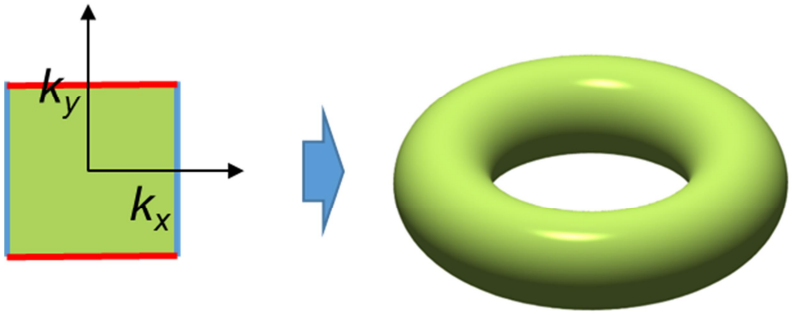

Figure 1- 8. The first Brillouin zone as a torus surface.

1.2.2. Topological edge states

While, the reason why topological insulators are drawing huge interest is that there must be edge states at the boundary between the materials with topologically different band gaps. The origin of the edge states is gap-closing, which results from the fact that two topologically different band gaps cannot be smoothly connected. These edge states are only determined by bulk topology, making it robust against perturbations.

Historically, the quantum Hall effect [20] is the first example of the state with topologically different from ordinary insulators. The quantum Hall effect occurs when a strong magnetic field is applied to two dimensionally confined electrons. At very strong magnetic field, electrons behave like orbital motions with the cyclotron frequency. With an applied electric field, the Hall conductance $\sigma_{xy} = \frac{Ne^2}{h}$ appear and it appears that the conductance is extremely precise and robust against any perturbation. Robustness is originated from the fact that this quantized conductance is the topological edge state of the quantum Hall state, benefitted from the topological protection [21]. The illustration of the quantized edge conduct is described in Figure 1-9. Not long after that, actual material systems exhibiting topologies different from ordinary insulators are demonstrated [22]. In fact, the quantum Hall state states above can present itself only under the condition of breaking of time reversal symmetry. The Chern numbers can be nontrivial values (not zero) only if the system has a broken time reversal symmetry. The applied magnetic field for quantum Hall effect plays a role of breaking time reversal symmetry, which makes the effect impractical for applications. However, actual material systems which have topologically distinct phase and topological edge states were found. The system does not have an explicit time reversal symmetry breaking as a whole system, but two spin subspaces which are connected each other by time reversal symmetry play a role of the topological phases [22, 23]. In this case, time reversal symmetry is required to exhibit topological phases. Therefore, each spin subspace is able to manifest itself nontrivial spin Chern numbers, and protected edge states provided that there is no spin-flipping process. This spin dependent effect is also called as the quantum spin Hall effect as shown in Figure 1-10. Without explicit external magnetic field that allows the integration of Berry curvature nontrivial, the quantum spin Hall effect can occur

with the existence of spin-orbit coupling, which can be considered as a momentum space magnetic field coupling to the spin of the electron.

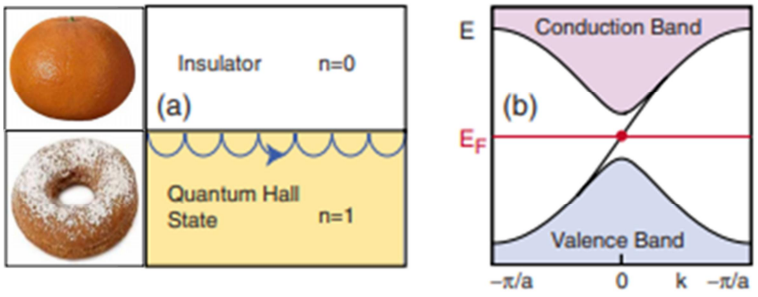

Figure 1- 9. Quantum Hall edge states [19].

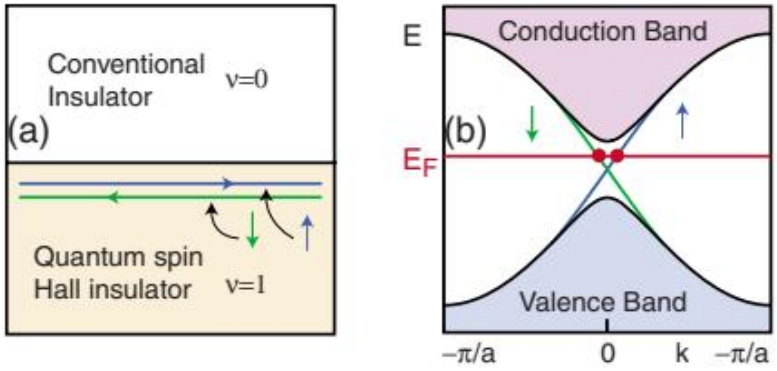

Figure 1- 10. Quantum spin Hall edge states [19].

1.2.3. Topological photonics

With the emergence of topological insulators in condensed matter physics, Haldane and Raghu also suggested that topological band structures are, in fact, the properties that are available not only for electronic systems but also for other wave-particle systems, such as photons [24, 25]. They discovered that the photonic bands can have a nontrivial topology under time reversal symmetry breaking conditions which is the prerequisite for the quantum Hall effect. Time reversal breaking in the photonic systems can be achieved by using magneto optical materials that bear off-diagonal elements to the magnetic permeability tensor [26]. This theoretical suggestion was soon elaborated with the realistic idea that utilized the magneto optical material, ferrite, for the photonic crystal structure and the microwave frequency as an operating regime. Based on this theoretical study, the implementation of the quantum Hall effect in the photonic system was demonstrated for the first time [27]. According to the simulation image and transmission spectrum in the Figure 1-11, light travels only in one direction through the edge of the structure, and it shows startling characteristic revealed from the fact that it passes through the obstacles without being reflected. This demonstration is surprising, but has disadvantages that it can be implemented under the microwave frequency because an external magnetic field is required and the magneto optical effect is weak at the optical frequency. To create more practical devices, the device should not require an external magnetic field and must be able to operate at an optical frequency regime. As in the case of condensed matter physics, the quantum spin Hall effect can be a solution. In the case of photons, unlike the former, spin properties are not inherent, but the problem can be solved by introducing a pseudo spin. Also contrary to the electronic case that only require time reversal symmetry, additional symmetries are required to achieve the spin Hall effect since the bosonic time reversal operator is different from the fermionic time reversal operator. With suitable realization of photonic pseudospins, the external magnetic field can be replaced with an effective magnetic field generated by phases acquired as photons traveling in the unit cell. One of the examples is a micro ring platform where spins can be defined whether the travel direction of the photon is clock-wise or counter clock-wise in the micro ring [28, 29]. Also acquiring a phase through one cycle of traveling a plaquette is realized

by using a link ring and making the position of the link ring shifted to allow photons moving opposite directions to travel slightly different distances as shown in Figure 1-12. Although the scheme seems very promising in the sense that it utilizes a silicon on insulator material which is very practical for semiconductor photonics and operates at the optical frequency regime, the size of the system is relatively large, compared to the operation wavelength, which is not good for high density photonic integrations. Recently, another scheme that can be implemented on a wavelength scale has been proposed [30]. The scheme uses a honeycomb lattice photonic crystal and implements different topological phases by shrinking or expanding a cluster consisting of 6 rods (holes). Figure 1-13 shows such a scheme that exhibits photonic pseudo spin dependent and robust propagation. It should be noted that aforementioned demonstrations are truly benefitted from the virtue of photonics which enables to design and fabricate without many restrictions. In addition to the 2D topological photonic structures, 3D photonic crystal topological insulators were also designed and demonstrated experimentally, showing intriguing properties of 3D topological insulators such as a Weyl point (Figure 1-14).

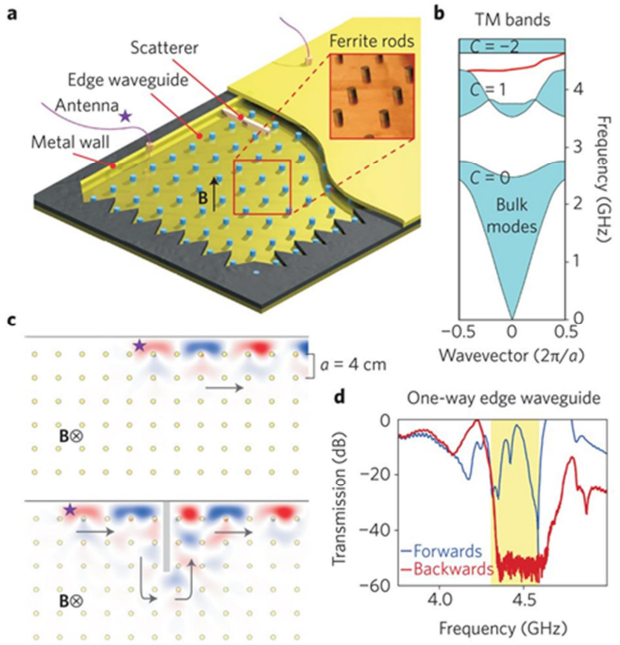

Figure 1- 11. The first demonstration of the quantum Hall effect in photonics [27].

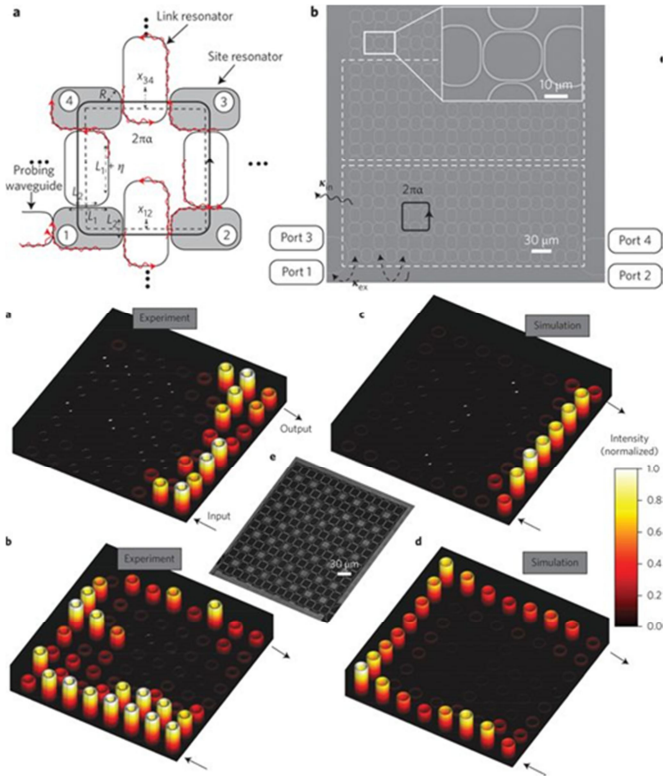

Figure 1- 12. Realization of the quantum spin Hall effect of photonics using mirroring arrays [29].

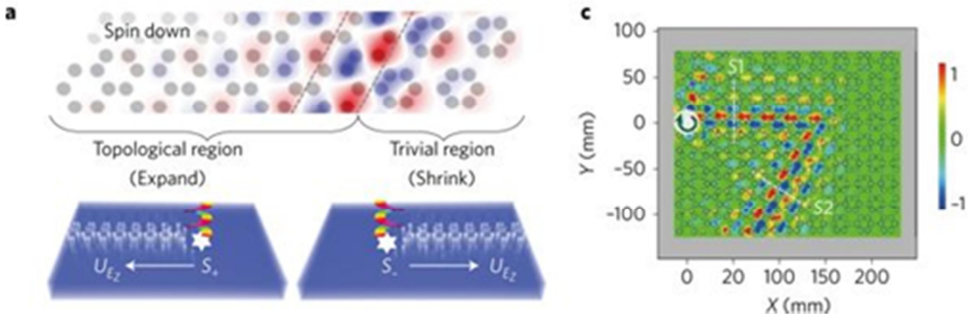

Figure 1- 13. A scheme for photonic spin Hall phases using honeycomb lattice-based photonic crystals [30].

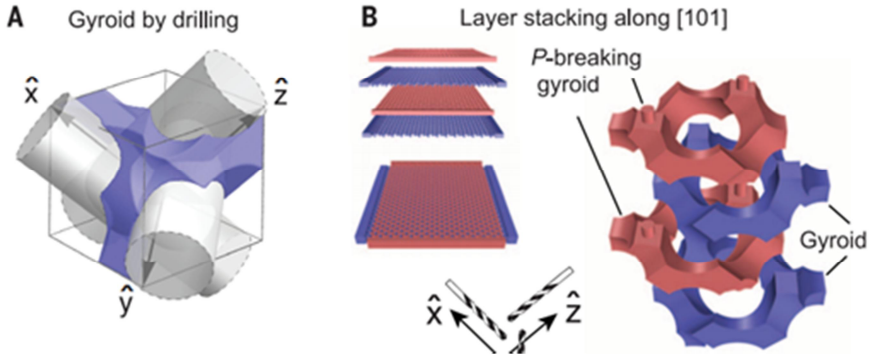

Figure 1- 14. A 3D topological photonic crystal [31].

1.2.4. Topological photonic crystal lasers

Since the aforementioned topological edge states are optical modes, it is possible to amplify the intensity if optical gain is introduced. Laser oscillation is possible if a resonator is formed using a topological edge state and gain exceeding loss is applied. This means that the laser can benefit from the features of the topological edge state. With this in mind, various topological lasers are actively being studied [32-34]. In particular, the 0-dimensional edge state of the 1-dimensional topological insulator can play a role of the resonator by itself, which is useful for the development of lasers. The 1D topological insulator will be introduced in more detail in the next chapter. The ring resonator can be implemented by connecting the beginning and end of the robust one-dimensional edge state of the quantum hall or quantum spin hall insulator mentioned above. Figure 1-15 shows that lasing from ring resonators with arbitrary shapes constructed by the quantum Hall edge states is possible, despite the fact that the magneto optical effect in the optical frequency is very weak, resulting in very narrow topological band gap [35]. It is very fascinating that the shape of the laser cavity can be arbitrary and laser emits only in a single direction. The quantum spin hall edge states can be used for laser oscillations as well [36, 37]. Figure 1-16 shows such a laser and the topological laser shows improved single modeness and slope efficiency compared to a trivial laser.

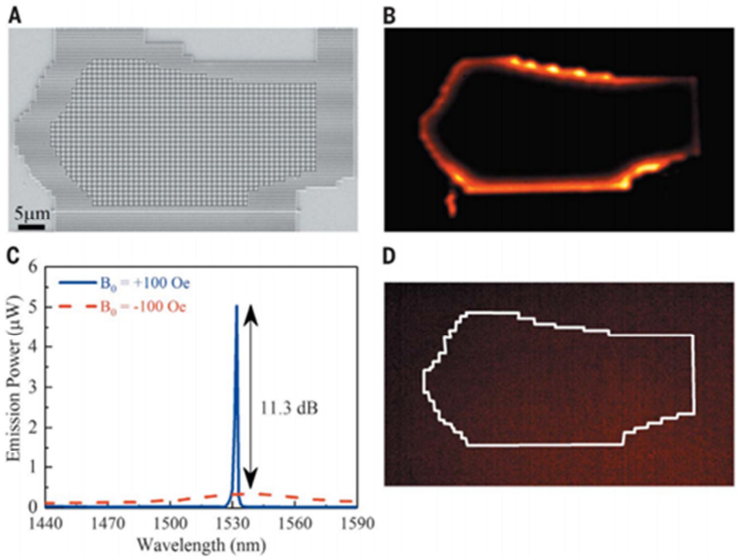

Figure 1- 15. A topological edge state laser using the quantum Hall scheme [35].

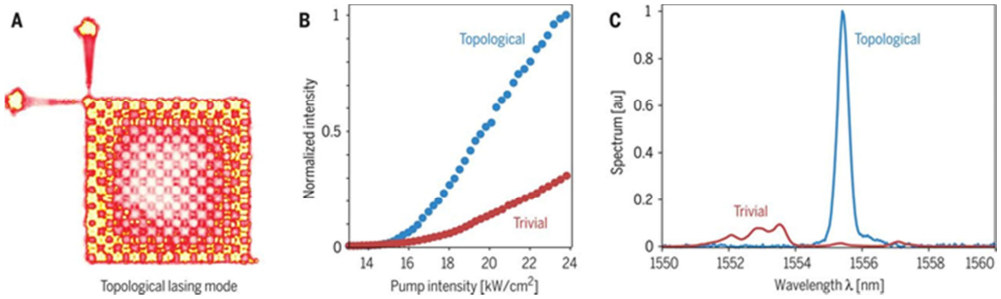

Figure 1- 16. A topological edge state laser using the quantum spin Hall scheme, exhibiting the improved performance [37].

1.3. Outline of the Manuscript

In this thesis, we introduced topological edge states lasers using various topological photonic crystals. Topological photonic crystals were fabricated using a semiconductor gain medium, allowing the identification of the edge states via lasing action.

In the chapter 2, we introduced laser oscillation in the edge state of a one-dimensional array of photonic crystal nanocavities. In an array arranged in the form of Su-Schrieffer-Heeger (SSH) model, topologically different phases and a topological edge state are possible. Here, the characteristics of each state were analyzed spectrally and spatially.

In the chapter 3. we introduced laser oscillation in the hierarchical edge states of a 2D photonic crystal. In the 2D SSH like array, not only 1D edge states (first order), but also 0D corner states (second order) can exist. Laser oscillation from multiple edge states were possible and characteristics of laser modes were also discussed.

In the chapter 4. we introduced a novel triangular shaped laser based on valley photonic crystals (VPC). Robust 1D edge states were able to construct whispering-gallery modes (WGM) despite of sharp turning from the waveguide bends.

Finally, in the chapter 5. the conclusion and the perspectives will be presented.

Chapter 2. Edge mode lasing in a photonic crystal cavity SSH array

2.1. Introduction

2.1.1. Photonic Su-Schrieffer-Heeger model

As mentioned previously, a propagating 1D edge state may exist in a 2D topological insulator. However, the topological insulator is not limited to two dimensions. Emergence of topological photonics regenerates interest of the past one-dimensional model called Su-Schrieffer-Heeger (SSH) model, which was introduced to describe a linear conjugated polymer [38]. It is a one-dimensional chain composed of identical resonators with staggered nearest-neighbor hopping strength as shown in Figure 2-1. A zero dimensional edge state can appear if the chain is arranged in a nontrivial topological phase. For its structural simplicity, the photonic SSH model was extensively studied and its topological edge states were experimentally demonstrated in various platforms; photonic [39], plasmonic waveguides [40], zig-zag resonator chains [41, 42] as shown in Figure 2-2. The model is also conveniently combined with non-Hermiticity in purpose of investigating the behavior of topological edge states in non-Hermitian system [43, 44].

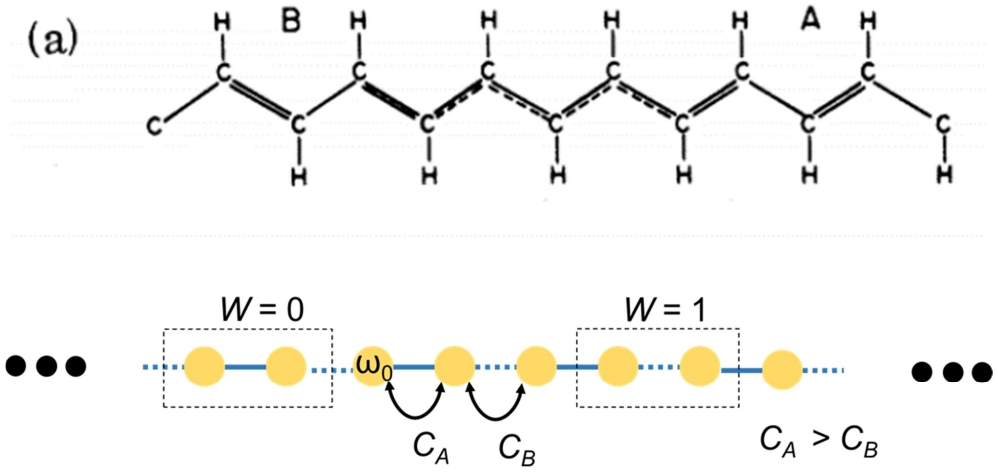

Figure 2- 1. Polyacetylene molecular structure and Su-Schrieffer-Heeger model.

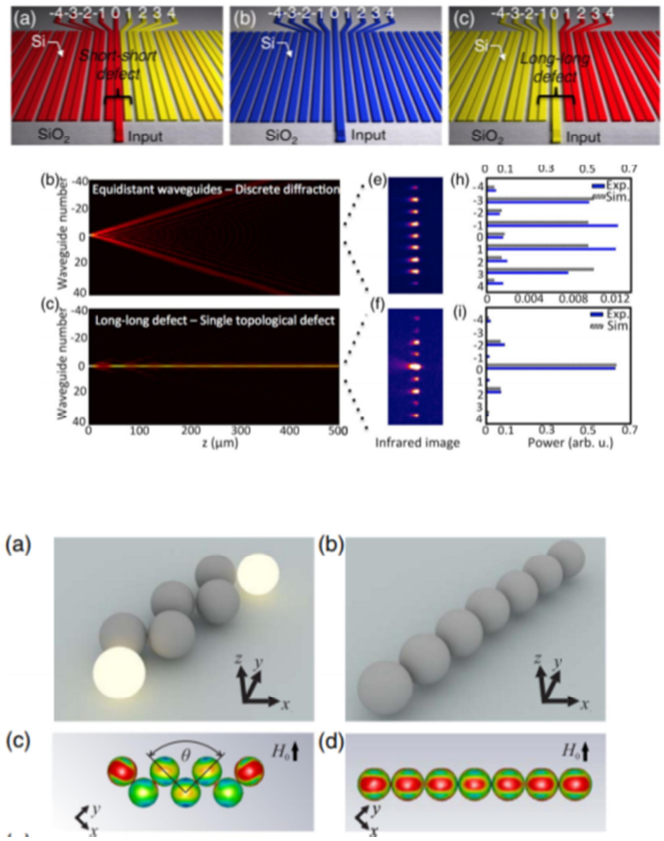

Figure 2- 2. Photonic realizations of the SSH model [39, 42].

2.1.2. Lasing in photonic SSH structures

Lasing in this edge states will also be fascinating for its localization and robustness against disorder. However previously demonstrated lasing in the edge states was relatively large in size, using micro-disk laser array [45, 46], micro-pillar array[47] as shown in Figure 2-3, which limit the possibility for densely integrated systems and harnessing light-matter interaction phenomena such as enhancing spontaneous emission factor which is efficient in cavities with small mode-volume.

In passive waveguide systems, wavelength-scale photonic and plasmonic edge states were observed, but observations were performed through imaging scattered light at the output of waveguides flaring out at each end of the original array or imaging blurred light scattered at the end, which makes their identification harder. So directly observing the edge states at the optical wavelength scale by using near-field measurement is also needed. For these purposes, photonic crystal nanocavities will be a suitable platform because of its high quality factor [48] and small mode volume, which already shows high quality nanoscale lasing [49, 50].

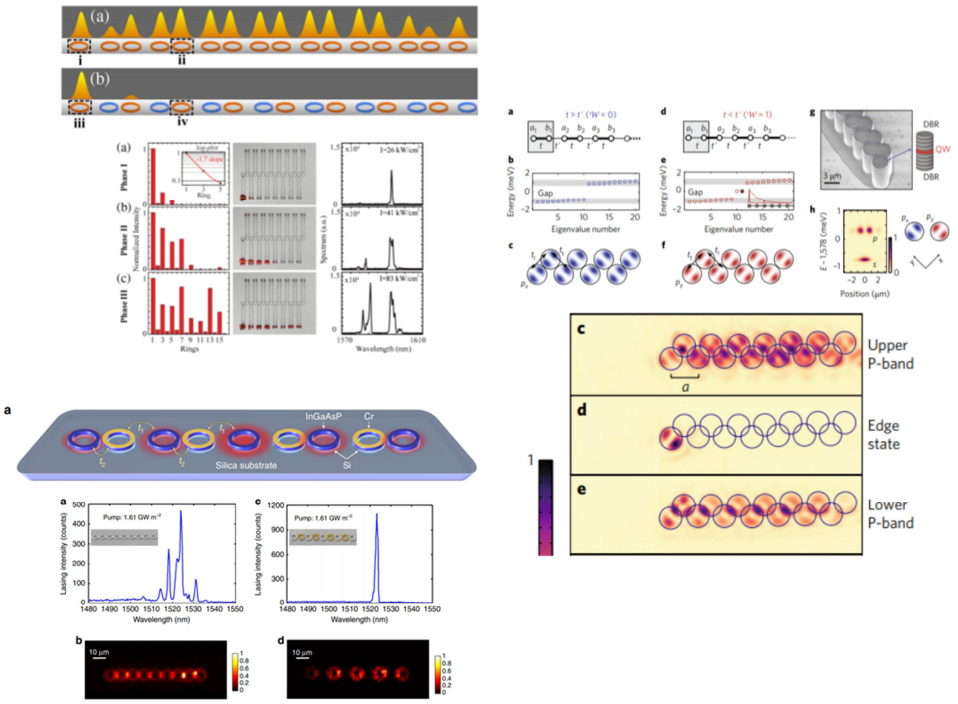

Figure 2- 3. Previous demonstrations on edge state lasing in the SSH array [45-47].

2.1.3. Performance fluctuation on a photonic crystal cavity

In particular, as mentioned earlier, nanophotonic devices are inherently susceptible to process errors. For example, Figure 2-4 shows that the coupling strength of the cavity changes significantly even if only one hole in the coupled cavities changes in size. And Figure 2-5 shows that if identically designed cavities are coupled, in the coupled mode, the mode distribution should be 50 to 50, but due to the process error, it is biased to either side. In the case of topological edge state, it is expected to be a solution even in this case, since the mode distribution of the topological edge state is hardly affected by external perturbations.

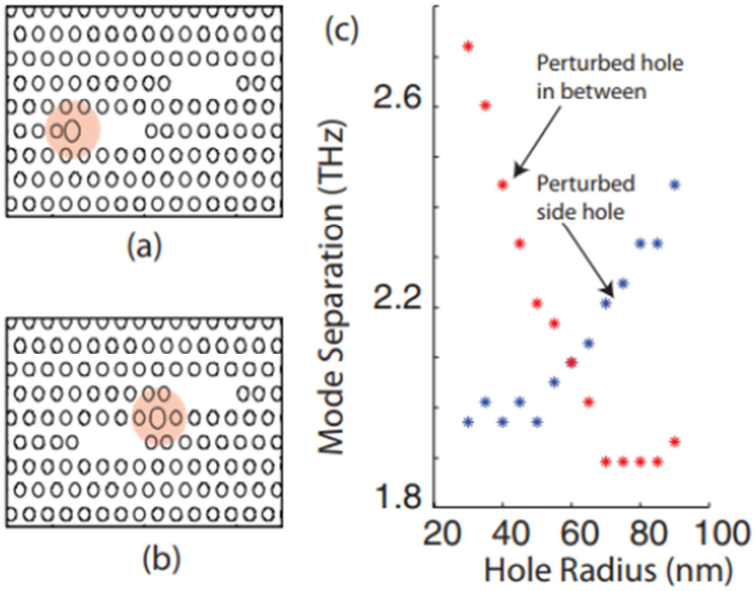

Figure 2- 4. A change of coupling strengths depending on a change of a radius of a single hole [51].

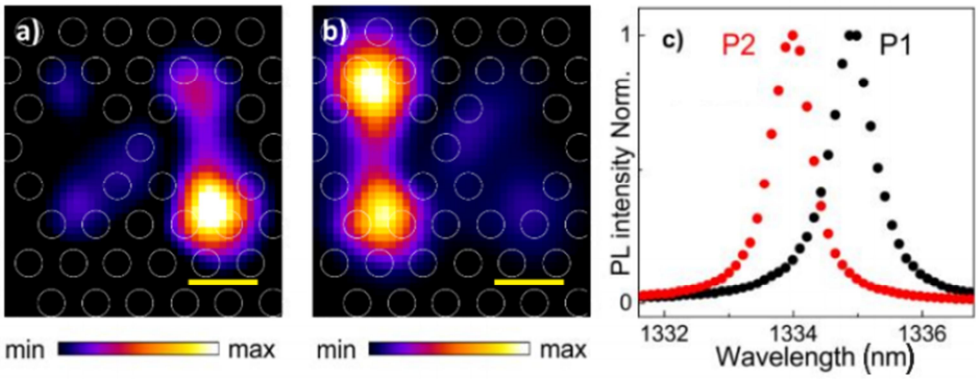

Figure 2- 5. Near-field image of a coupled modes of coupled photonic crystal cavities [52].

2.2. Result

2.2.1. Photonic crystal cavity SSH array

A standard SSH model used in this study is shown in Figure 2-1. It is a one-dimensional chain composed of identical resonators whose resonant frequencies are ω_0, with staggered nearest-neighbor hopping strength (C1, C2 and C1>C2). We realize this configuration in a photonic crystal slab cavity array system by linearly placing L3 cavities with alternating inter-cavity distances, (one column, three columns) to represent staggered nearest-neighbor hopping strengths as shown in Figure 2-6 [53]. The L3 cavity is a photonic crystal cavity created by subtracting three holes in a row from otherwise a perfect hexagonal photonic crystal. Lattice constant (a), hole radius (r) and slab thickness (t) are set to be a=430 nm, r=0.3a and t=230nm and holes at edges of each cavity are shifted and have reduced radius to reduce losses in cavities.

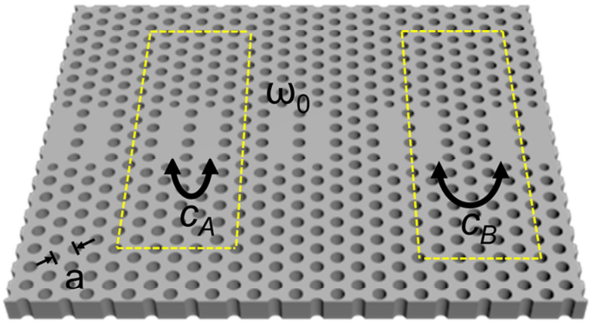

Figure 2- 6. A schematic of the photonic crystal L3 cavity SSH array

2.2.2. Coupling strength control of coupled photonic crystal L3 cavities

When the photonic crystal L3 cavities are brought close together, coupling may occur due to the overlap of the evanescent field of each cavity mode. The coupling strength can be defined as following formula:

$$\kappa = \frac{\omega}{2}\frac{\int \varepsilon_2(r)E_2^*(r)E_1(r)dV}{\int \varepsilon(r)|E_1(r)|^2 dV} \quad (8)$$

With the coupling strength k, eigenfrequencies of coupled modes whose resonant frequency is ω_0 are ω_0+k, ω_0-k. For the case of evanescent coupling in (8), the coupling strength is stronger as each mode overlaps more with another. In this study, we defined stronger coupling as one row apart and weaker coupling as three rows apart. Figure 2-7 shows controlling coupling strength of photonic crystal L3 cavities through simulations. In the case of an isolated L3 cavity, a single resonant mode with a frequency ω_0 is observed. For the cases with coupling, the frequencies of the resonant modes are split, and the splitting is greater as the cavities are more closely located. The splitting of coupled modes is simply $2k$. From this simulation, we confirmed that the coupling strength could be readily controlled by adjusting inter-cavity distances. Note that the center of the coupled modes deviates from ω_0, which will be discussed section 2.2.5.

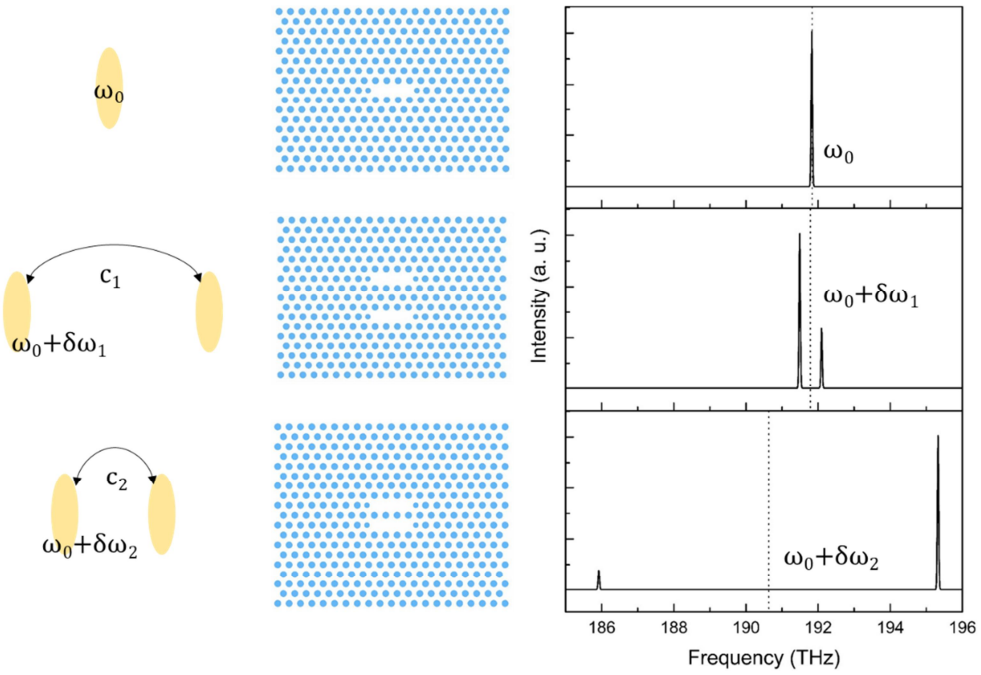

Figure 2- 7. Simulation results of coupled photonic crystal L3 cavities.

2.2.3. Band structure calculation

For an infinite array, a photonic band diagram can be generated by defining the unit cell containing two resonators per cell. In order for a topological edge state to appear, a photonic band gap must exist. To confirm this, we calculated it using two methods: the tight-binding model and the FDTD method using a real structure. For the tight-binding model calculation, we first describe the system in the second quantization language [54],

$$H = \sum_n C_1(a_n b_n^\dagger + a_n^\dagger b_n) + C_2\left(b_{n-1}a_n^\dagger + b_{n-1}^\dagger a_n\right) + \omega_0 a_n a_n^\dagger + \omega_0 b_n b_n^\dagger \tag{9}$$

Here, C1 and C2 means two different coupling constants. $a_n(a_n^\dagger)$ means an annihilation (creation) operator on *a* site of *n*th unit cell. $b_n(b_n^\dagger)$ is for *b* site. A ω_0 is a resonant frequency of the cavity. Then by Fourier transforming of the operators, we can get

$$a_n = \frac{1}{\sqrt{N}}\sum_k a_k e^{-ikna_0}$$
$$b_n = \frac{1}{\sqrt{N}}\sum_k b_k e^{-ikna_0} \tag{10}$$

By substituting (10) to (9), we can get

$$H(k) = \begin{pmatrix} \omega_0 & C_1 + C_2 e^{-ika_0} \\ C_1 + C_2 e^{ika_0} & \omega_0 \end{pmatrix} \tag{11}$$

This is a kernel of the Hamiltonian. Eigenvalues of the Hamiltonian can be obtained as $\lambda = \omega_0 \pm \sqrt{C_1^2 + C_2^2 + 2C_1C_2\cos(ka_0)}$ The eigenvalues represent a dispersion relation, as function of *k*. This is a standard solution for the SSH model [55]. For the numerical band structure with the realistic structure, we define a unit cell as it contains two cavities and has a Bloch boundary condition in one direction and perfect matched layers (PML) in another

direction. The Bloch boundary condition enables to select a specific crystal momentum wavevector, k. Since the structure is considered to be infinite, any combination of cavities for the unit cell is allowed.

Figure 2-8 shows the calculation result of both methods. As a result of the calculation, it was confirmed that the structure can be well described as a tight-binding lattice with the nearest neighbor coupling only because the two results are quantitatively consistent, and that the band gap exists between the two bands. Symmetric two bands are separated by a band gap with magnitude $2|C_1 - C_2|$.

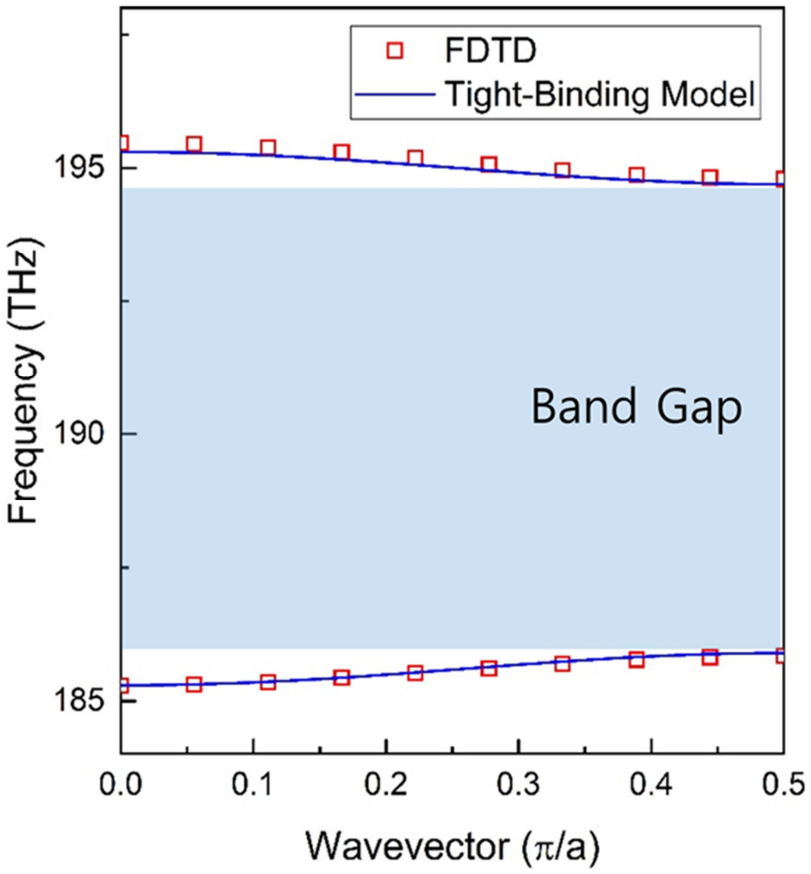

Figure 2- 8. Band structure calculated by FDTD and tight-binding model method.

2.2.4. Topological invariant calculation

The band structure result is irrelevant to the choice of the unit cell. Nevertheless, there are two possible unit cell definitions as shown in dotted boxes in Figure 2-6, one of which is containing two resonators connected by the strong hopping and another is by the weak hopping. The choice of the unit cell definition does not affect the band structure at all so it seems meaningless. However, there can be different finite structures depending on which unit cell is consisting the whole lattice. In fact, distinct topological phases can be determined by this unit cell definition, which is associated to so called winding number W [55]:

$$W = \frac{\mathrm{i}}{\pi}\oint_{BZ} dk \left\langle u_k \middle| \frac{\partial}{\partial k} \middle| u_k \right\rangle \tag{12}$$

Where u_k is a wavefunction of the system in terms of momentum k. For the unit cell with two resonators connected by the strong hopping, the winding number is calculated to be 0, which means a trivial phase. For another unit cell definition, it is calculated to be 1 meaning a nontrivial topological phase and being possible to possess the edge states.

The winding number can be calculated as follows: Starting with the SSH Hamiltonian,

$$\begin{aligned} H(k) &= \begin{pmatrix} \omega_0 & C_A + C_B e^{-ika_0} \\ C_A + C_B e^{ika_0} & \omega_0 \end{pmatrix} \\ &= C_B \begin{pmatrix} \omega_0/C_B & C_A/C_B + e^{-ika_0} \\ C_A/C_B + e^{ika_0} & \omega_0/C_B \end{pmatrix} \end{aligned} \tag{13}$$

we define

$$\rho(k) = C_A/C_B + e^{-ia_0} = |\rho(k)|e^{-i\phi(k)} \tag{14}$$

Where

$$\phi(k) = arctan(sin(ka_0)/(C_A/C_B + cos(ka_0)) \tag{15}$$

Then the SSH Hamiltonian becomes

$$H(k) = C_B \begin{pmatrix} \omega_0/C_B & |\rho(k)|e^{-i\phi(k)} \\ |\rho(k)|e^{i\phi(k)} & \omega_0/C_B \end{pmatrix} \tag{16}$$

from which we obtain the eigenvectors

$$u(k) = \frac{1}{\sqrt{2}} \begin{pmatrix} e^{-i\phi(k)} \\ \pm 1 \end{pmatrix}. \tag{17}$$

The winding number can then be calculated to be

$$W = \frac{i}{\pi} \oint_{BZ} dk \langle u(k) \left| \frac{\partial}{\partial k} \right| u(k) \rangle = \frac{1}{2\pi} \oint_{BZ} dk \frac{d\phi(k)}{dk} = \frac{\Delta\phi}{2\pi}, \tag{18}$$

where $\Delta\phi$ is the accumulated phase of $\phi(k)$, as k evolves across the Brillouin zone.

From the definition of $\phi(k)$, $\phi(k)$ acquires a full phase of 2π ($W = 1$) if $C_A/C_B > 1$, and 0 ($W = 0$) if $C_A/C_B < 1$. Figure 2-9 shows diagrams representing evolutions of phases for two example values of coupling strength ratios. The angle acquire zero phase for a trivial case and 2π phase for a nontrivial case.

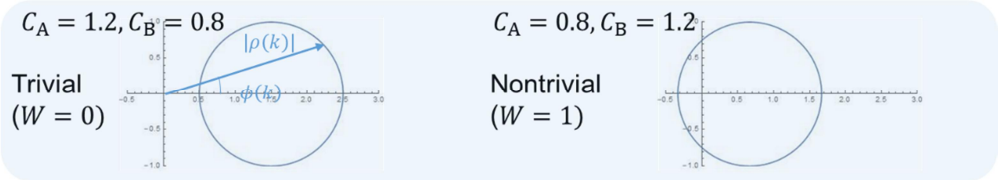

Figure 2- 9. Diagrams of phase factor evolutions for two topologically different cases.

2.2.5. Finite lattice simulation

Based on the calculation of the topological invariant, we consider two types of finite lattices as shown in Figure 2-10, which are both comprised of 10 identical cavities but with different unit cell definitions. Type-1 array is composed of unit cells that have a trivial winding number (W=0), and Type-ll array is composed of topologically nontrivial unit cells (W=0). For the two cases we first conducted a full-3D FDTD simulation to find out every possible resonant mode in these structures. We placed randomly oriented dipole sources at every cavity position and time monitors at the centers of each cavity. Time dependent field signals captured by time monitors are Fourier transformed to generate spectra at each cavity, which enable to investigate resonant modes of the photonic structures.

Figure 2-11 show simulated spectra obtained by Fourier transform of time monitors placed at the center positions of the first five cavities. As expected from previous section, Type-l and Type-ll show a critical difference between each other. A common thing is that two groups of closed spaced resonant modes are observed for both cases, However, for Type-1 array, an isolated resonant mode whose intensity is the strongest at the edge cavity is observed, and its wavelength is in the middle of the wavelengths of the two groups composed of closely spaced modes, but for Type-ll array, there is no isolated mode observed. We can speculate this isolated mode as an edge state and two groups composed of closely spaced modes as bulk states. The green shaded area we expect to be a spectral band-gap region. One thing that should be noted is that the edge state should appear exactly at the center of the band gap due to chiral symmetry of the SSH Hamiltonian, which is different from our FDTD result showing slightly shifted spectral position of the isolated mode. We attribute this to coupling-induced resonant frequency shift which strongly appears in small sized cavities such as photonic crystal nanobeam cavities [56, 57]. This effect will be discussed in detail for the next section. Considering this effect, more realistic tight-binding model can be established. Corresponding eigenvalue plots calculated from this model for both types of arrays are shown in Figure 2-13. Figures clearly show that edge states appear only in Type-ll array and edge states energy is shift from the exact center by consideration of the coupling effect.

For further evidence, profiles of several representative resonant modes calculated by FDTD for

both Type-l and Type-ll arrays are shown in Figure 2-12. The mode profile at the wavelength corresponding to that of the isolated mode shows that its electric field is localized at the edge cavities, but other mode profiles shows the electric field is extended in bulk and diminished at the edge cavity.

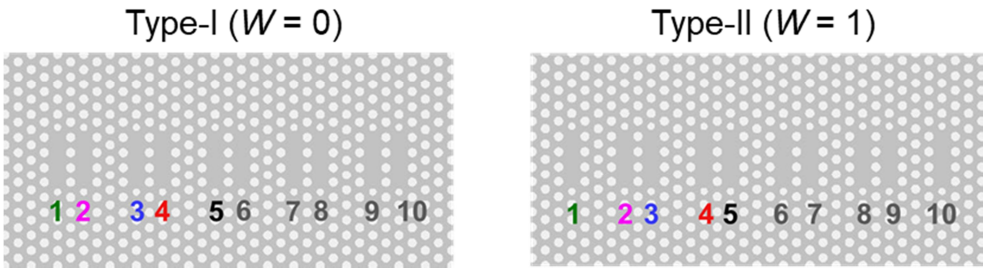

Figure 2- 10. Two different finite array considered for FDTD simulations.

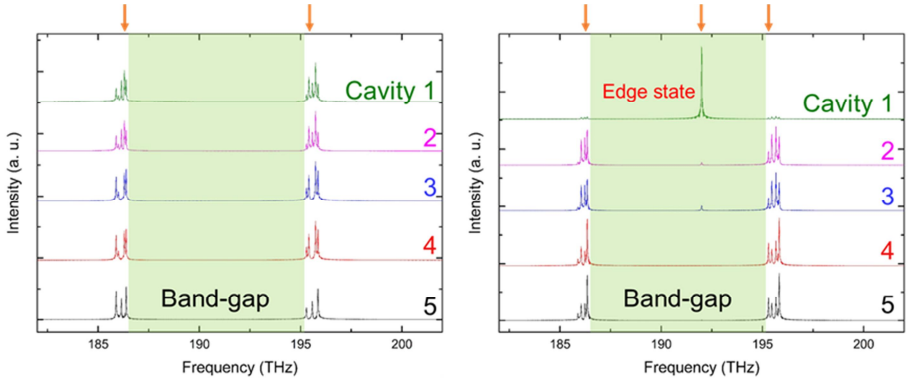

Figure 2- 11. FDTD simulated spectra measured at each cavity site.

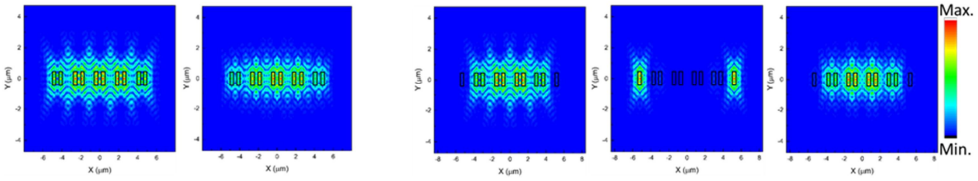

Figure 2- 12. FDTD simulated mode profiles with frequencies indicated arrows in Figure 2-11.

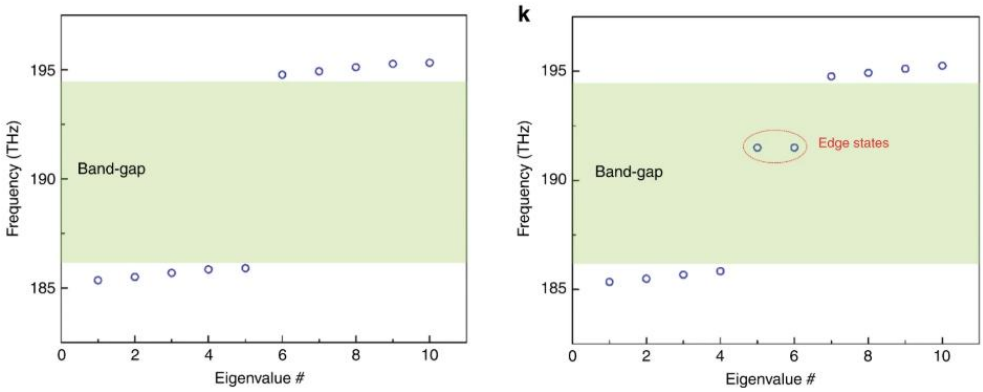

Figure 2- 13. Eigenvalue spectra obtained by tight-binding calculations.

2.2.6. Coupling-induced resonance shift

It is known that the mean frequency of the supermodes in coupled resonators (or an *effective* uncoupled resonance frequency) shifts from the single resonator resonance frequency, which is schematically depicted in Figure 2-7. It is also known that the amount of shift increases as the coupling becomes stronger. To confirm this, we conducted FDTD simulations on a single PhC L3 cavity and coupled PhC L3 cavities with two different coupling strengths. Simulated results clearly demonstrate that the mean value of two resonance frequencies indeed shifts and that the shift gets larger $(\delta\omega_1 < \delta\omega_2)$ as the coupling strength is increased.

We then investigate the coupling-induced resonance shift (CIRS) in our topological array system (Type-1). Taking the frequency shift in coupled cavities into account, the SSH Hamiltonian for a finite coupled cavity array system can be rewritten as

$$H = \begin{pmatrix} \omega_0 + \delta\omega_1 & C_B & & & & \\ C_B & \omega_0 + \delta\omega_1 + \delta\omega_2 & C_A & & & \\ & C_A & \ddots & C_A & & \\ & & C_A & \omega_0 + \delta\omega_1 + \delta\omega_2 & C_B & \\ & & & C_B & \omega_0 + \delta\omega_1 & \end{pmatrix} \quad (19)$$

Note that the cavities in the middle of the array have two nearest-neighbor cavities on both sides so its effective uncoupled resonant frequency is increased by $\delta\omega_1 + \delta\omega_2$ from the single cavity frequency ω_0, while two cavities at the array edges have only one nearest-neighbor so the effective uncoupled resonant frequency is increased by $\delta\omega_1$. Diagonalization of the Hamiltonian results in the eigenvalues (resonant frequencies) and corresponding eigenstates. In Figure 2-13, we compare results with and without the CIRS included in the Hamiltonian. Without the CIRS, the edge states appear exactly at the center of the band-gap because of the symmetry of the system. On the other hand, if the CIRS is included, the edge states shift from the gap center.

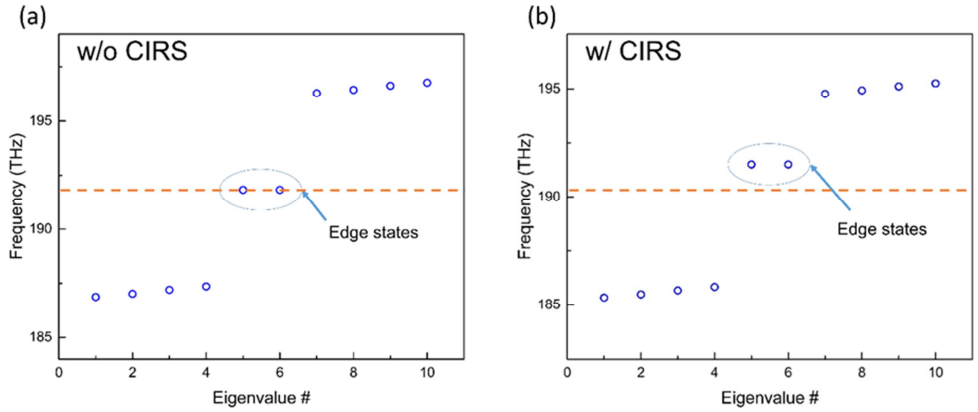

Figure 2- 14. Eigenvalues of the SSH model without (a) and with (b) the CIRS.

2.2.7. Localization of the edge state

The field strength of an edge state of the SSH model is given by an exponential decaying function $\left(\frac{C_B}{C_A}\right)^n = \left(\frac{C_A}{C_B}\right)^{-n}$ [44, 45], where the exponent stands for the n-th unit cell from the edge. We obtain the field profiles of the TES in our system using both FDTD simulations and tight-binding model calculations, which are consistent with each other as shown in Figure 2-15. By fitting the results, we obtain $\sim(14.4)^{-n}$ from the FDTD simulations and $\sim(14.5)^{-n}$ from the tight-binding calculations. The decay rates are slightly slower than $\left(\frac{C_A}{C_B}\right)^{-n} \approx (15.6)^{-n}$. We attribute these discrepancies to the finiteness of actual structure and also to the coupling-induced resonant frequency shift, the latter being explained in the previous section.

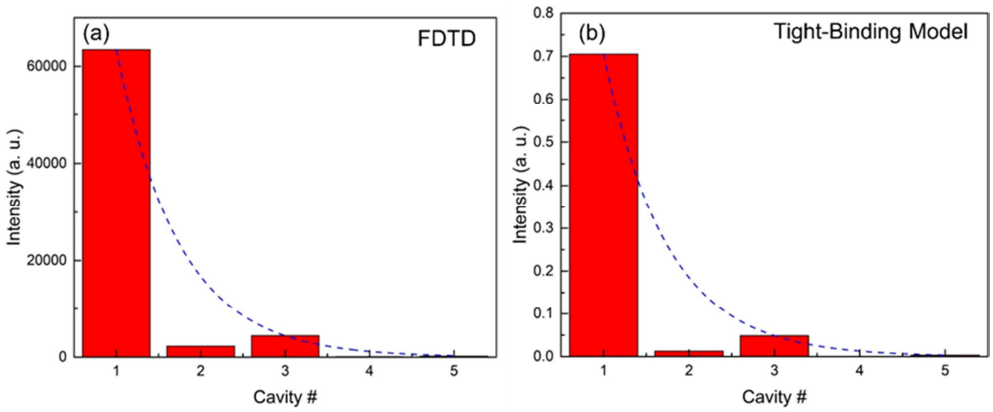

Figure 2- 15. Modal amplitudes of the edge state obtained by the FDTD simulation (a) and tight-binding model calculation (b). The dashed lines are exponential fitting curves.

2.2.8. Sample fabrication

To experimentally observe lasing in edge states in our system, we employed the InAsP multiple quantum well active gain medium and used the electron-beam lithography to draw photonic crystal cavities. A schematic of the process flow is presented in Figure 2-16. First, the InP substrate containing multiple quantum well slab is flip-bonded to a glass substrate. A molecular bonding method is used, requiring oxide deposition formerly [58]. Then the InP substrate is removed by wet etching using a HCl solution. A Si_3N_4 hard mask with thickness of ~30 nm is deposited on the InAsP slab using PECVD. To form the pattern, a standard electron-beam lithography is used. A ZEP520A positive e-beam resist is spin coated followed by coating of an adhesion promotor HMDS. After the e-beam resist is exposed, it is developed and subsequently RIE etching is conducted to transfer the pattern to the multiple quantum well slab. For etching of the Si_3N_4 hard mask, oxygen and CF4 gases are used. CH_4 and H_2 gases are used to etching the InAsP/InP slab. During etching of the InAsP slab with that recipe, byproducts are formed and should be removed by oxygen plasma to prevent saturation of the etch rate. Figure 2-17 shows a magnified view of SEM of the completed sample.

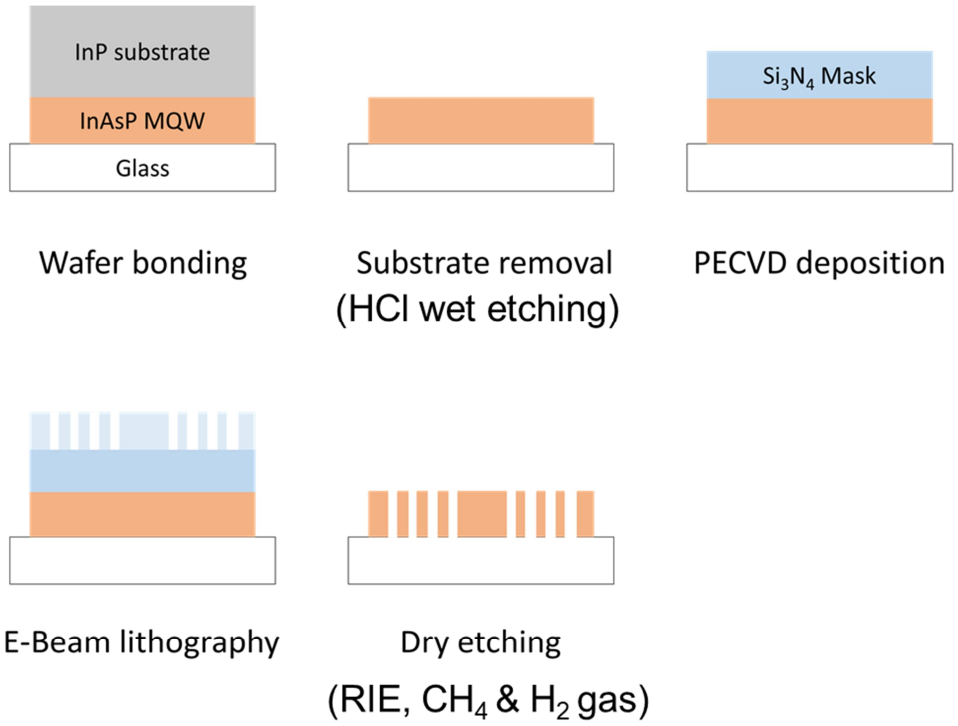

Figure 2- 16. Fabrication process

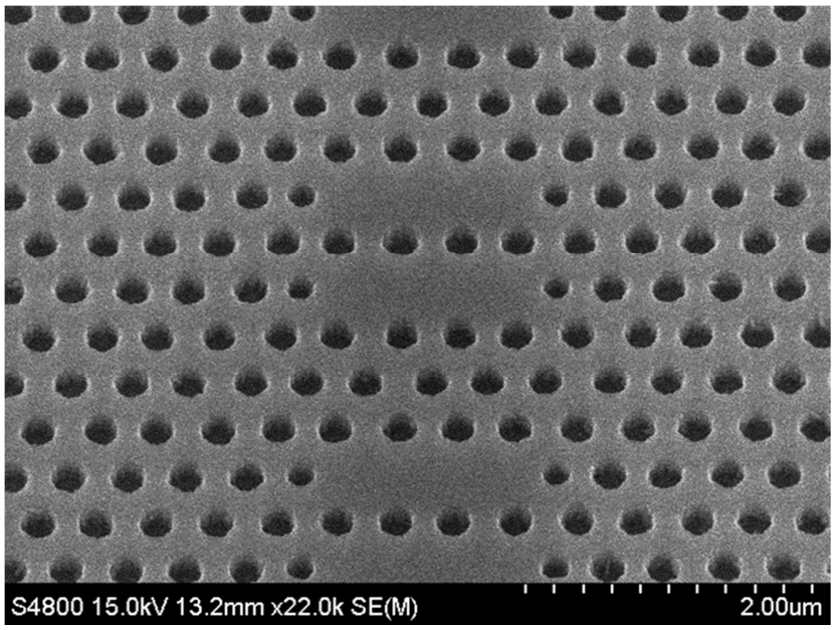

Figure 2- 17. A scanning electron micrograph of the fabricated sample

2.2.9 Micro-photoluminescence measurement

The two topologically different finite arrays that was considered in the simulations are fabricated and SEM images are shown in Figure 2-18. The devices are optically pumped and the radius of pump beam spot is about ~5 μm. The pump laser wavelength is 1064 nm and the laser operation is pulsed with the repetition rate of 500 kHz and pulse width of 20 ns. When pumped with sufficient fluence, both types of devices exhibit lasing oscillation. Interestingly, for Type-ll devices, pumping at two different positions (Spot 1 is at the center and Spot 2 is at the edge of the device) causes lasing with totally different wavelengths depending on the positions (~195 THz for the edge, ~199 THz for the center), whereas for Type-1 devices, lasing occurs at similar wavelengths (~199 THz) for two different pumping position (Figure 2-19). Schematics of the optical pumping geometry for different positions (edge and center) of the spot is shown in inset. Considering the spatial overlap of the pumping spot and the mode profile, we can speculate that the strongest lasing mode observed when pumped at the edge of the device is the edge state we have been looking for. On the other hand, other lasing modes are expected to be originated from bulk states of the SSH array. Furthermore, bulk state spectra present multiple lasing modes, which means that these multiple modes correspond to the components of the mode group revealed in the simulation.

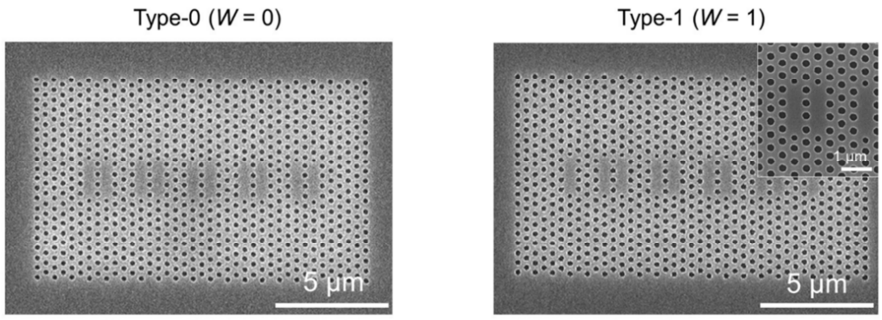

Figure 2- 18. SEM images of fabricated devices with different topological invariants.

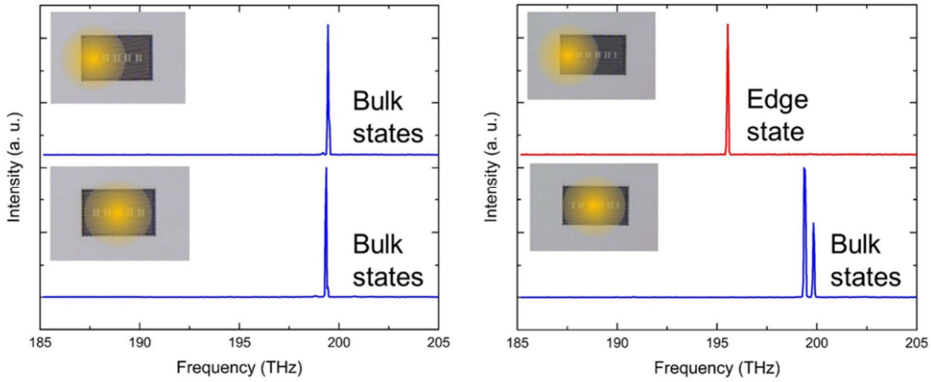

Figure 2- 19. Measured photoluminescence spectra for the two types of the devices. Inset shows a schematic of pumping geometry.

2.2.10. Near-field scanning microscope measurement

For directly observing the edge states, we conducted scanning near-field optical microscope (SNOM) measurements which enable direct observations of the spatial distribution of lasing modes [58, 59]. A schematic of the SNOM measurement setup is shown in Figure 2-20. A 980 nm pump laser is illuminated onto the devices from the back side of the sample through the transparent glass substrate. An optical fiber tip, tapered to nanometer scale for sharpness, is scanning over the surface of the device and interacting with the evanescent fields of the lasing mode. Unlike conventional photoluminescence (PL) measurements which could only collect light escaping from the slab, SNOM allows direct interaction with the evanescent fields that cannot be seen normally by PL measurements and measure the mode with the resolution beyond diffraction limit.

A right panel in Figure 2-21 is measured SNOM data for the Type-ll device at different lasing modes occurred for both pumping positions. Clearly, the lasing mode we speculated as the edge state is indeed localized at the edge cavity and other lasing modes show that their intensity distributions are extended over several cavities, diminishing at the edge cavity. On the other hands, none of the lasing modes in Type-l devices does not appear to be strongly localized at the edge. Also It is observed that the bulk modes in the Type-l devices can extend to the edge cavity, which tells that this have different topological phase from the Type-ll structure.

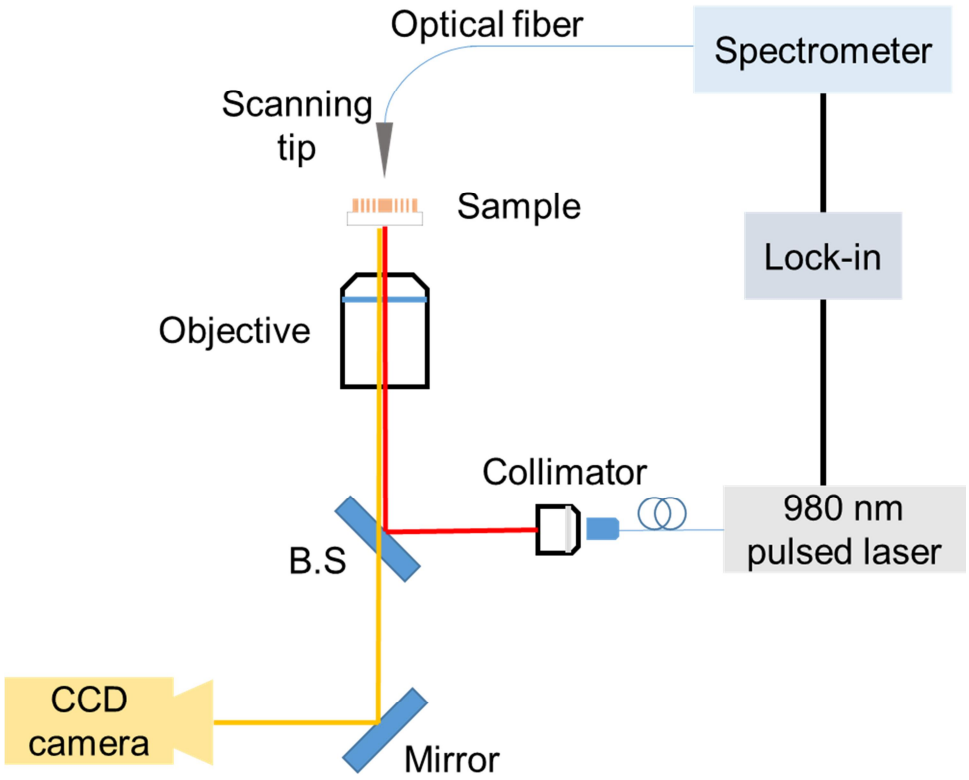

Figure 2- 20. A schematic of the SNOM measurement setup.

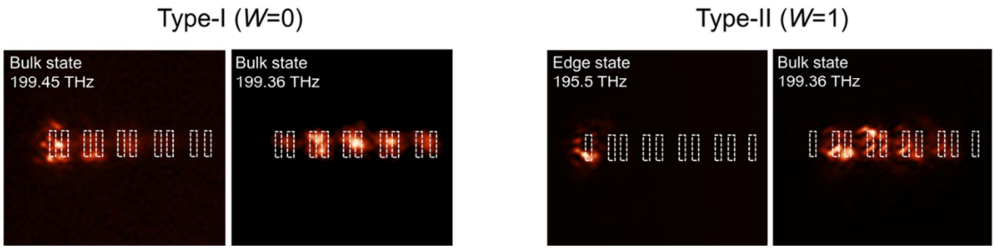

Figure 2- 21. SNOM images of the lasing modes corresponding to Figure 2-19. Dashed rectangles represent the positions of the L3 cavities

2.2.11. Lasing characteristics of the edge and bulk modes

We measured the change in the output intensity according to the pump intensity in the bulk lasing mode and the edge lasing mode of the devices. As shown in Figure 2-22. threshold behavior, which is characteristic of lasing oscillation, was well observed, and the threshold value was lower for the edge state (~13 kW/cm^2) than for the bulk state (~23 kW/cm^2), and the slope efficiency which is the increment of output power to the increment of input pump power was higher for the bulk state. From the calculated quality factors shown in Figure 2-23, it can be inferred that the edge states have lower threshold due to its higher Q factor (and lower mode competition), and in the bulk state, it is considered that the slope efficiency is greater because the mode volume is larger.

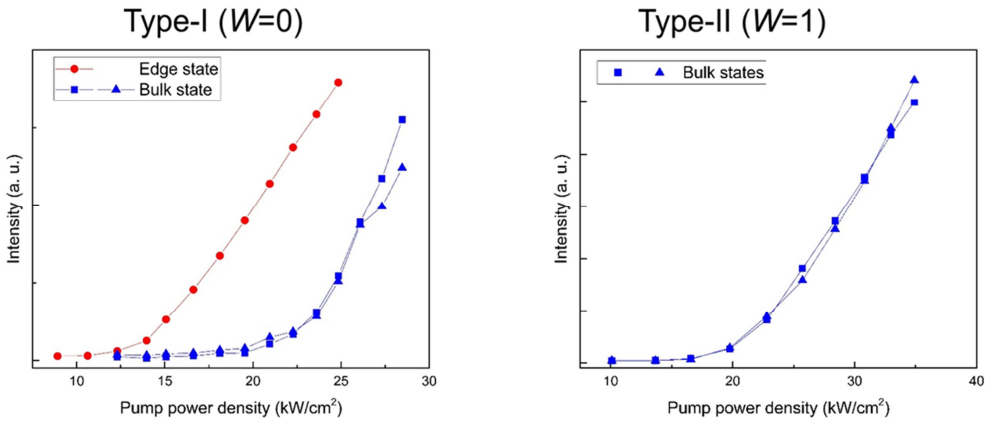

Figure 2- 22. Output intensities as function of pump power density for both types of devices. Edge and bulk states are presented as red and blue colors.

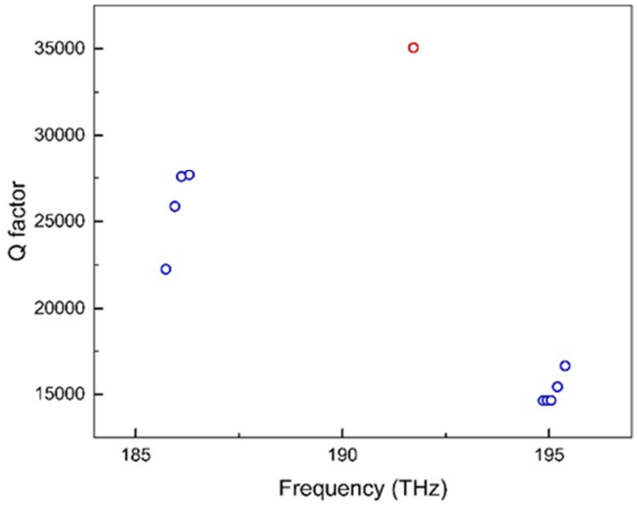

Figure 2- 23. FDTD calculated quality factors of the modes of the Type-1 device. A red dot represents the edge mode and blue dots for bulk states.

2.2.12. Spontaneous emission factor of the edge mode

We calculated the beta factor, which is the ratio of photons that contributes to the laser mode in spontaneous emitted light to the total spontaneous emitted light. The beta factor is a factor considered to develop a thresholdless laser [50, 60, 61] because a high *Q/V* ratio in a high-beta laser weakens the threshold phenomenon of the laser. If 1, it means that every spontaneous emitted photon contributes to the lasing mode, enabling to observe a sharp peak even at very low excitation power. A widely used method to extract the beta factor is by putting the beta factor as a fitting parameter of the laser rate equations,

$$\begin{aligned} \frac{dN}{dt} &= \frac{\eta L_{\text{in}}}{\hbar\omega_{\text{pump}} V_{\text{a}}} - \left(\frac{v_s}{d_{\text{a}}} N + BN^2 + CN^3\right) - \Gamma \frac{g_0 c}{n_{\text{eff}}} ln\left(\frac{N}{N_{\text{tr}}}\right) P \\ \frac{dP}{dt} &= \Gamma \frac{g_0 c}{n_{\text{eff}}} ln\left(\frac{N}{N_{\text{tr}}}\right) P - \frac{P}{\tau_{\text{p}}} + \beta BN^2, \end{aligned} \tag{20}$$

and extracting the factor by fitting (20) to the measured light-in light-out curve. The result of fitting is shown in Figure 2-24 and parameters used for the laser rate equations are shown in Table 2. The fitted beta factor is ~0.15, which is quite high thanks to a high *Q/V* value. It should be noted that a cold-cavity Q factor can be experimentally measured as shown in Figure 2-25 by fitting the peak with the Lorentzian curve, when pumped just below lasing threshold regime (transparent regime).

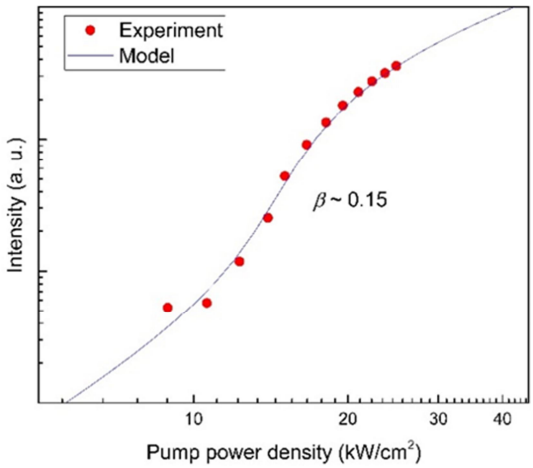

Figure 2- 24. Light-in light out curve fitted with laser rate equations. An estimated beta factor is presented.

Table 2. Parameters used for the laser rate equations

η (Absorption of pump)	0.15
Γ (Confinement factor)	0.175
τ_p (Photon life time)	$0.3 \times 10^{-9}\ s^{-1}$
g_0 (Gain coefficient)	$1500\ \mathrm{cm}^{-1}$
B (Bimolecular recombination rate)	$1.0 \times 10^{-10}\ \mathrm{cm}^3\ \mathrm{s}^{-1}$
C (Auger recombination rate)	$5.0 \times 10^{-29}\ \mathrm{cm}^6\ s^{-1}$
N_{tr} (Transparency carrier density)	$1.0 \times 10^{18}\ \mathrm{cm}^{-6}$
v_s (Surface recombination velocity)	$3000\ \mathrm{cm\ s}^{-1}$
d_a (Propagation distance for surface recombination)	2.0×10^{-5} cm
n_{eff} (Effective refractive index)	2.5
V_a (Active volume)	$2.6 \times 10^{-11}\ \mathrm{cm}^3$

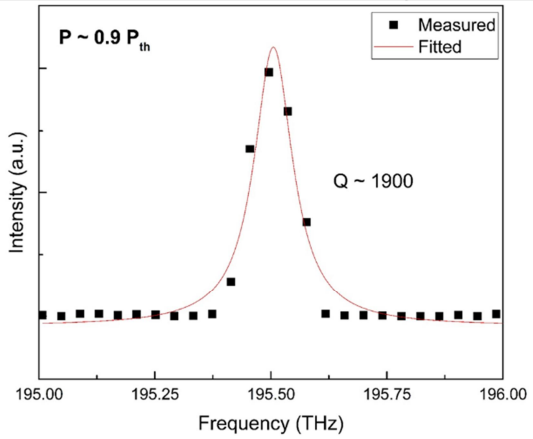

Figure 2- 25. A measured PL spectrum just below threshold (dots) and Lorentzian fitting curve (line).

2.2.13. Chiral symmetry

Chiral symmetry implies there is some unitary (local) operator Γ that anti-commutes with the Hamiltonian. For example, the SSH Hamiltonian possess the chiral symmetry defined by the Pauli matrix [47, 53].

$$\{H(k), \sigma_z\} = 0 \tag{21}$$

The consequence of the chiral symmetry is that the spectrum is symmetric; every eigenstate u_{E} with energy E has a partner eigenstate Γu_{E} with energy –E. This statement also implies that if the edge state of the SSH model exists and has a zero energy, it should appear in pair. Figure 2-26 shows examples of spectrum of the SSH model that in general, has the chiral symmetry which causes symmetric spectra for the cases of various parameters.

Another definition of the chiral symmetry is the sublattice symmetry. The sublattice symmetry means that If the lattice can be divided by two sublattices, A and B, with hopping appearing only between these two different sublattices, then the lattice has chiral (sublattice) symmetry. In other words, for the Hamiltonian matrix in block form:

$$H = \begin{pmatrix} H_{AA} & H_{AB}^{*} \\ H_{AB} & H_{BB} \end{pmatrix} \tag{22}$$

if chiral symmetric, no interaction between atoms in the same sublattice means that, $H_{AA} = H_{BB} = 0$ resulting in,

$$H = \begin{pmatrix} 0 & H_{AB}^{*} \\ H_{AB} & 0 \end{pmatrix} \tag{23}$$

The sublattice symmetry will be revisited for the 2D SSH model discussed in Chapter 2.

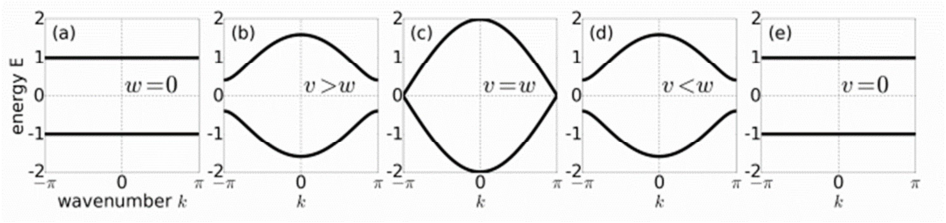

Figure 2- 26. Chiral symmetric band structures of the SSH model.

2.2.14. Robustness of the edge state

Robustness of the edge states is another important feature to be considered. It is well known that due to the chiral symmetry of the SSH Hamiltonian, perturbations which respect the chiral symmetry such as disorder in hopping strengths does not affect the edge states. And it is also investigated that even if perturbations such as modifying on-site energies of the edge sites break the chiral symmetry, the localization is maintained to some extent. In this study, we investigated robustness of the edge state against fabrication errors. First, through calculations, the coupled modes of two coupled cavities and the topological edge mode in the SSH-coupled cavities were compared. At this time, the same amount of random numbers of the general nanofabrication error level were applied to the cavity on-site energy ($\delta_i = 0.01\gamma\xi_i\omega_0$) and coupling strength ($\varepsilon_i = 0.1\gamma\xi_i C_{\mathrm{A/B}}$) for both cases as shown in Figure 2-27. We set the maximum level of the random numbers as 10% and 1% of the original coupling strength and on-site energy, respectively. As a result of the analytic calculation, the mode distribution of the simple coupled modes changed significantly as the random parameter value increased, but in the case of the topological edge state, it was confirmed that the mode distribution hardly changed. To verify the robustness of the topological edge mode experimentally, we compared the bulk state and edge state of several identically designed devices (but differently fabricated due to fabrication errors). Figure 2-28 shows that in the case of a bulk state, due to fabrication errors, the number of laser modes and the relative intensity differ from device to device, and the mode distribution also varies from device to device. On the other hands, in the case of the edge state, despite fabrication errors, the modes were always well localized in the edge cavity and showed a single mode.

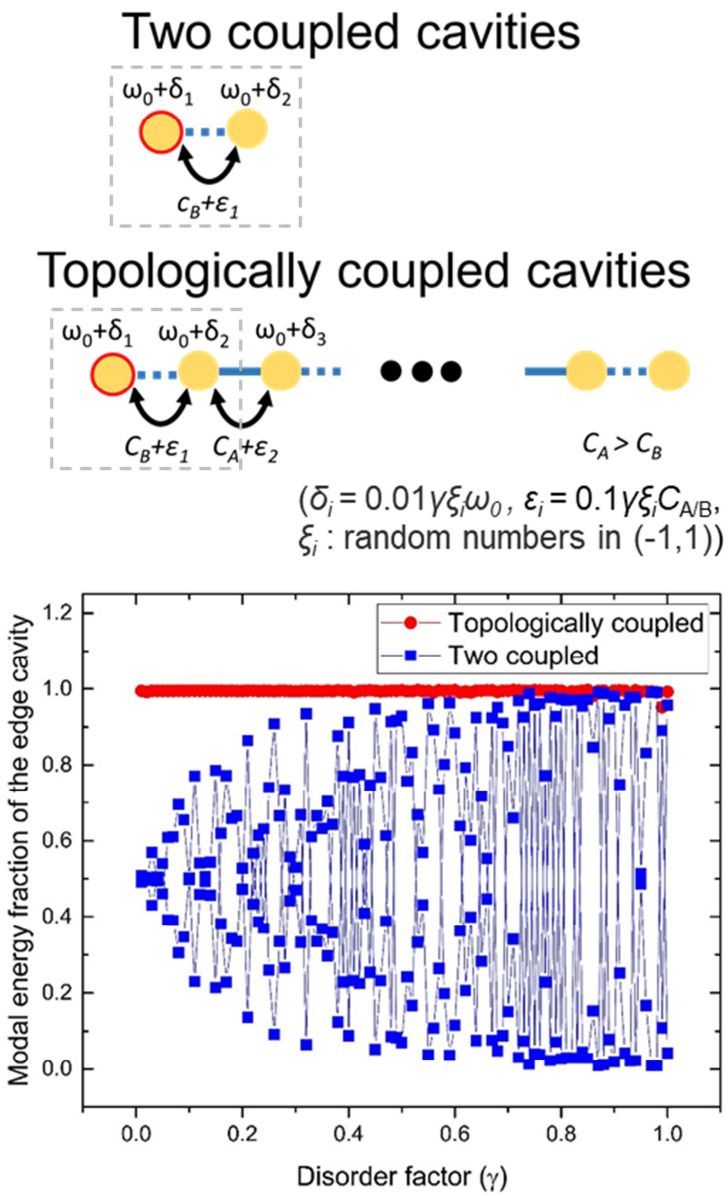

Figure 2- 27. Comparison of the mode distribution between coupled modes and topological edge mode.

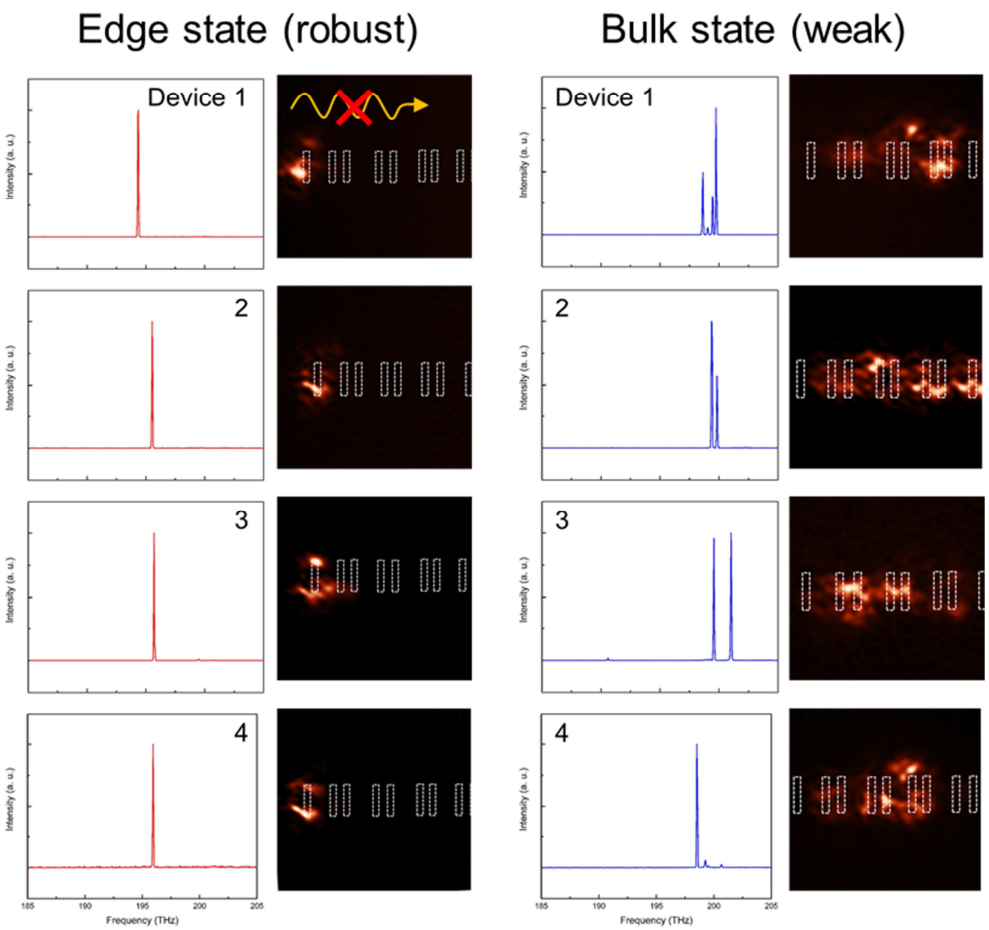

Figure 2- 28. Measured lasing spectra of the edge and bulk states for identically designed devcies.

2.2.15. Edge states in topological kink

Edge states can exist also in the middle of the array. If a kink is introduced in the SSH array as shown in Figure 2-29, the array can be considered to be composed of two topologically different arrays which are able to generate the topological edge state at the interface of the two. We have fabricated such an array and the SEM image is shown in Figure 2-29. When we optically pumped the device at the center of the array, we observed a single mode lasing action as shown in Figure 2-29. Furthermore, we also confirmed by the SNOM measurement that the lasing mode is indeed topological edge state. The lasing mode is strongly localized at the kink cavity which sit in the middle of the array.

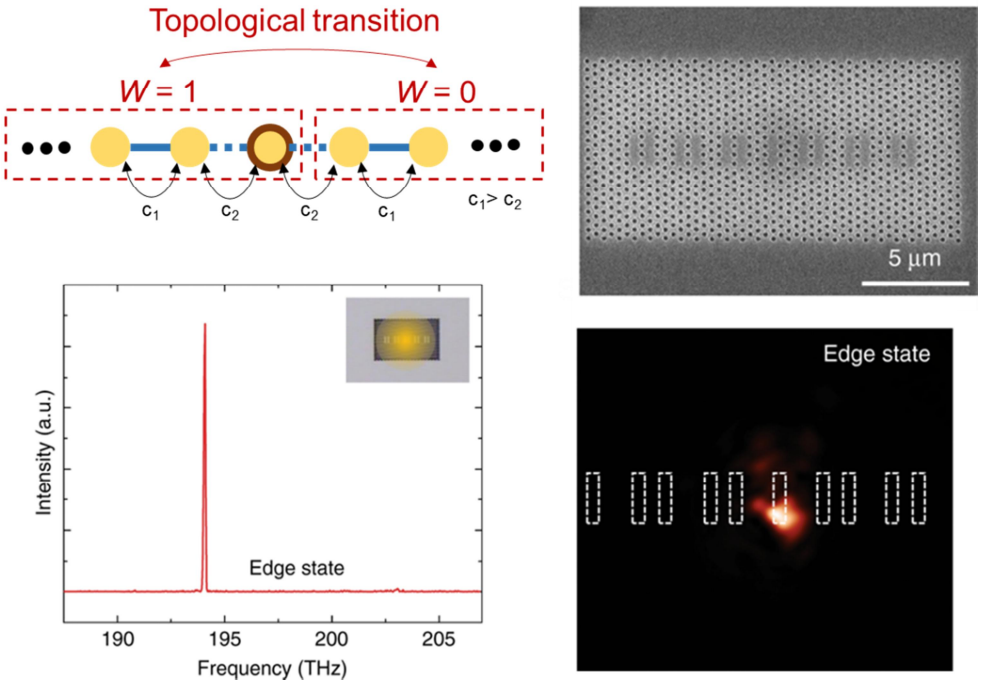

Figure 2- 29. Edge state lasing in the middle of the array.

2.3. Conclusion

In conclusion, we theoretically and experimentally demonstrated the edge states in one dimensional lattices composed of photonic crystal L3 nanocavities. A straight-forward FDTD method applied to optical photonic crystal structures showed wavelength-scale edge states could be formed depending on the type of unit cells. In experiment, adopting active gain material, lasing in this edge states were observed and spectral results were critically different by topology of the structures. The SNOM measurements provided the direct evidence that lasing indeed occurred at the edge states and also showed that these edge states were robust against fabrication errors. Our results unambiguously demonstrated such topological edge states can exist and even be possible to lase at wavelength-scale photonic crystal cavities which is technologically demanding for more densely integrated photonic systems. And it is also opening the way for more interesting subjects related to the photonic crystal such as slow-light waveguides [62], strong light-matter interactions [63], nanoscale sensing etc., which can be combined with intriguing topological properties

Chapter 3. Higher-order topological edge states lasers

3.1. Introduction

3.1.1. 2D SSH lattices

The one dimensional SSH model can be extended to two dimensions. If the coupling strengths appear alternately in the added dimension, it will become the following lattice structure as Figure 3-1 [64]. In such a structure, it can be expected that an edge state which is the zero dimensional edge state of the SSH model is extended one-dimensionally. However, even though this edge state is one-dimensional, unlike the one-dimensional edge states of the typical Chern insulator, the propagation characteristics are not topologically protected and it is the same as a general waveguide which suffers from backscattering by disorder or bending of the waveguide. Therefore, two-dimensional (2D) structures with Chern type insulators (Chern, Z_2, valley Chern) are the main platforms to be employed and studied because they not only facilitate easy device fabrication but also enable to study photonic analogues to many fascinating 2D quantum electronic phenomena, such as quantum (spin) Hall effects. In fact, most of the studies on topological photonics so far have dealt with the one-dimensional (1D) topological edge states (TESs) of the 2D structures, with the main emphases on their propagation characteristics, except that the confined topological state, zero-dimensional (0D) TESs of the SSH model have been studied as well, which has expanded our view point on TESs from wave transportation to confinement and trapping. However, aforementioned 2D SSH lattice initiates another fascinating topic of topological insulators, which will be described in the next section.

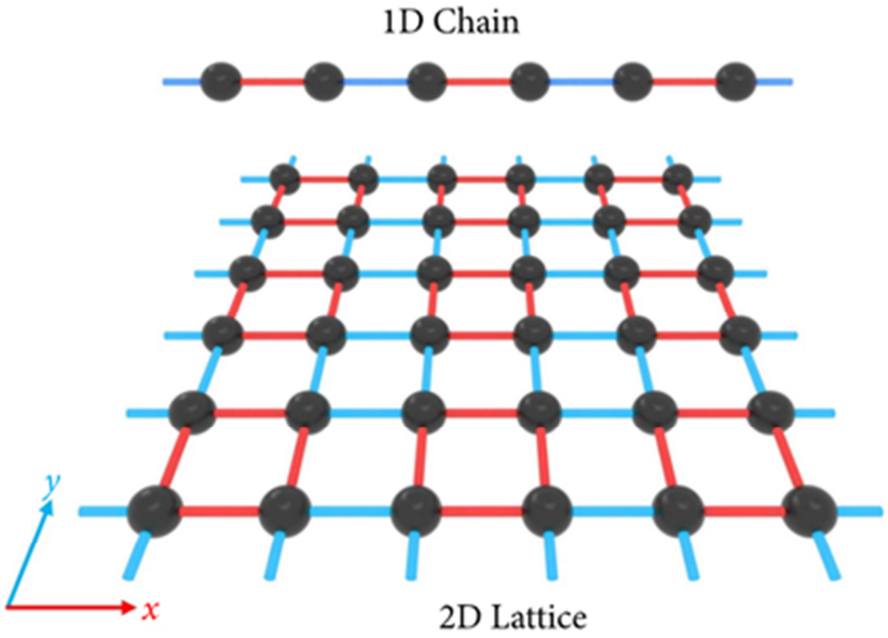

Figure 3- 1. An example of the 2D SSH lattice [64].

3.1.2. Higher order topological insulators

Recently, a new concept of TIs, higher order TIs (HOTIs) has been suggested, which stated that a d-dimensional bulk can possess edge states of the dimensions less than (d-1) as shown in Figure 3-2. In the case of the 2D HOTI, it may have 0D edge states (corner states). the first proposal of HOTIs is about utilizing multipole moments of the bulk, as shown in Figure 3-3 [65]. HOTIs based on quadrupole moments of the 2D bulk have been suggested and experimentally demonstrated in various systems such as mechanical resonators [66], electrical circuits [67, 68] and photonic microring arrays [69]. In short, the proposed quadrupole moment HOTI appears by adjusting the coupling phase so that the unit cell can acquire the π gauge flux in the 2D SSH array. While, it has also been proposed that HOTIs can be built without multipole moments [70-76]. In this case, nontrivial topology is characterized by bulk polarizations, (equivalently, Wannier centers) and higher order topological edge states are formed in a hierarchical manner. For example, the 2D bulk with nonzero polarizations induces the 1D edge states and the 0D corner states can be formed if the two 1D edge states with nonzero polarization meet. This kind of HOTIs were realized at systems where quadrupole moments are hard to be achieved. Figure 3-4 shows several examples of HOTIs in various systems and corresponding higher order edge states.

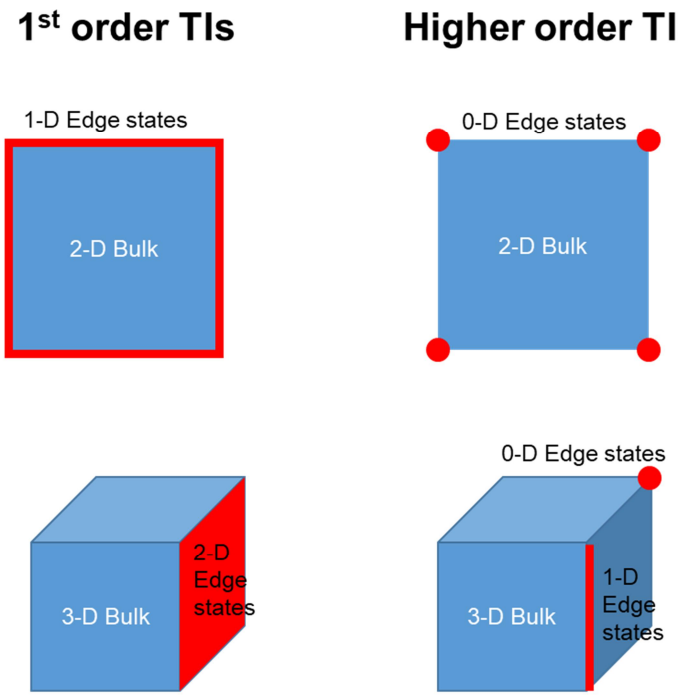

Figure 3- 2. A schematic description of HOTIs and conventional Tis. Edge states are depicted by red color.

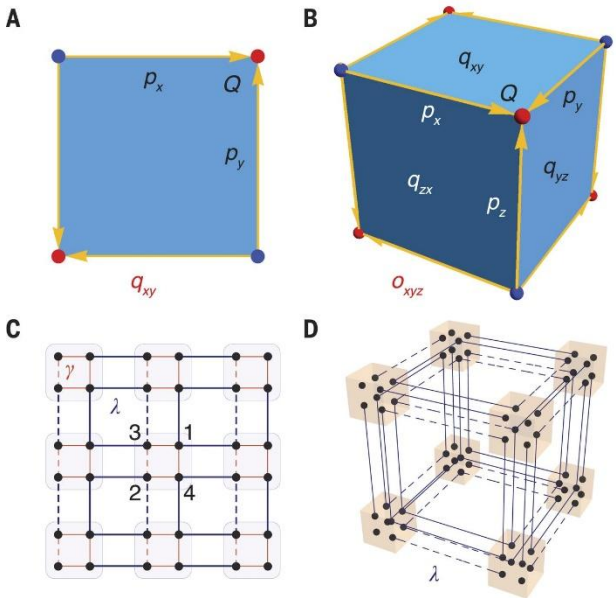

Figure 3- 3. Mechanisms of formation of HOTIs by multipole moments [65].

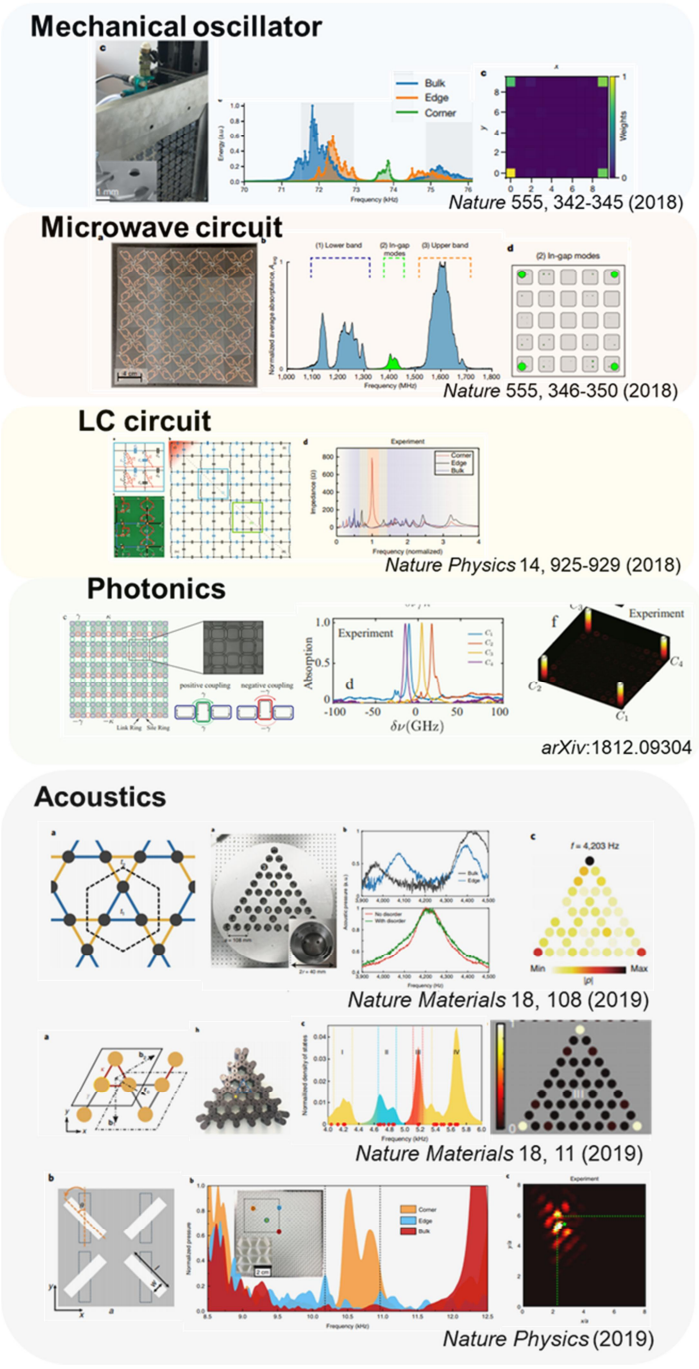

Figure 3- 4. Demonstrations of HOTIs in various systems.

3.1.3. Photonic crystal HOTIs

In photonics, light trapping to the limit of the size by using photonic crystals or plasmonics is a fascinating topic and highly pursued for enhanced light matter interactions and development of photonic integrated circuits, and thus naturally drives topological photonics to smaller scale [77, 78]. In this sense, a photonic crystal HOTI slab having corner states with ultrasmall mode volume is desirable. In this study, in order to implement the 2D SSH model (without quadrupole moments) in the photonic crystal structure, the square-shaped air hole in the slab was considered as a lattice atom, and the coupling strengths were adjusted like the form of the SSH model by changing the distance between the holes as shown in Figure 3-5. In this case, the unit cell has 4 atoms. It should be noted that in such a system, tight-binding model is not perfectly applicable for the wave-nature of the photonic crystal.

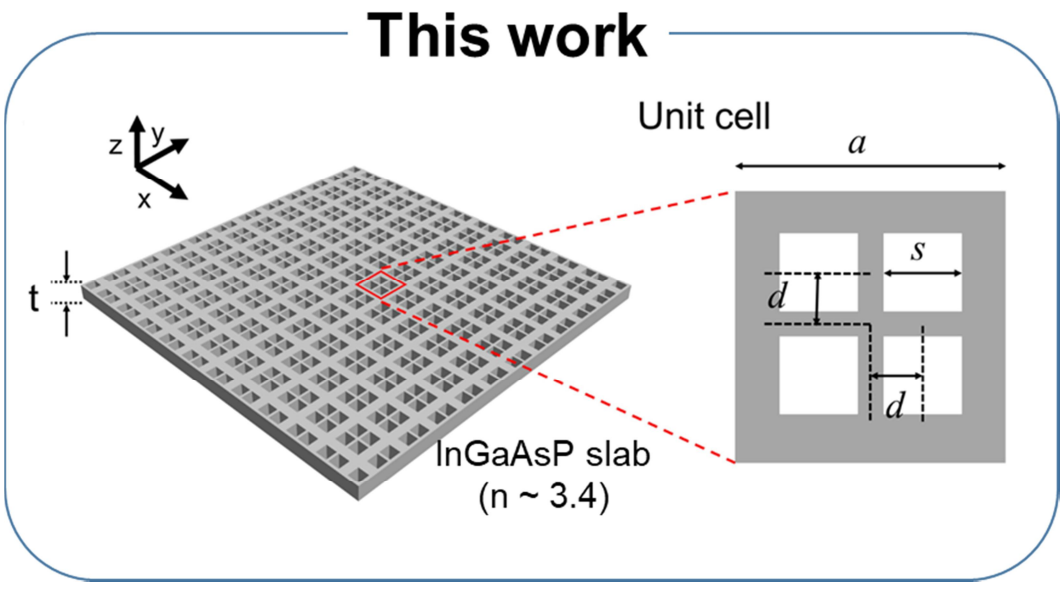

Figure 3- 5. A photonic crystal slab HOTI.

3.2. Result and discussion

3.2.1. Band structure calculation

First, we tried to calculate the bulk band structure considering the unit cell. Inverting the relative strengths of the inter-cell and intra-cell coupling strengths, which is the topological phase transition condition of the SSH model, is achieved by adjusting the positions of the holes (changing *d* in inset of Figure 3-6 [79]) in the unit cell. The FDTD simulated structure is that square-shaped holes are drilled into the slab and the unit cell of the lattice constant a = 500 nm consists of 4 holes with the side length of r = 0.33a. In such a case, considering the TE mode is qualitatively the same as the TM mode of the dot-in-air structure studied by other group previously. In our study, we only consider an isotropic case, which means that the all 4 holes are apart from the center of the unit cell by the same distances, and the distances in the x and y directions are the same. As shown in Figure 3-6, there is no band gap when the hole position is in a neutral position (middle panel), but the band-gap opens when shrinking (left panel) or expanding (right panel) the unit cell. At this time, in common with the SSH model, the band-gap is topologically trivial for the shrunken unit cell and topologically nontrivial for the extended unit cell. At d = 0.25a, the unit cell is the supercell of the unit cell with a single hole, resulting in the gapless, folded band structure. At d ≠ 0.25a, the band-gap (partial or full) opens and different topological phases emerge depending on whether the unit cell is extended or shrunken. It is known that a topological invariant of this structure can be defined with 2D Zak phases (polarizations), unlike Chern numbers of the conventional 2D topological insulators. This vectored Zak phases can distinguish different topological phases as (0,0) for trivial, (1/2,1/2) for nontrivial [80].

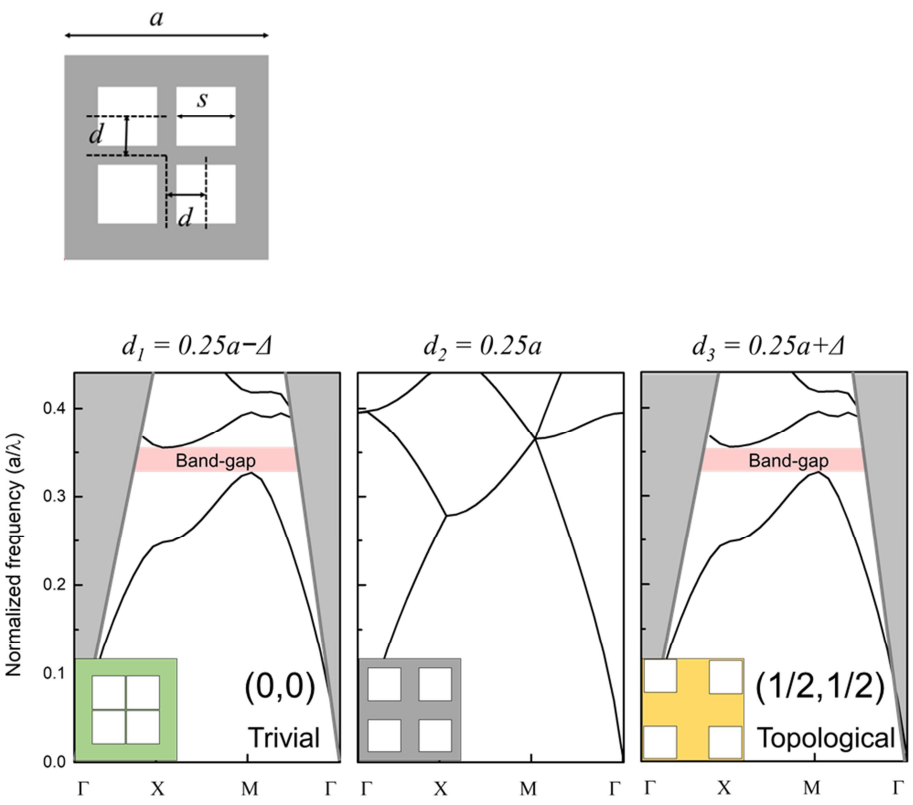

Figure 3- 6. FDTD calculated band structures of different unit cell parameter. A topological phase transition is observed. Topological invariants are shown as numbers.

3.2.2. Hierarchical topology

As mentioned above, topological invariant of bulk is 2D Zak phases (polarizaions), $\boldsymbol{P}=(P_x,P_y)$, which is defined as [81],

$$P_j = -\frac{1}{(2\pi)^2}\int d^2\boldsymbol{k}\mathrm{Tr}[i\left\langle u_m(\boldsymbol{k})\left|\partial_{k_j}\right|u_n(\boldsymbol{k})\right\rangle] \qquad j=x,y, \tag{24}$$

In our band structure, there is only a single band below the band gap of interest (m,n=1). And we can substitute the integration with summation considering a discrete set of k-points.

$$P_x = -\frac{i}{(2\pi)^2}\Sigma_{BZ}\langle u(k_x,k_y)|\partial_{k_x}u(k_x,k_y)\rangle dk_x dk_y \tag{25}$$

By using following approximations,

$$\begin{gathered} u(k_x+dk_x,k_y)\approx u(k_x,k_y)+\partial_{k_x}u(k_x,k_y)dk_x \\ \langle u(k_x,k_y)|u(k_x+dk_x,k_y)\rangle \approx \\ 1+\langle u(k_x,k_y)|\partial_{k_x}u(k_x,k_y)\rangle dk_x \\ \ln(\langle u(k_x,k_y)|u(k_x+dk_x,k_y)\rangle) = \\ \ln(1+\langle u(k_x,k_y)|\partial_{k_x}u(k_x,k_y)\rangle dk_x)\approx \\ \langle u(k_x,k_y)|\partial_{k_x}u(k_x,k_y)\rangle dk_x \end{gathered} \tag{26}$$

We can get,

$$P_x = -\frac{i}{(2\pi)^2}\Sigma_{BZ}\langle u(k_x,k_y)|\partial_{k_x}u(k_x,k_y)\rangle dk_x dk_y$$

$$= -\frac{i}{(2\pi)^2}\Sigma_{BZ}\ln\left(\langle u(k_x,k_y)|u(k_x+dk_x,k_y)\rangle\right)dk_y \qquad (27)$$

$$= -\frac{i}{(2\pi)^2}\Sigma_{k_y}dk_y \ln\Pi_{k_x}\langle u(k_x,k_y)|u(k_x+dk_x,k_y)\rangle$$

To calculate this numerically, first we should obtain EM mode profiles (Hz) at each k point → $u(k_x,k_y)$ by using FDTD simulations as shown Figure 3-7. Then, For each k_y, we compute $\ln\Pi_{k_x}\langle u(k_x,k_y)|u(k_x+dk_x,k_y)\rangle$. Summing over all the values about k_y's completes the calculation.

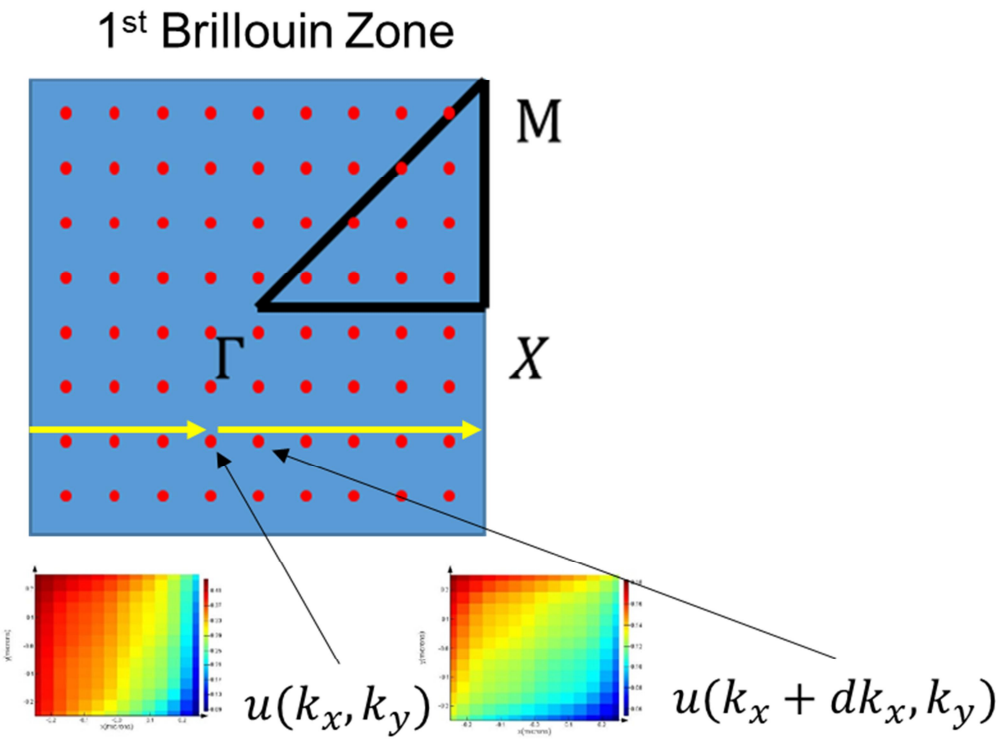

Figure 3- 7. Discretization of Brillouin zone for computing wavefucntions.

If 1D edge states exist, topological invariants of the edge states can also be calculated. Topological invariant of the edge is defined as,

$$p_i = -\frac{1}{(2\pi)^2}\int dk\mathrm{Tr}[i\langle v_m(k)|\partial_k|v_n(k)\rangle] \quad (i=x,y,) \qquad (28)$$

The calculation is the same as the bulk case, except that summation is 1D. Figure 3-8 shows the calculation result. The polarization is constant and independent of the structural parameter, except the phase transition point, and 0 for trivial 0.5 for nontrivial.

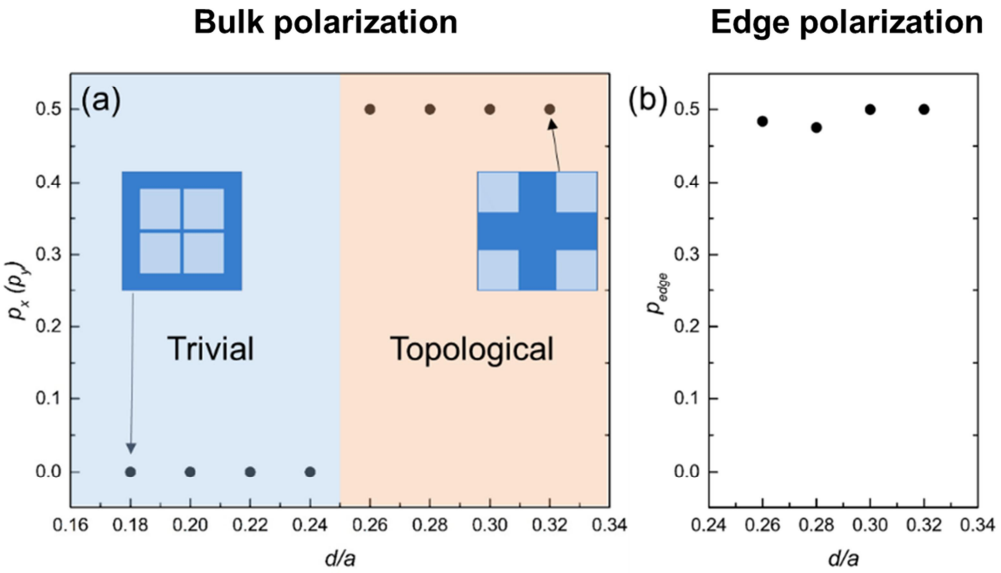

Figure 3- 8. Calculation results of polarization for different parameters.

3.2.3. Edge state simulations

To investigate edge states by numerical simulations, we tried to calculate the projected band structure by bringing the trivial and nontrivial structure into contact and giving periodic boundary conditions in the direction parallel to the boundary as shown in Figure 3-9. As a result, it was confirmed that an isolated waveguide mode existed between the upper and lower bulk bands. To verify that this mode is the edge state, we calculated the mode profile at an arbitrary point (marked by star) on the band. As a result, it was confirmed that the mode distribution existed at the boundary of the topologically different structures. Subsequently, as a finite structure in all directions, we simulated a structure in which the topologically nontrivial structure surrounds the topologically trivial structure. As a result, a resonance mode (indicated by the red dashed line) was observed at the frequency gap between the edge mode and bulk mode, and the distribution of the mode was calculated to confirm that it existed at the corner of the structure. As a summary, the 1-D gapped edge state appears when two topologically different structures are interfaced, and Corner-localized state is generated as two nontrivial edge polarizations converge at the corner.

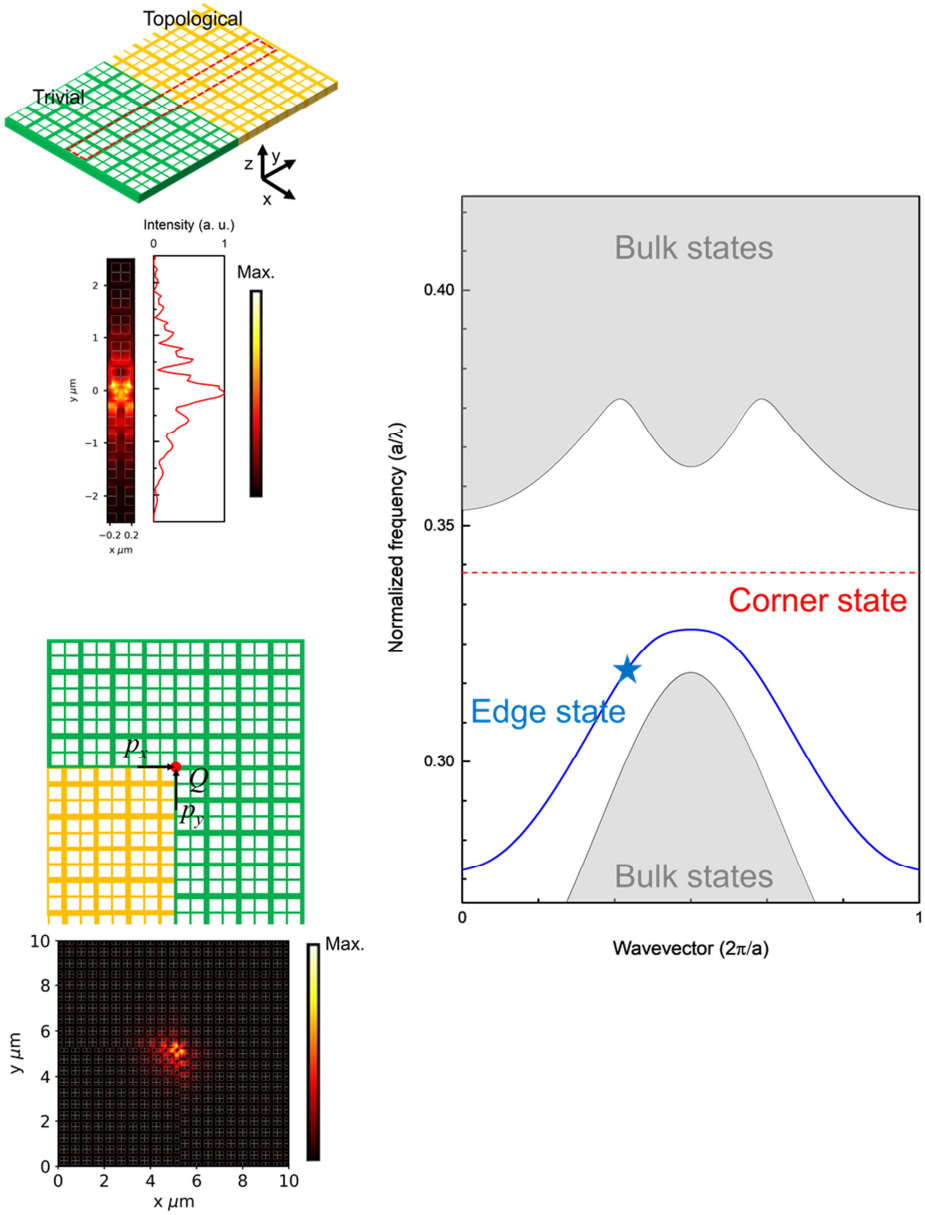

Figure 3- 9. Simulation results of the edge state and corner state.

3.2.4. Device fabrication

We fabricated the sample based on the simulation results. Brief fabrication steps are described in Figure 3-10. The pattern was produced by E-Beam lithography and dry etching of the MQW slab. For the vertical mode confinement, the air-bridge structure was formed by wet etching of the sacrificial layer. The sacrificial InP layer was removed by dipping the sample in the HCl solution. It should be noted that since it is difficult to manufacture the structure in which the holes are located at the position resulting in very small gaps between them, it is manufactured as a parameter that the holes come into contact with.

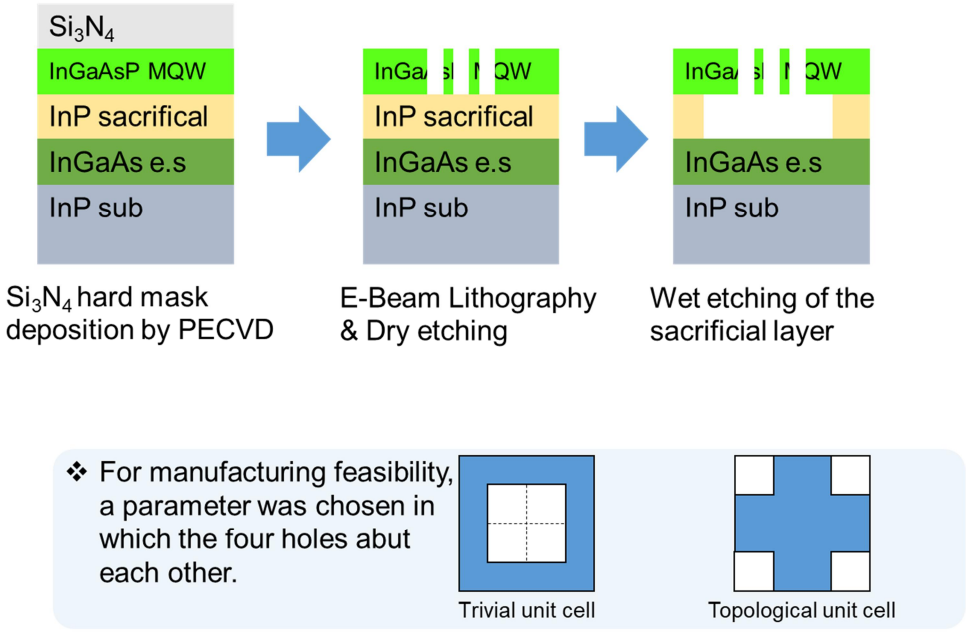

Figure 3- 10. A schematic of fabrication steps.

3.2.5. Photoluminescence measurement

The SEM image of the fabricated device is shown in Figure 3-11. The fabricated sample was subjected to optical pumping and PL was measured. The pumping spot was positioned at 4 corners, 4 edges, and 1 bulk, respectively. As a result of the measurement shown in Figure 3-12, each photonic topological mode gains the optical gain and exhibits laser oscillation. The wavelengths of the laser mode were increased in the order of corner-edge-bulk, which is identified from upper panels of Figure 3-12. This is consistent with the simulation result of the projected band structure in previous section. In each pumping situation, the CCD image was checked when the laser oscillated, which is shown in bottom panels. When pumping to the corner, the laser modes are localized at the corners, and when pumping to the edge, the laser modes spread along the interface of the two region. When the bulk region was pumped, it was possible to check the wide spread laser mode. And when simulating the same structure, the mode spectra and the mode profiles are similar to the experimental results. However, in the case of the ideal structure, due to the structural symmetry, four corner and edge states are degenerate. Actually, it is not perfectly symmetrical due to fabrication imperfection, therefore after applying some structural deviations in the simulation, the results become closer to the experimental results. Through this, it was confirmed that laser oscillation could be realized in the corner-edge-bulk hierarchical modes.

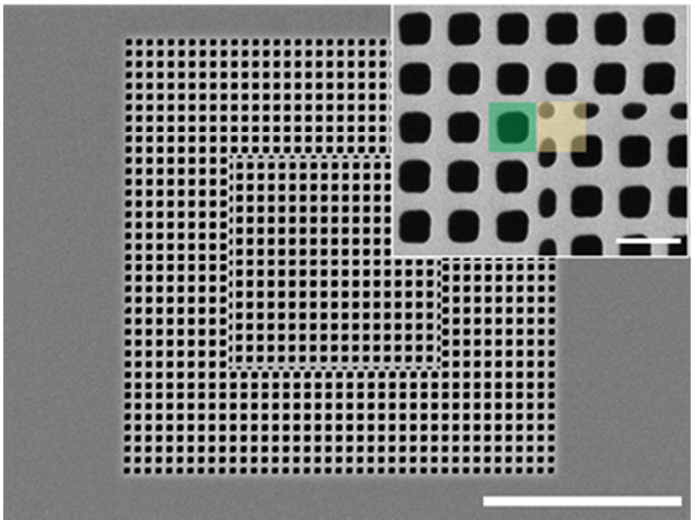

Figure 3- 11. A SEM of the fabricated device. Inset shows a magnified view of the corner area.

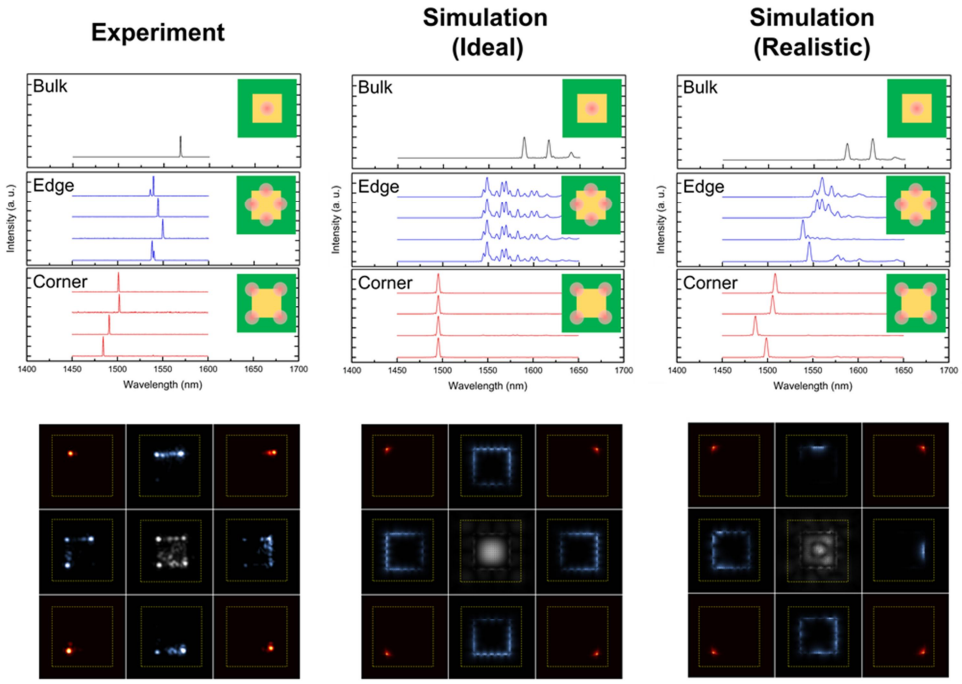

Figure 3- 12. Upper panel; Measured PL spectra and simulated spectra of the structure. Lower panel; CCD images of the lasing modes and simulated mode profiles of representative modes.

3.2.6. Lasing characteristics

We checked the input / output characteristics for all lasing modes with optical pumping. As shown in Figure 3-13, All modes showed threshold behavior which is evidence of lasing. The threshold values are similar for all modes (7~8 kW/cm^2), but considering the deviation of the slope efficiency and the calculated Q-factor, we can see that the corner states are more robust than the edge state. This is thought to be due to the fact that the edge states have a lot of scattering in the process of forming the Fabry-perot modes because there is no protection (such as back-scattering immune) for the propagation of the mode.

We focused on the corner state lasing characteristics for more detail. Figure 3-14 shows that a concomitant behavior of linewidth narrowing near the threshold also indicates transition to lasing. Figure 3-14 also shows a logarithmic plot of measured L-L data and a fitted curve obtained from the laser rate equations [53]. Spectral evolution for laser with threshold is presented. It is also presented that the far-field polarization result which exhibits a linear polarization forming an angle of 45 degrees with x-y direction. It might be attributed to the fact that the far-field polarization direction of the corner state is a vector sum of two orthogonal far-field polarization of edge modes.

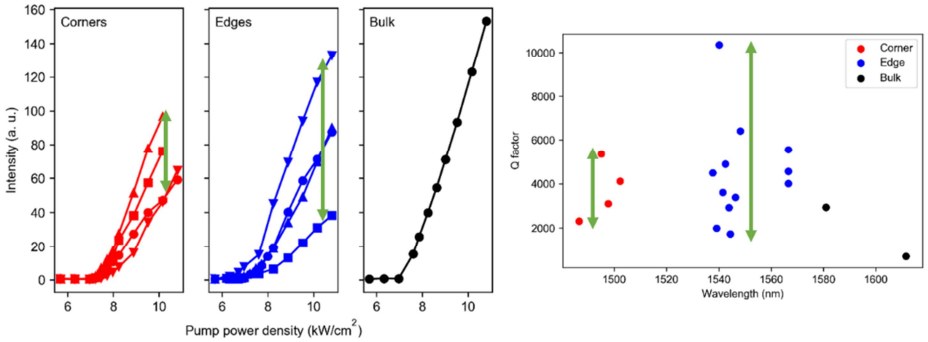

Figure 3- 13. Output intensities of each lasing mode as function of the input pump power (left). Calculated quality factor distribution of the resonant modes.

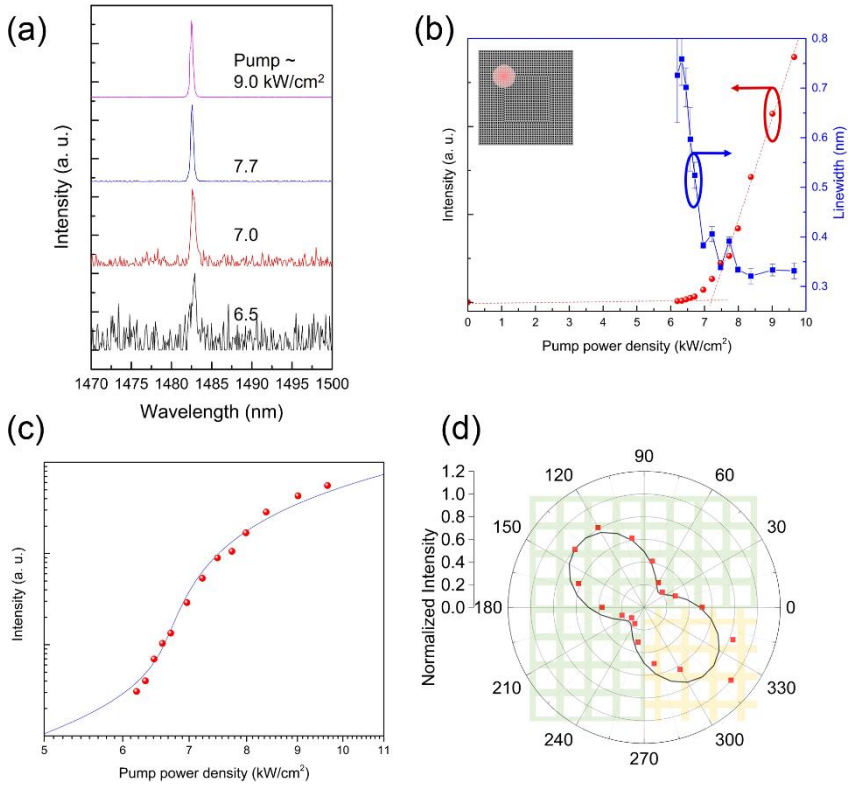

Figure 3- 14. Performance characteristics of the corner state lasers. (b) Light output intensity (red dots) and laser linewidth (blue dots) as a function of excitation power density, measured for the one of the corner states in a device. Error bars represent Lorentzian fitting errors. (c) Logarithmic scale plot of the measured output intensity (red dots) and the theoretical curve from the rate equations (blue). (a) PL emission spectra with increasing pump intensity from below to above threshold. (d) Far-field polarization dependences of the corner state laser. The red dots are measured data, while the black lines are from FDTD simulations.

3.2.7. Origin of in-gap corner states

In the case of the 2D SSH structure as shown in Figure 3-1, it is known that the corner state exists inside the bulk band and it can hybridizes with the bulk mode [69, 82]. We first directly verified this by using the tight-binding calculation. For the calculations, the open source Python library code (*PythTB)* was used. For the calculation parameters, a 6 × 6 finite array of unit cells was considered. The coupling strengths (h) between photonic atoms was defined by a single exponentially decaying function of the distance, h=exp(-s) where s was the interatomic distance. The longer and shorter distances between the sites in the x and y direction were arbitrarily selected to be 3.5 and 1.5, respectively, while all on-site energies were set to zero. Figure 3-15 shows a schematic of the lattice and a density of state spectrum of the calculated eigenvalue distribution. Since the lattice has a chiral symmetry (see Figure 3-17), the spectrum appears to be symmetric with respect to the zero energy. We plot the spatial eigenfunction distribution at the zero energy, which is expected to be the energy of the corner states. As a result, the mode distribution shows that the corner and bulk state are hybridized. However, for wave-based systems such as photonic crystals which is studied in this work, long range interaction cannot be ignored. To identify the effect of the complex interactions, we add the coupling constants in every diagonal direction and next-nearest neighbors, as schematically shown in Figure 3-16. When this long range interaction is put into the calculation, we can see from Figure 3-16 that the spectrum becomes asymmetric due to the breaking of the chiral symmetry of the lattice as shown in Figure 3-17, and the corner state can be positioned the band-gap, making it possible to observe the localized mode.

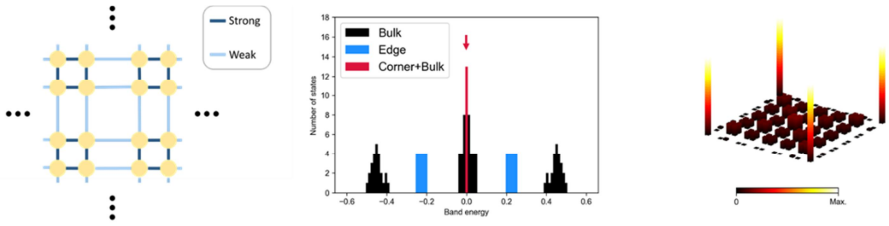

Figure 3- 15. A tight-binding calculations result of the 2D SSH structure.

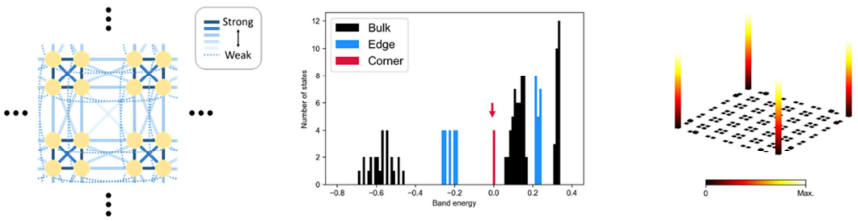

Figure 3- 16. A calculation result of the 2D SSH structure with complex coupling interactions with sites.

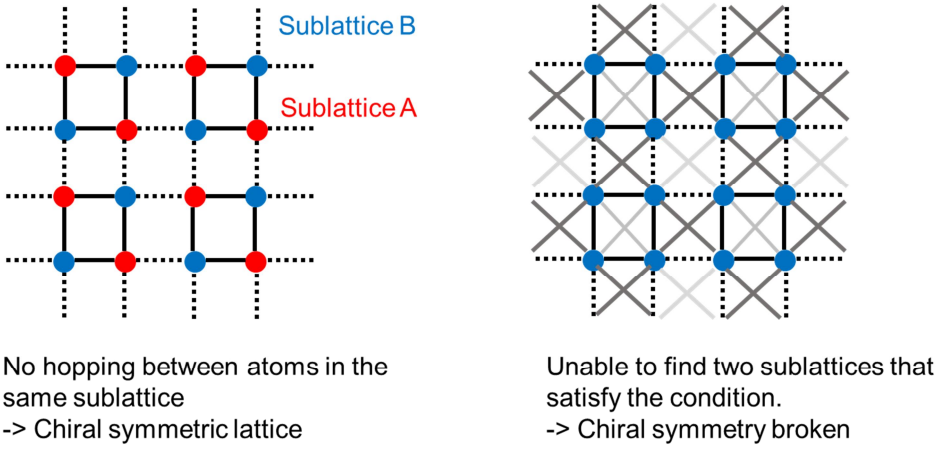

Figure 3- 17. Chiral symmetry of the 2D SSH lattices.

3.3. Conclusions

In summary, we designed and demonstrated lasing action in 2D photonic crystals with hierarchical topological states by using a semiconductor gain material operating in the optical frequency regime. Each topological states were confirmed by the lasing spectra and direct visualization of the lasing modes. Our demonstration will have an important effect on realizing photonic integrated circuits with topological photonic crystals, specially enabling multiple components such as resonators, waveguides, couplers to be integrated in a single photonic crystal device. Moreover, our work will potentially provide various fundamental study platforms about higher order topological states, if combined with nonlinearity, non-Hermitian physics or quantum photonics.

Chapter 4. Preliminary results of a valley edge mode laser.

4.1. Introduction to valley photonic crystals

Since the birth of the first quantum Hall insulator, topological insulators with various operation principles have been proposed. Topological invariants defined for various types of topological insulators can be distnaguished, and topologically protected properties also can be different. Therefore, in the viewpoint of adopting the principles to photonics, various topological structures can be candidates for nanophotonic devices. Among various topological insulators, in solid state systems, a valley degree of freedom which is manifested in TMDCs (2D materials) is recently attracting great interest for a novel degree of freedom applicable for future information processing. Valleys are extrema of the energy band, and atomic transition properties of different valleys related to each other by certain symmetry (e.g. *K* and *K'* with inversion symmetry in honeycomb lattices) should be the same if the lattice maintains that symmetry. However, for TMDCs, the inversion symmetry is broken and thus *K* and *K'* valleys show different atomic transitions depending on the chirality of absorbed light (which is otherwise the same), as it is getting to become atomically thin [83-86]. Inspired by this property, the valley photonic topological insulator becomes one of the principles applicable to on-chip systems and easy to be implemented at the nano-photonic level. Briefly, as shown in Figure 4-1, when inversion symmetry is broken in the unit cell, different topological invariants (valley Chern number) may appear at the valleys of the energy band depending on the parity of symmetry breaking. It should be mentioned that the (total) Chern number is always zero due to time reversal symmetry. However, when two different structure with different valley topology are brought into contact, valley edge modes must exist near the valleys due to the difference in valley Chern numbers, and the directionality of the edge modes (momentum at the valley) is preserved as long as the inter-valley scattering is not prominent. This edge state by itself can be used as a waveguide

with low loss [87-93], and can be utilized as a ring resonator when configured in the form shown in right panel in Figure 4-1 [94]. Small-sized and exotic-shaped ring resonator devices should be possible using the valley edge modes.

First, as a unit device, we aim to manufacture a laser device using such a ring resonator. Although there is a large angle of bend in the optical path, provided topological protection, it is expected that there will be laser modes based on the whispering-gallery principle (WGM). Also, the topological edge mode can be confirmed by comparison with a trivial ring resonator. In the future, it is planned to check whether it can have better performance than a trivial structure, and to verify the robustness of the device in various ways. Then, by combining these laser modes with the topological waveguide, we intend to lay the foundation for an optical integrated circuit capable of propagating optical signals without loss.

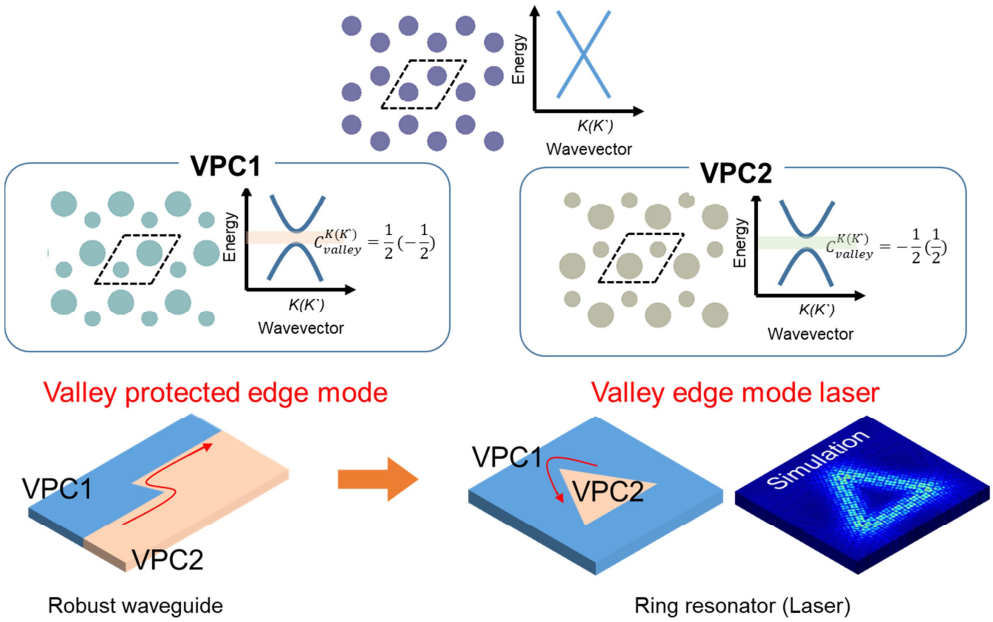

Figure 4- 1. Schematics of the band structure of the valley photonic crystals and possible applications.

4.2. Result and discussion

4.2.1. Band structure of valley photonic crystals

We calculated the band structures of the honeycomb lattice photonic crystals with and without inversion symmetry, using the FDTD method. The period and thickness of the slab is fixed as 485 nm and 200 nm respectively. The unit cell of the honeycomb lattice has two atoms as shown in Figure 4-1. For the case of the photonic crystal with inversion symmetry which is shown in left of Figure 4-2, radii of two holes are designed to be the same (0.21*period) and resultantly, a typical honeycomb band structure which exhibits Dirac points at K(K') points is produced. When inversion symmetry is broken by differentiating the radii of two holes in the unit cell (0.245*period and 0.185*period), a band-gap opens as shown in right panel of Figure 4-2.

The calculated projected bandstructures of the structure with and without an interface between two VPCs are shown in Figure 4-3. In the case of the structure with the interface, we observe the band that does not appear in the structure without the interface, and the band has opposite group velocities at the different K(K') points. This implies that provided valley protection (in other words, lack of inter-valley scattering), the propagation of photons near K(K') point can be robust against certain disorder.

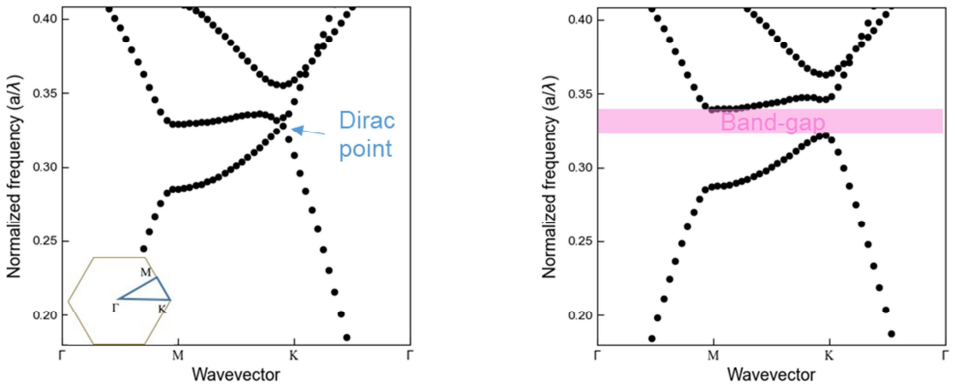

Figure 4- 2. Calculated band structures of the honeycomb lattice photonic crystals with (left) and without (right) inversion symmetry.

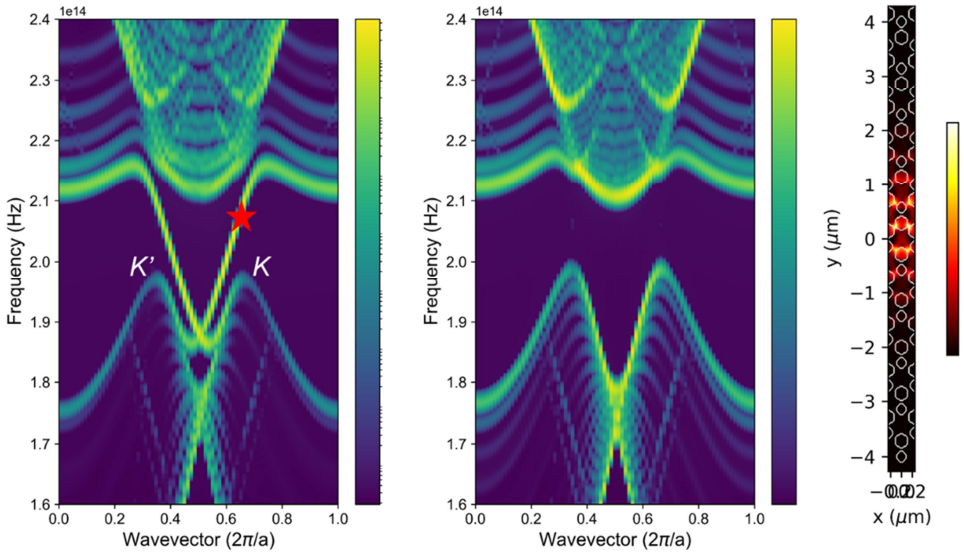

Figure 4- 3. Calculated projected band structure of the structures with the interface where two VPCs are brought into contact and without the interface. Simulated mode profile at the point denoted by a star.

4.2.2. VPC laser

We used aforementioned broken inversion symmetry honeycomb lattice for actual device fabrication, the structure used in previous VPC studies [92] as well. It is shown that if the inversion symmetry is maintained, the band structures shows Dirac points at the $K(K')$ and no band-gap. However, if the symmetry is broken, the band-gap opens at the $K(K')$ points and topological invariants of the band-gap near the valleys (valley Chern numbers) can be calculated. We designed and fabricated a ring resonator formed by placing two different VPC in a way that the inner VPC is surrounded by the outer VPC which is topologically different from the inner VPC. Figure 4-4 shows the SEM images of the fabricated sample. The same optical gain medium, InGaAsP multiple quantum well slab with thickness ~200 nm, was used for fabrication and the standard e-beam lithography was utilized. Structural parameters can be measured from the SEM image. At the interface, the valley edge modes exist and it can form triangular-shaped WGM mode, which can lase if sufficient gain is provided.

Therefore, we conducted PL measurements and measured spectra and emission images from a CCD camera. As shown in Figure 4-5, sharp lasing peaks were observed when pumped above lasing threshold. A measured L-L data clearly shows a transition from spontaneous emission to simulated emission. The CCD image in inset also indicates that the lasing indeed occurs at the triangular-shaped boundary between two VPCs. We also calculated cavity modes by using the FDTD methods. In the spectral band-gap region which is produced by inversion symmetry breaking, several modes were observed and it was confirmed that the modes were triangular-shaped, which means that they are valley-protected edge modes.

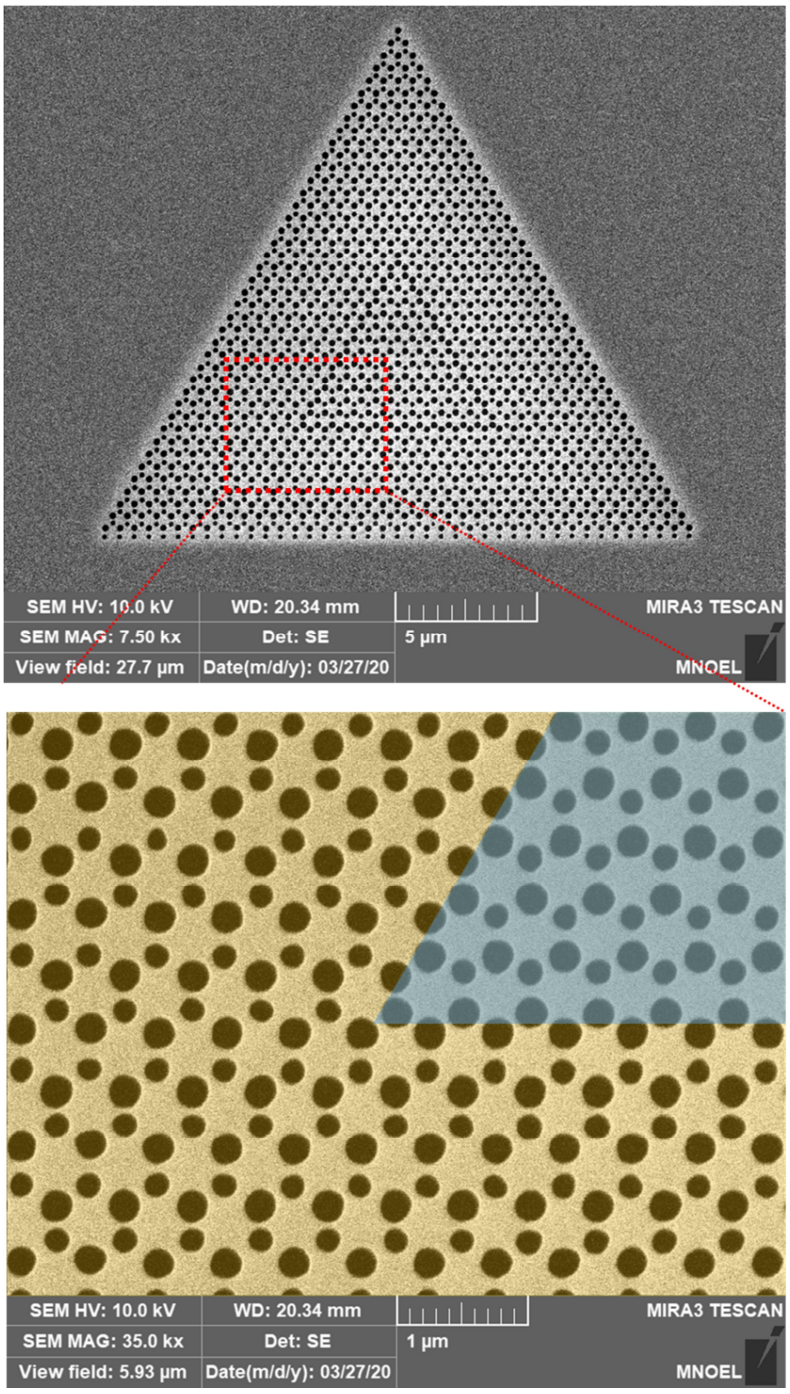

Figure 4- 4. A SEM image of the fabricated VPC laser.

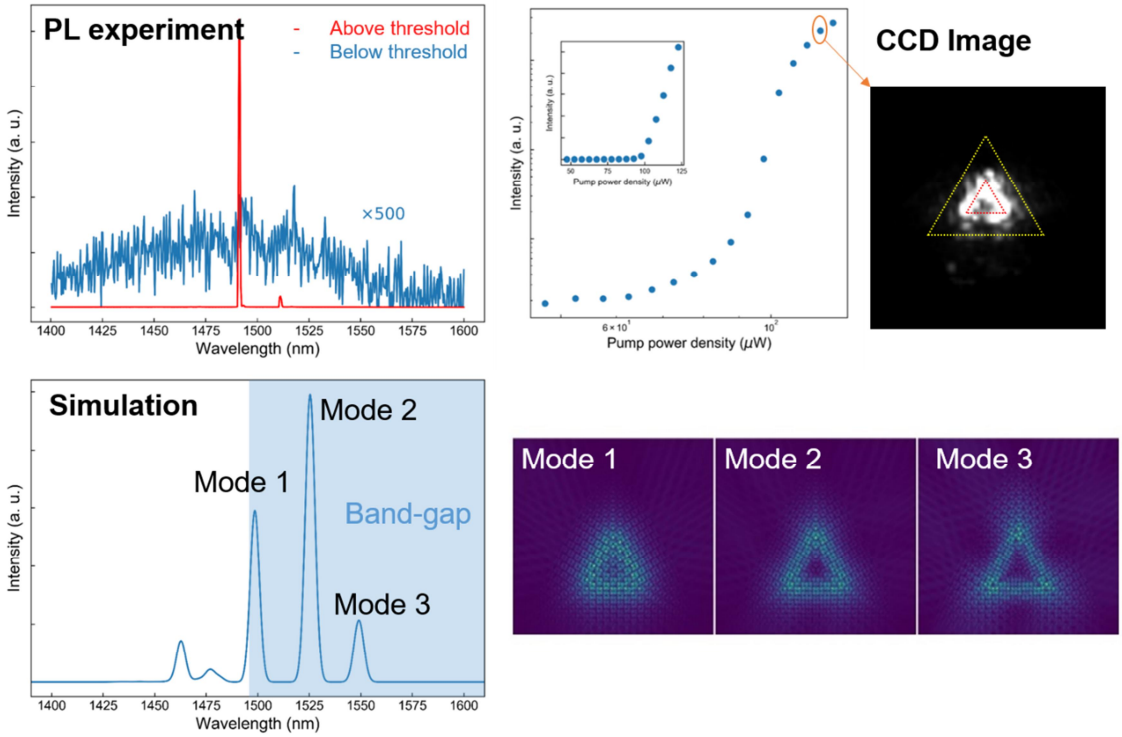

Figure 4- 5. Lasing characteristics and FDTD simulation results of the VPC laser.

4.2.3. Comparison with a trivial cavity laser

We conducted another experiment to verify the lasing modes were indeed originated from the valley edge modes. We fabricated another triangular-shaped ring cavity, but in this time composed of trivial photonic crystal waveguides. We optically pumped the VPC laser and the trivial laser at several different pump positions near the interface as shown in Figure 4-6, to introduce spatially non-uniform gain distribution. The PL measurement results are shown in Figure 4-7. For the VPC laser, the same lasing modes were excited regardless of the pump position. Measured CCD images also indicates that the shapes of the lasing modes are the same for all cases. This means that the lasing modes are indeed triangular shaped and the mode distributions are everywhere along the interface, which results from the circulation of the valley edge mode. This clear message that the modes can propagate without backscattering at the waveguide bends to achieve round trips, thus implies that the modes at the interface are indeed the valley-protected topological edge modes. On the other hands, for the trivial cavity, different lasing modes appear when pump position is changed. The lasing CCD image also shows different shapes depending on the pump position (It seems like that only waveguide modes near the pump position are excited). This means that the resonant modes are not circulating modes and the mode distributions are only at the part of the triangular-shaped wave guides. Notice that bright spots at the positions of the waveguide bends are observed from the CCD images. This implies that the modes experience large scattering from the waveguide bends, which is stark difference from the VPC lasers with topological protection.

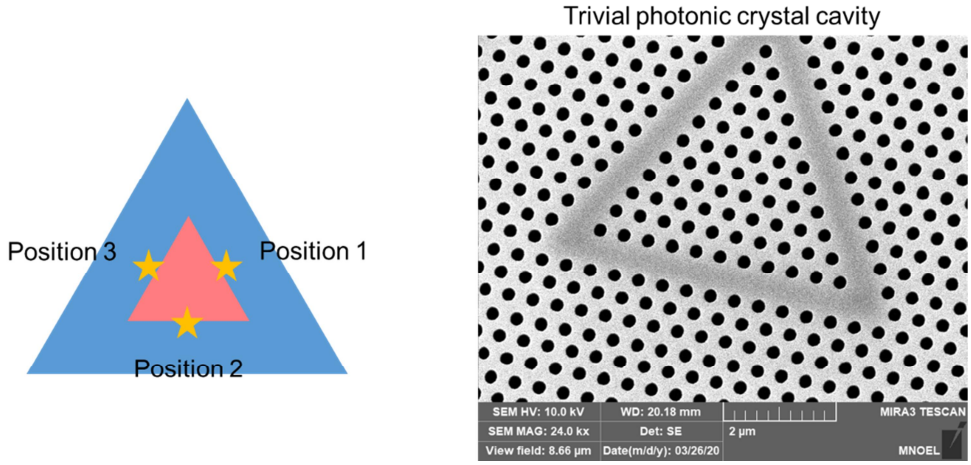

Figure 4- 6. A scheme for pump position dependence and a SEM image of the trivial cavity.

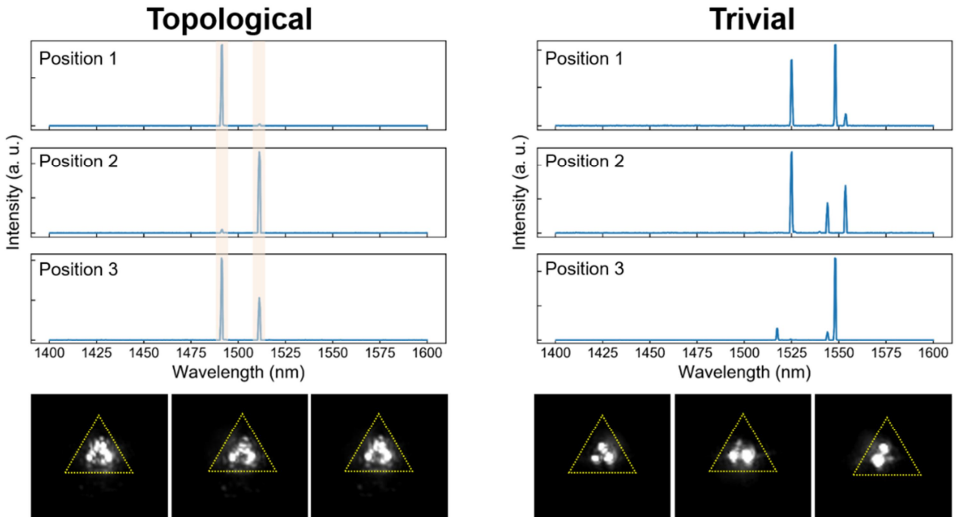

Figure 4- 7. PL spectra and CCD images for the VPC and trivial lasers.

4.2.4. FSR analysis

Interestingly, we observed a splitting of WGM modes on several devices. Figure 4-8 shows an example of the VPC laser device exhibiting the splitting of each azimuthal order mode. It is noticed that both lasing and non-lasing WGM modes appear in pair. The splitting of the WGM modes can be attributed to the well-known phenomenon which happens when there is a scattering of traveling modes associated with local defects, resulting in coupling of counter-propagating (CW and CCW) WGM modes otherwise degenerate. We could claim from this observation that topological protection, despite sharp bents, allowed the valley edge modes to form the WGM modes, but could not provide complete protection from scattering.

We investigated the dependence of the size of the triangle cavity size. We compared lasing spectra of the device with the side length of 20*a* and 14*a*. The larger sized devices are rarely excited, which could be attributed to inefficient pumping geometry and probability of bulk lasing modes. Measured lasing spectra are shown in Figure 4-9. The device with the larger size exhibit smaller free spectral range (FSR) of the averaged value of ~2.17 THz, and smaller device shows larger averaged-FSR of ~3.02 THz. This is natural result of simple relation between FSR and the cavity length. The ratio of two FSR (~0.718) is comparable to that of the cavity length (0.7), which reflects that a group index is nearly constant (linear dispersion of edge modes) in the operation frequency range.

The group indices of the valley edge modes are estimated from measured FSRs of the two devices mentioned above and it is compared with the simulated result. The result is summarized in Fig. 4-10. Assuming a constant group velocity at the frequency range of interest, both devices exhibit similar group velocities of ~4.7. We then obtained simulated group indices by differentiating the valley edge mode dispersion, based on the relation, $v_g = c/n_g = d\omega/dk$. Observe that near the K wavevector point, measured group indices (dashed lines) agree well with the simulated group indices (red dots). This further supports our argument that the lasing modes are indeed originated from the valley edge mode of topological photonic crystals.

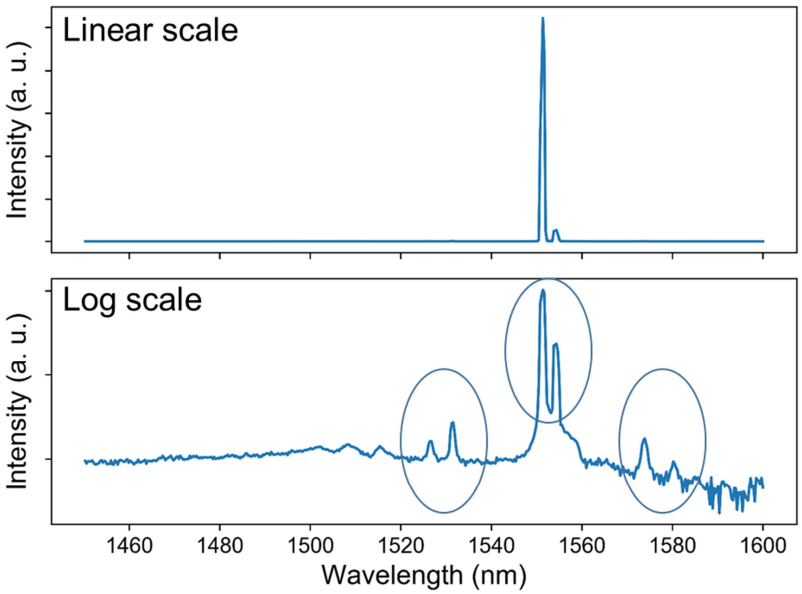

Figure 4- 8. PL spectra of the lasing device plotted in linear and log scale. Circles indicate pairs of split modes.

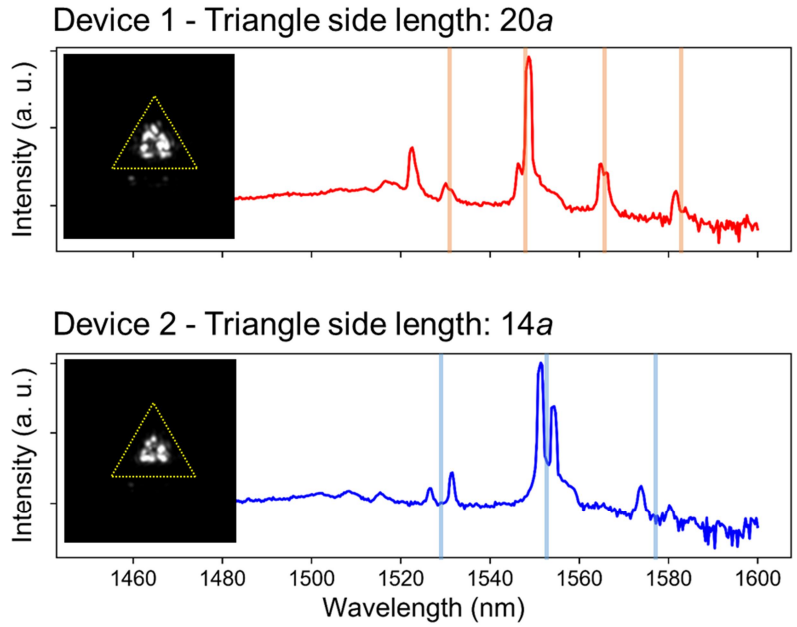

Figure 4- 9. Lasing PL spectra for VPC cavities with different sizes.

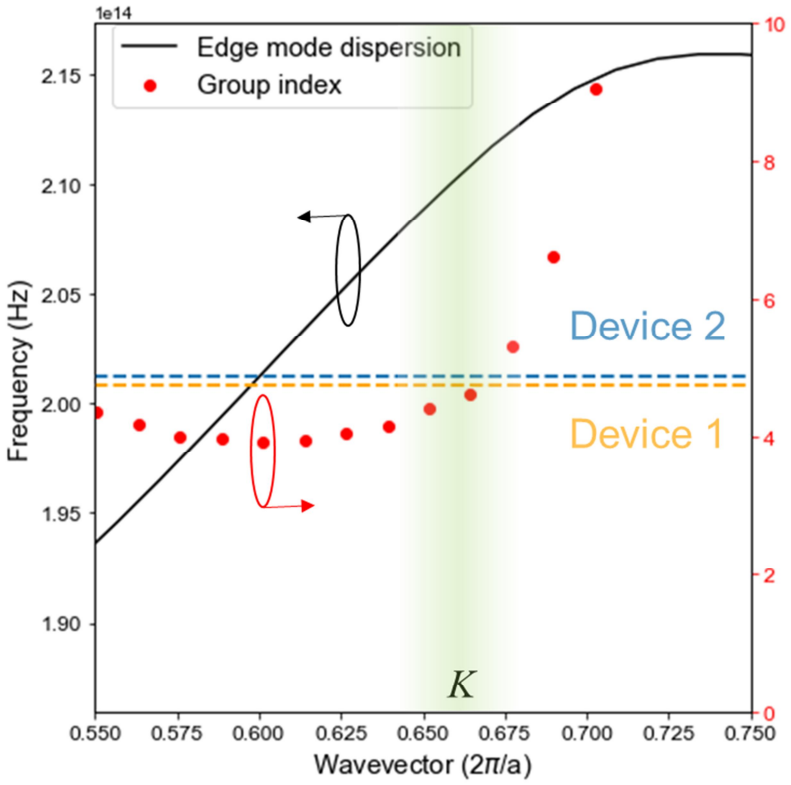

Figure 4- 10. Measured group indices of the two devices (dashed lines) and the simulated edge band dispersion (line) from which the simulated group indices (red dots) are deduced.

4.2.5. Structural disorder simulation

We investigated the effect of structural disorder on valley edge WGM modes. We divided the types of variation into two kinds; variation in the position of holes and variation in the size of holes. Fig. 4-11 shows a schematic description of the implementation of position variations. Each hole is shifted from the ideal position by $\Delta x_i = a\gamma_{i,x}\eta_{i,x}, \Delta y_i = a\gamma_{i,y}\eta_{i,y}$, where γ_i characterizes the strength of disorder and η_i means uniform random number in range (-1,1). Fig.4-11 also contains simulated spectra showing that as mentioned in the previous section, each azimuthal WGM mode split into pair of the modes as disorder increases. From the simulation results of modes profiles of the split modes, we observe that the mode profiles are slightly distorted, despite that triangular resonant modes are still available. Also we can find that the amount of splitting varies by different disorder configurations. For the simulation for hole size variations shown in Fig. 4-12, we varied each hole size as $\Delta r_i = r_i\xi_{i,x}\eta_i$, where ξ_i again serves as disorder parameter. Interestingly it does not seem to have a clear signature of mode splitting until disorder significantly weakens the quality of modes, diminishing edge modes to be comparable to weak bulk modes. We conclude that positional disorder has a greater effect on the edge mode.

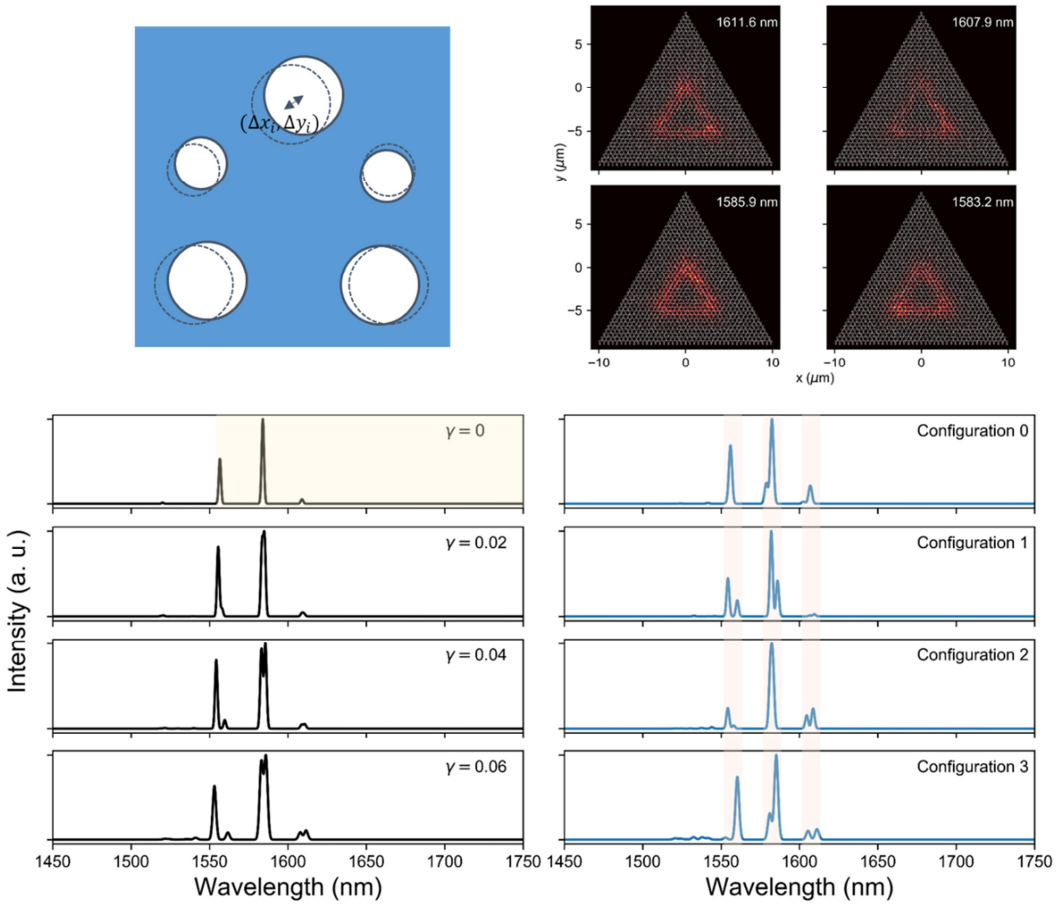

Figure 4- 11. Simulation results about structural disorder in the position of holes.

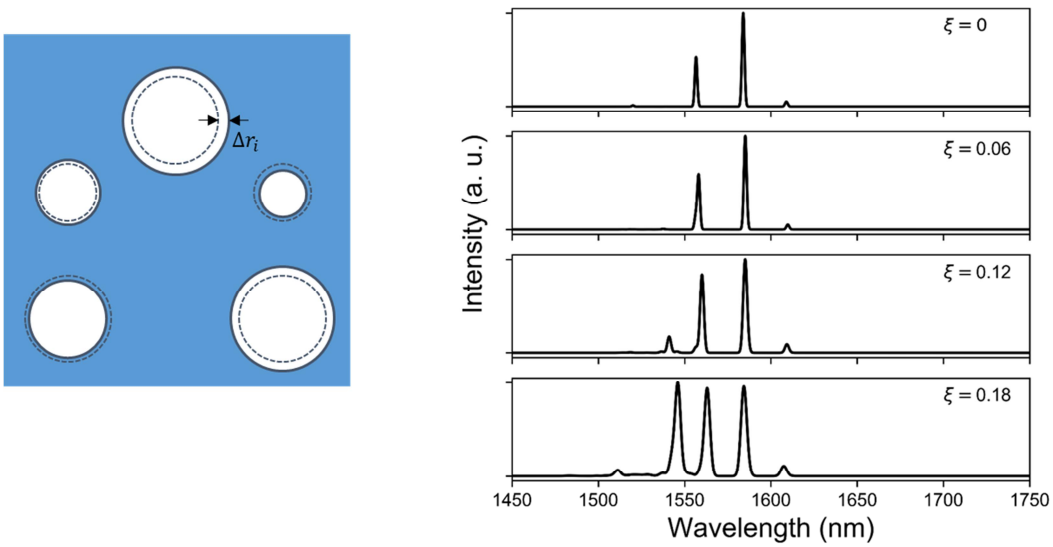

Figure 4- 12. Simulation results about structural disorder in the size of holes.

4.3. Conclusions

We designed the VPC and confirmed the lasing action from the valley edge modes through optical pumping. Previously, robust propagation using valley edge modes has been demonstrated in passive platforms, but laser oscillation by forming a ring resonator with the valley edge modes has never been realized. We realized the VPC laser using a InGaAsP gain material for the first time and measured laser characteristics. To confirm that the laser modes are actually the valley edge modes, comparative experiments were performed with a trivial cavity laser. The valley edge modes were able to round-trip along the triangular-shaped interface thanks to topological protection, which was verified through spectrum and CCD image analysis. In the future, it is expected that additional studies will discover useful properties of the VPC laser, and that combination with other photonic components will also be realized.

Chapter 5. Conclusion and Perspective

In this thesis, we studied the topological photonic structures inspired by the topological insulators in condensed matter physics, and especially realized the laser oscillation appearing in the topological edge state by utilizing the optical gain material, and investigated its properties.

First, the edge state appearing in the photonic crystal L3 cavity array was theoretically confirmed by computational simulations, and experimentally confirmed by laser oscillation. As a result of applying the SSH model to the array and constructing finite lattices with topologically different unit cells, it was confirmed that the topological edge state appears only in the topologically nontrivial array. Modal distributions of the lasing modes were directly observed by SNOM measurement, clearly identifying the origin of the lasing modes. In addition, it was confirmed that the topological edge state was less sensitive to process errors than the bulk state.

Second, we studied the higher-order edge state in a 2D SSH like photonic crystal. Unlike ordinary (first order) TIs, the higher-order topological insulators can have edge states whose spatial dimension is more than 2 dimension lower than the dimension of the bulk. For the 2D photonic crystal, it was confirmed through simulations that not only the 1D edge state but also the 0D corner state existed, and the laser oscillation in the bulk-edge-corner state was also confirmed. It is confirmed that they have distinct properties from spectral and spatial measurements.

Finally, robust lasing from valley edge modes was also demonstrated. Valley edge modes at the interface between two VPCs were topologically protected and experienced less backscattering at the bends of the interface waveguide. This robustness enabled to form WGM modes even in the triangle-shaped cavity.

Topological photonics are being actively researched, and active topological photonics have attracted attention more recently. Topological edge modes will be much more beneficial for

lasers compared to non-topological modes in the sense that it can offer higher-efficiency, modal robustness, single modeness [95], etc. Optical gain medium with topological photonic structures is naturally opening a way to found the area of non-Hermitian topological photonics [44, 96-98], which is already presenting fascinating results. Also active medium related to nonlinearity will be exciting materials for topological photonics, since it enables us to explorer nonlinear topological photonics [99-101]. Furthermore, quantum light sources can also be benefitted by topological edge states, which will strengthen the robustness and efficiency of the quantum information processing in the future [102-104].

References

[1] M. Grabherr, H. Moench, and A. Pruijmboom, "Vcsels for optical mice and sensing," in *Vcsels*(Springer, 2013), pp. 521-538.

[2] J. L. Gimlett, and N. K. Cheung, J. Lightwave Technol. **7**, 888-895 (1989).

[3] C. Han, H. Kim, H. Jung, S.-I. Lee, P. G. Jablonski, and H. Jeon, Optica **4**, 464-467 (2017).

[4] J. D. Joannopoulos, S. G. Johnson, J. N. Winn, and R. D. Meade, *Photonic crystals: Molding the flow of light - second edition* (Princeton University Press, 2011).

[5] L. Rayleigh, The London, Edinburgh, and Dublin Philosophical Magazine and Journal of Science **11**, 196-205 (1881).

[6] E. Yablonovitch, Phys. Rev. Lett. **58**, 2059 (1987).

[7] C. Kittel, P. McEuen, J. Wiley, and Sons, *Introduction to solid state physics* (John Wiley & Sons, 2019).

[8] A. E. Siegman, *Lasers* (University Science Books, 1986).

[9] J. P. Dowling, M. Scalora, M. J. Bloemer, and C. M. Bowden, J. Appl. Phys. **75**, 1896-1899 (1994).

[10] H. Jung, M. Lee, C. Han, Y. Park, K.-S. Cho, and H. Jeon, Opt. Express **25**, 32919-32930 (2017).

[11] H. Matsubara, S. Yoshimoto, H. Saito, Y. Jianglin, Y. Tanaka, and S. Noda, Science **319**, 445-447 (2008).

[12] S. Ahn, H. Kim, H. Jeon, J. R. Oh, Y. R. Do, and H. J. Kim, Applied Physics Express **5**, 042102 (2012).

[13] O. Painter, R. K. Lee, A. Scherer, A. Yariv, J. D. Brien, P. D. Dapkus, and I. Kim, Science **284**, 1819 (1999).

[14] H. Altug, D. Englund, and J. Vučković, Nat. Phys. **2**, 484-488 (2006).

[15] E. M. Purcell, "Spontaneous emission probabilities at radio frequencies," in *Confined electrons and photons*(Springer, 1995), pp. 839-839.

[16] T. Yoshie, A. Scherer, J. Hendrickson, G. Khitrova, H. M. Gibbs, G. Rupper, C. Ell, O.

B. Shchekin, and D. G. Deppe, Nature **432**, 200 (2004).

[17] L. A. Coldren, S. W. Corzine, and M. L. Mashanovitch, *Diode lasers and photonic integrated circuits* (John Wiley & Sons, 2012).

[18] S. Ahn, S. Kim, and H. Jeon, Appl. Phys. Lett. **96**, 131101 (2010).

[19] M. Z. Hasan, and C. L. Kane, Rev. Mod. Phys. **82**, 3045-3067 (2010).

[20] R. B. Laughlin, Phys. Rev. B **23**, 5632 (1981).

[21] D. J. Thouless, M. Kohmoto, M. P. Nightingale, and M. den Nijs, Phys. Rev. Lett. **49**, 405 (1982).

[22] B. A. Bernevig, T. L. Hughes, and S. C. Zhang, Science **314**, 1757-1761 (2006).

[23] M. König, S. Wiedmann, C. Brüne, A. Roth, H. Buhmann, L. W. Molenkamp, X.-L. Qi, and S.-C. Zhang, Science **318**, 766-770 (2007).

[24] S. Raghu, and F. D. M. Haldane, Phys. Rev. A **78** (2008).

[25] F. D. Haldane, and S. Raghu, Phys. Rev. Lett. **100**, 013904 (2008).

[26] Z. Wang, Y. D. Chong, J. D. Joannopoulos, and M. Soljačić, Phys. Rev. Lett. **100**, 013905 (2008).

[27] Z. Wang, Y. Chong, J. D. Joannopoulos, and M. Soljačić, Nature **461**, 772 (2009).

[28] M. Hafezi, E. A. Demler, M. D. Lukin, and J. M. Taylor, Nat. Phys. **7**, 907 (2011).

[29] M. Hafezi, S. Mittal, J. Fan, A. Migdall, and J. M. Taylor, Nat. Photonics **7**, 1001 (2013).

[30] L. H. Wu, and X. Hu, Phys. Rev. Lett. **114**, 223901 (2015).

[31] L. Lu, Z. Wang, D. Ye, L. Ran, L. Fu, J. D. Joannopoulos, and M. Soljačić, Science **349**, 622-624 (2015).

[32] Y. Ota, K. Takata, T. Ozawa, A. Amo, Z. Jia, B. Kante, M. Notomi, Y. Arakawa, and S. Iwamoto, Nanophotonics **9**, 547-567 (2020).

[33] L. Lu, J. D. Joannopoulos, and M. Soljačić, Nat. Photonics **8**, 821-829 (2014).

[34] A. B. Khanikaev, and G. Shvets, Nat. Photonics **11**, 763 (2017).

[35] B. Bahari, A. Ndao, F. Vallini, A. El Amili, Y. Fainman, and B. Kanté, Science **358**, 636-640 (2017).

[36] G. Harari, M. A. Bandres, Y. Lumer, M. C. Rechtsman, Y. D. Chong, M. Khajavikhan,

D. N. Christodoulides, and M. Segev, Science **359** (2018).

[37] M. A. Bandres, S. Wittek, G. Harari, M. Parto, J. Ren, M. Segev, D. N. Christodoulides, and M. Khajavikhan, Science **359** (2018).

[38] W. P. Su, J. R. Schrieffer, and A. J. Heeger, Phys. Rev. Lett. **42**, 1698-1701 (1979).

[39] A. Blanco-Redondo, I. Andonegui, M. J. Collins, G. Harari, Y. Lumer, M. C. Rechtsman, B. J. Eggleton, and M. Segev, Phys. Rev. Lett. **116**, 163901 (2016).

[40] Q. Cheng, Y. Pan, Q. Wang, T. Li, and S. Zhu, Laser Photonics Rev. **9**, 392-398 (2015).

[41] A. Poddubny, A. Miroshnichenko, A. Slobozhanyuk, and Y. Kivshar, ACS Photonics **1**, 101-105 (2014).

[42] A. P. Slobozhanyuk, A. N. Poddubny, A. E. Miroshnichenko, P. A. Belov, and Y. S. Kivshar, Phys. Rev. Lett. **114**, 123901 (2015).

[43] S. Malzard, C. Poli, and H. Schomerus, Phys. Rev. Lett. **115**, 200402 (2015).

[44] S. Weimann, M. Kremer, Y. Plotnik, Y. Lumer, S. Nolte, K. G. Makris, M. Segev, M. C. Rechtsman, and A. Szameit, Nat. Mater. **16**, 433 (2016).

[45] M. Parto, S. Wittek, H. Hodaei, G. Harari, M. A. Bandres, J. Ren, M. C. Rechtsman, M. Segev, D. N. Christodoulides, and M. Khajavikhan, Phys. Rev. Lett. **120**, 113901 (2018).

[46] H. Zhao, P. Miao, M. H. Teimourpour, S. Malzard, R. El-Ganainy, H. Schomerus, and L. Feng, Nat. Commun. **9**, 981 (2018).

[47] P. St-Jean, V. Goblot, E. Galopin, A. Lemaître, T. Ozawa, L. Le Gratiet, I. Sagnes, J. Bloch, and A. Amo, Nat. Photonics **11**, 651-656 (2017).

[48] Y. Akahane, T. Asano, B.-S. Song, and S. Noda, Nature **425**, 944 (2003).

[49] K. Nozaki, and T. Baba, Appl. Phys. Lett. **88**, 211101 (2006).

[50] M. Takiguchi, H. Taniyama, H. Sumikura, M. D. Birowosuto, E. Kuramochi, A. Shinya, T. Sato, K. Takeda, S. Matsuo, and M. Notomi, Opt. Express **24**, 3441-3450 (2016).

[51] A. Majumdar, A. Rundquist, M. Bajcsy, V. D. Dasika, S. R. Bank, and J. Vučković, Phys. Rev. B **86**, 195312 (2012).

[52] N. Caselli, F. Intonti, F. La China, F. Biccari, F. Riboli, A. Gerardino, L. Li, E. H. Linfield, F. Pagliano, and A. Fiore, Nat. Commun. **9**, 1-8 (2018).

[53] C. Han, M. Lee, S. Callard, C. Seassal, and H. Jeon, Light: Science & Applications **8**, 40 (2019).

[54] D. J. Griffiths, *Introduction to quantum mechanics* (Cambridge University Press, 2017).

[55] P. Delplace, D. Ullmo, and G. Montambaux, Phys. Rev. B **84**, 195452 (2011).

[56] M. A. Popović, C. Manolatou, and M. R. Watts, Opt. Express **14**, 1208-1222 (2006).

[57] P. B. Deotare, M. W. McCutcheon, I. W. Frank, M. Khan, and M. Lončar, Appl. Phys. Lett. **95**, 031102 (2009).

[58] M. Lee, J. Lee, S. Kim, S. Callard, C. Seassal, and H. Jeon, Sci. Adv. **4**, e1602796 (2018).

[59] M. Lee, S. Callard, C. Seassal, and H. Jeon, Nat. Photonics **13**, 445-448 (2019).

[60] M. Khajavikhan, A. Simic, M. Katz, J. Lee, B. Slutsky, A. Mizrahi, V. Lomakin, and Y. Fainman, Nature **482**, 204-207 (2012).

[61] Y. Ota, M. Kakuda, K. Watanabe, S. Iwamoto, and Y. Arakawa, Opt. Express **25**, 19981-19994 (2017).

[62] T. F. Krauss, J. Phys. D: Appl. Phys. **40**, 2666 (2007).

[63] Y. Sato, Y. Tanaka, J. Upham, Y. Takahashi, T. Asano, and S. Noda, Nat. Photonics **6**, 56-61 (2011).

[64] S. Liu, W. Gao, Q. Zhang, S. Ma, L. Zhang, C. Liu, Y. J. Xiang, T. J. Cui, and S. Zhang, Research **2019**, 8609875 (2019).

[65] W. A. Benalcazar, B. A. Bernevig, and T. L. Hughes, Science **357**, 61-66 (2017).

[66] M. Serra-Garcia, V. Peri, R. Süsstrunk, O. R. Bilal, T. Larsen, L. G. Villanueva, and S. D. Huber, Nature **555**, 342 (2018).

[67] S. Imhof, C. Berger, F. Bayer, J. Brehm, L. W. Molenkamp, T. Kiessling, F. Schindler, C. H. Lee, M. Greiter, T. Neupert, and R. Thomale, Nat. Phys. **14**, 925-929 (2018).

[68] C. W. Peterson, W. A. Benalcazar, T. L. Hughes, and G. Bahl, Nature **555**, 346 (2018).

[69] S. Mittal, V. V. Orre, G. Zhu, M. A. Gorlach, A. Poddubny, and M. Hafezi, Nat. Photonics (2019).

[70] M. Ezawa, Phys. Rev. Lett. **120**, 026801 (2018).

[71] H. Xue, Y. Yang, F. Gao, Y. Chong, and B. Zhang, Nat. Mater. **18**, 108-112 (2019).

[72] X. Ni, M. Weiner, A. Alù, and A. B. Khanikaev, Nat. Mater. **18**, 113-120 (2019).

[73] B.-Y. Xie, G.-X. Su, H.-F. Wang, H. Su, X.-P. Shen, P. Zhan, M.-H. Lu, Z.-L. Wang, and Y.-F. Chen, Phys. Rev. Lett. **122**, 233903 (2019).

[74] B.-Y. Xie, H.-F. Wang, H.-X. Wang, X.-Y. Zhu, J.-H. Jiang, M.-H. Lu, and Y.-F. Chen, Phys. Rev. B **98**, 205147 (2018).

[75] X.-D. Chen, W.-M. Deng, F.-L. Shi, F.-L. Zhao, M. Chen, and J.-W. Dong, Phys. Rev. Lett. **122**, 233902 (2019).

[76] A. El Hassan, F. K. Kunst, A. Moritz, G. Andler, E. J. Bergholtz, and M. Bourennane, Nat. Photonics **13**, 697-700 (2019).

[77] R. Chikkaraddy, B. De Nijs, F. Benz, S. J. Barrow, O. A. Scherman, E. Rosta, A. Demetriadou, P. Fox, O. Hess, and J. J. Baumberg, Nature **535**, 127-130 (2016).

[78] T. B. Hoang, G. M. Akselrod, C. Argyropoulos, J. Huang, D. R. Smith, and M. H. Mikkelsen, Nat Commun **6**, 7788 (2015).

[79] C. Han, M. Kang, and H. Jeon, arXiv, arXiv: 2002.04757 (2020).

[80] F. Liu, and K. Wakabayashi, Phys. Rev. Lett. **118**, 076803 (2017).

[81] R. D. King-Smith, and D. Vanderbilt, Phys. Rev. B **47**, 1651-1654 (1993).

[82] W. A. Benalcazar, and A. Cerjan, arXiv preprint arXiv:1908.05687 (2019).

[83] K. F. Mak, K. L. McGill, J. Park, and P. L. McEuen, Science **344**, 1489-1492 (2014).

[84] J. R. Schaibley, H. Yu, G. Clark, P. Rivera, J. S. Ross, K. L. Seyler, W. Yao, and X. Xu, Nature Reviews Materials **1**, 1-15 (2016).

[85] F. Xia, H. Wang, D. Xiao, M. Dubey, and A. Ramasubramaniam, Nat. Photonics **8**, 899 (2014).

[86] K. F. Mak, and J. Shan, Nat. Photonics **10**, 216 (2016).

[87] T. Ma, and G. Shvets, New J. Phys. **18** (2016).

[88] F. Gao, H. Xue, Z. Yang, K. Lai, Y. Yu, X. Lin, Y. Chong, G. Shvets, and B. Zhang, Nat. Phys. **14**, 140 (2017).

[89] X.-D. Chen, F.-L. Zhao, M. Chen, and J.-W. Dong, Phys. Rev. B **96** (2017).

[90] L. Ye, Y. Yang, Z. Hong Hang, C. Qiu, and Z. Liu, Appl. Phys. Lett. **111** (2017).

[91] M. I. Shalaev, W. Walasik, A. Tsukernik, Y. Xu, and N. M. Litchinitser, Nat. Nanotech.

14, 31-34 (2019).

[92] X. T. He, E. T. Liang, J. J. Yuan, H. Y. Qiu, X. D. Chen, F. L. Zhao, and J. W. Dong, Nat Commun **10**, 872 (2019).

[93] J. Ma, X. Xi, and X. Sun, arXiv preprint arXiv:1908.03708 (2019).

[94] Y. Zeng, U. Chattopadhyay, B. Zhu, B. Qiang, J. Li, Y. Jin, L. Li, A. G. Davies, E. H. Linfield, B. Zhang, Y. Chong, and Q. J. Wang, Nature **578**, 246-250 (2020).

[95] Y. Ota, R. Katsumi, K. Watanabe, S. Iwamoto, and Y. Arakawa, Communications Physics **1**, 86 (2018).

[96] M. Pan, H. Zhao, P. Miao, S. Longhi, and L. Feng, Nat Commun **9**, 1308 (2018).

[97] H. Zhao, X. Qiao, T. Wu, B. Midya, S. Longhi, and L. Feng, Science **365**, 1163-1166 (2019).

[98] M. Pan, H. Zhao, P. Miao, S. Longhi, and L. Feng, Nat. Commun. **9**, 1308 (2018).

[99] S. Kruk, A. Poddubny, D. Smirnova, L. Wang, A. Slobozhanyuk, A. Shorokhov, I. Kravchenko, B. Luther-Davies, and Y. Kivshar, Nat. Nanotech. (2018).

[100] D. A. Dobrykh, A. V. Yulin, A. P. Slobozhanyuk, A. N. Poddubny, and Y. S. Kivshar, Phys. Rev. Lett. **121**, 163901 (2018).

[101] S. Kruk, A. Poddubny, D. Smirnova, L. Wang, A. Slobozhanyuk, A. Shorokhov, I. Kravchenko, B. Luther-Davies, and Y. Kivshar, Nat. Nanotech. **14**, 126-130 (2019).

[102] S. Barik, A. Karasahin, C. Flower, T. Cai, H. Miyake, W. DeGottardi, M. Hafezi, and E. Waks, Science **359**, 666-668 (2018).

[103] S. Mittal, E. A. Goldschmidt, and M. Hafezi, Nature **561**, 502-506 (2018).

[104] A. Blanco-Redondo, B. Bell, D. Oren, B. J. Eggleton, and M. Segev, Science **362**, 568 (2018).

Abstract in Korean

물질의 위상적 상태는 기존에 없었던 새로운 물질의 상태를 제시함으로써 양자 물질의 시대를 열었다. 특히, 위상부도체는 내부가 부도체인 동시에 도체인 표면을 가지고 있으며 표면에서의 전자의 흐름은 위상적으로 보호되므로 불완전성에 의한 산란이 크게 감소된다. 이러한 특징은 스핀트로닉 소자 또는 양자 컴퓨터에서의 안정적인 정보 저장에 활용될 것으로 기대된다. 한편, 이러한 응집물질물리학에서의 발견은 빛과 같은 다른 파동 시스템에서의 위상적 상태를 위한 연구의 포석이 되었다. 위상부도체 표면의 전자와 마찬가지로, 빛의 위상적 가장자리 상태는 산란으로부터 보호되고, 이러한 특성은 고효율의 광도파로, 광결합기 등의 응용에 기여할 것으로 기대된다.

지금까지의 많은 위상광자학 연구는 빛의 전파특성에 집중되어 있었다. 예를 들면, 시간 반전 대칭성이 깨진 양자-홀 가장자리 상태 또는 스핀으로부터 보호된 가장자리 상태를 통한 빛의 전파가 연구되었다. 이러한 수동적 시스템에 비해 레이저 발진은 많이 연구되지 않았다. 기존의 몇몇 위상적 가장자리 상태를 이용한 레이저 연구는 마이크로링 공진기를 이용하여서 소자의 크기가 매우 크다는 단점이 있었다. 파장-스케일의 광자결정구조에서 위상적 가장자리 상태를 확인하고 이를 이용한 레이저 소자를 개발한다면 향상된 광 집적 회로나 위상적 빛-물질 상호작용을 연구할 수 있는 기반이 될 것으로 기대한다. 뿐만 아니라, 광소자의 크기가 작아질수록 공정상의 오차에 의한 성능 편차가 커지는데, 위상적 가장자리 상태는 이러한 상황에서 해결책이 될 것으로 기대된다.

이 논문에서는, 첫 번째로, 광자결정 공진기 배열을 통한 위상적 가장자리 상태에서의 레이저 발진을 시연하였다. Su-Schrieffer-Heeger 모델에 기반한 배열과 다중양자우물 광이득 물질을 이용하여 위상적으로 비자명한 배열에서 위상적 가장자리 상태가 레이저 발진을 통해서 확인되었다. 근접장 측정을 통해 모드 분포를 직접적으로 관찰함으로써 광모드의 기원을 확인할 수 있었고, 공정적 무질서로부터 가장자리 상태가 상대적으로 견고함을 확인하였다.

두 번째로, 2차원 광자결정에서의 고차원 위상적부도체 원리에 의한 계층적 가장자리 상태에서의 레이저 발진을 시연하였다. 2차원 SSH 배열과 유사한 형태로 광자결정을 디자인하였고, 광이득 물질을 이용하여 위치에 대해 선택적인 광펌핑을 통해 다양한 상태에서의 레이저 발진을 확인하였다. 각 상태에서의 레이저 특성을 스펙트럼과 이미지 분석을 통해서 조사하였다.

마지막으로, valley 가장자리 상태를 이용한 링 공진기에서의 레이저 발진을 시연하였다. 공간 반전 대칭성이 깨어진 구조에서는 valley가 보호된 가장자리 상태가 나타날 수 있고 valley간 산란이 적은 상황에서는 전파 특성이 보호되어 구조적 변화에 의한 후방산란이 매우 낮아진다. 이를 이용하여 급격한 꺾임을 가진 valley 가장자리 모드를 이어서 링 형태로 공진기를 제작하였고 실제로 위상적으로 보호된 특성에 의해 레이저 발진이 가능한 것을 위상적으로 보호되지 않은 자명한 링 공진기와의 비교를 통해 확인하였다.

주요어: 광자 결정, 위상 광자학, SSH 모델, 가장자리 상태 레이저, valley 가장자리 모드

학번: 2014-21364